Fundamentals and Application in CO_2 Sorptivity of K_2CO_3 and Na_2CO_3

July 2015

Luo Hongchao

Graduate School of Science

Chiba University

（千葉大学学位申請論文）

Fundamentals and Application in CO_2 Sorptivity of K_2CO_3 and Na_2CO_3

炭酸カリウムと炭酸ナトリウムの二酸化炭素吸蔵反応の基礎と応用

July 2015

千葉大学大学院理学研究科

基盤理学専攻化学コース

駱　紅超

Contents

Chapter 1: General introduction

Numerous observations of the climate system based on direct measurements and remote sensing from satellites and other platforms suggest the increasing temperature of the Earth over the past hundred-odd years. The Figure1-1 (upper) by Intergovernmental Panel on Climate Change (IPCC), shows how the temperature increases over the period 1850 to 2012 [1]. In addition to robust multi-decadal, particularly the past three decadal warming, globally averaged surface temperature exhibits substantial decadal and interannual variability, shown in Figure 1-1 (lower) [1]. Many scientific reports indicate that the intervention of human activities has brought about climate changes and global current temperature [1-9].

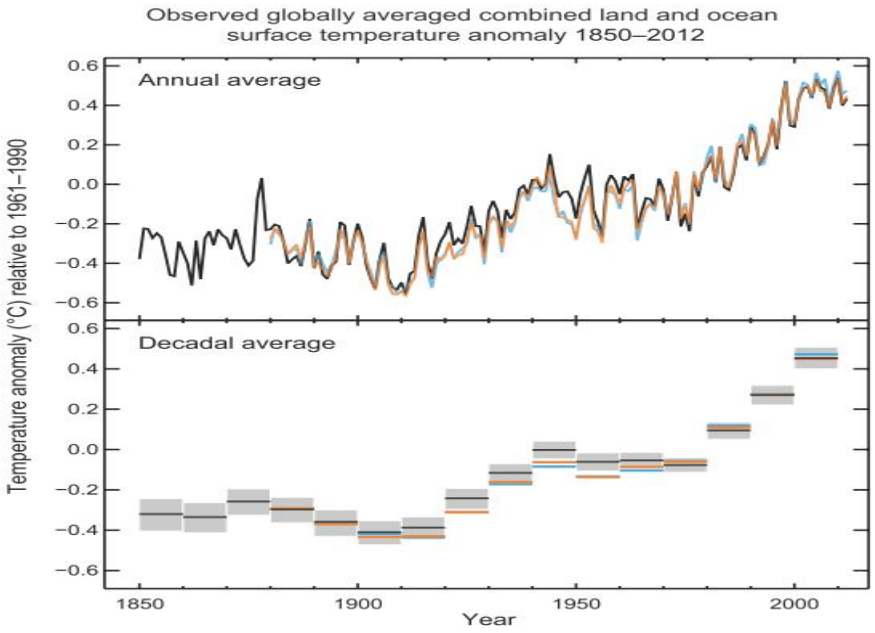

Figure 1-1: Observed global mean combined land and ocean surface temperature anomalies, from 1850 to 2012 from three data sets [1].

1.1 Causes of global warming

According to the IPCC, the climate change attributed to the radiative forcing of natural and anthropogenic greenhouse gases (GHGs) and their constitutions in the atmosphere. Figure 1-2 shows the contributions of radiative forcing of climate from different types of greenhouse gases. Positive radiative forcing results in warming of the atmosphere, and negative forcing results in cooling of the atmosphere [1-3, 5-7]. As shown in Figure 1-2, radiative forcing values are global average ones, partitioned according to the emitted compounds or processes that result in a combination of drivers [1]. Compared with the primary greenhouse gases such as methane, water and nitrous oxide, CO_2 has a higher positive radiative forcing of proximately 1.66 Wm^{-2}. This property of greenhouse gases suggests that how much the concentration of greenhouse gases, particularly CO_2 from anthropogenic activities in the atmosphere is profoundly affect global temperature change.

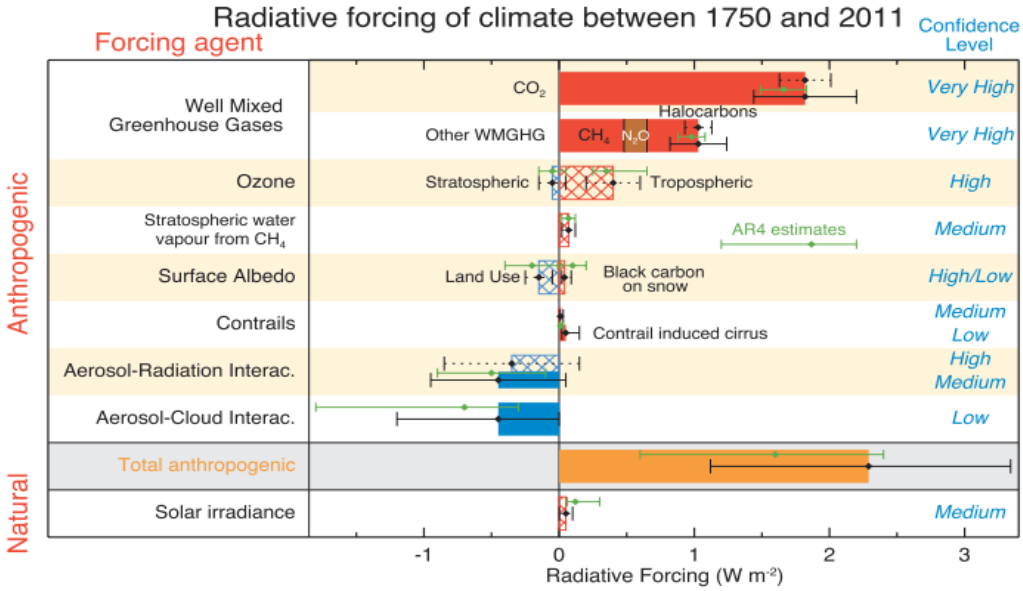

Figure 1-2: Radiative forcing estimates in 2011 relative to 1750 and aggregated uncertainties for the main drivers of climate change [1].

Anthropogenic greenhouse gas emissions have increased since the industrial revolution, leading to atmospheric concentrations of carbon dioxide, methane and nitrous oxide that are unprecedented, and are now higher than ever [10]. The effects of

increased atmospheric concentrations of greenhouse gases caused by fossil fuel burning, industrialization and deforestation with other anthropogenic activities together, are extremely likely to have been the dominant reason for the observed warming [7,10].

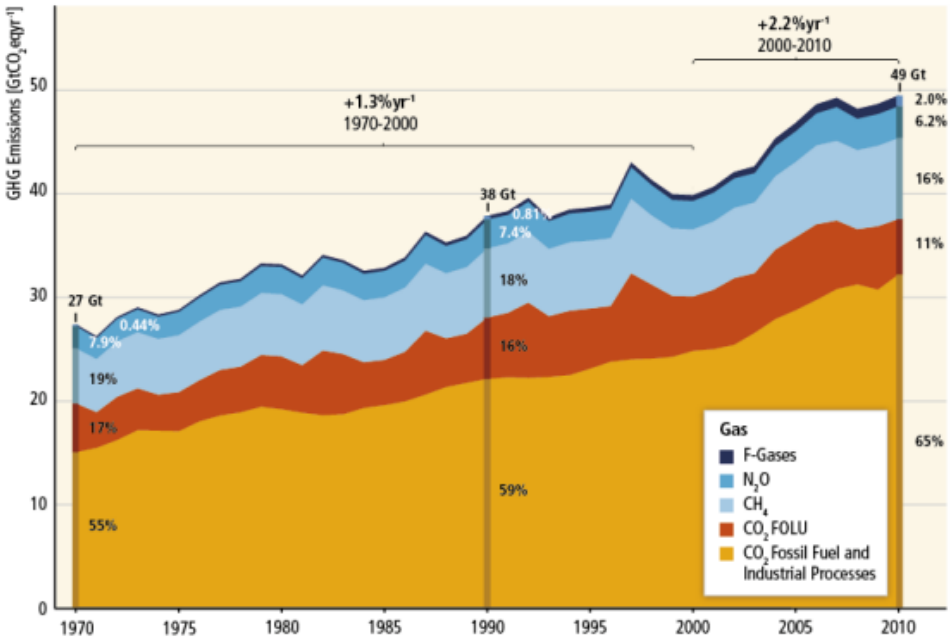

Figure 1-3: Global annual emissions of anthropogenic GHGs for the period 1970 to 2010 by gases: CO_2 from fossil fuel combustion and industrial processes; CO_2 from Forestry and Other Land Use (FOLU); methane (CH_4); nitrous oxide (N_2O); fluorinated gases covered under the Kyoto Protocol (F-gases) [10].

Between 1750 and 2011, cumulative anthropogenic CO_2 emissions to the atmosphere were 2040 ± 310 $GtCO_2$. About 40% of these emissions have remained in the atmosphere (880 ± 35 $GtCO_2$) [10]. Figure 1-3 shows the CO_2 emission from fossil fuel combustion and industrial processes increased from 55% to 65% between 1970 and 2010. Furthermore, the CO_2 emission from fossil fuel combustion and industrial processes continued to be the most important source compared with CO_2 from FOLU, methane (CH_4), nitrous oxide (N_2O), and F-gases, and continued about 78% of the total greenhouse gas emissions increase from during the period 1970 to 2010.

According to carbon dioxide data at Mauna Loa Observatory affiliated with National Oceanic and Atmospheric Administration (NOAA), shown in Figure 1-4, its concentration has been increasing gradually and evidently. Subsequently, the linear increase in the concentration of CO_2 emissions coupled with the high positive radiative forcing as noted above tends towards warming the atmosphere even further [1-3, 5-7].

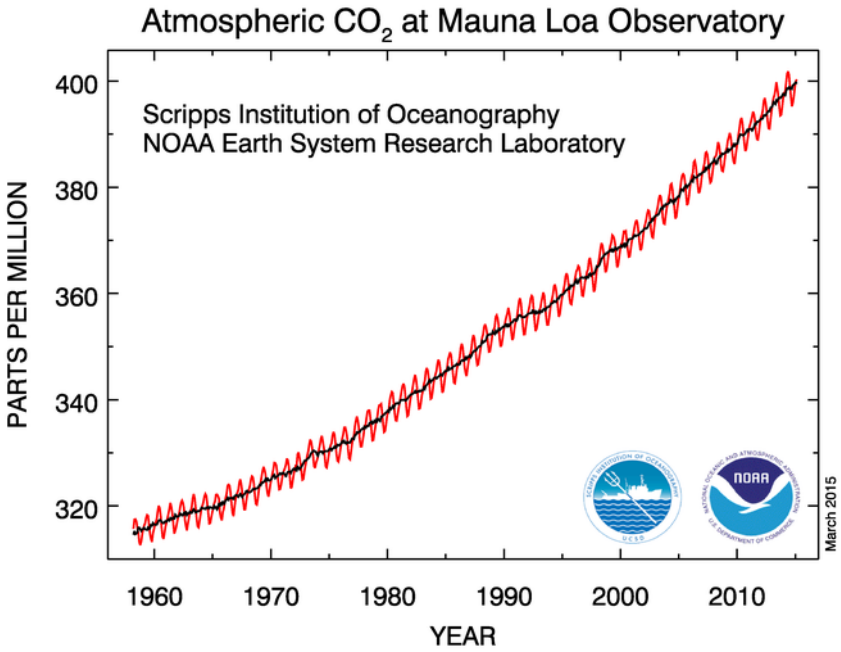

Figure 1-4: Atmospheric CO_2 at Mauna Loa Observatory, Hawaii. The red curve means the CO_2 data measured as the mole fraction in dry air, on Mauna Loa constitute the longest record of direct measurements of CO_2 in the atmosphere; the black curve represents the seasonally corrected data [11].

1.2 Impacts and Risks of global warming

As the global average surface temperature increases caused by the anthropogenic increase in greenhouse gas, particularly CO_2 concentration, the impacts and risks on Earth's environment have gradually begun to appear. Impacts from human-induced climate-related extremes, such as floods, cyclones, droughts, and wildfires, heat waves, reveal significant vulnerability and exposure of some ecosystems and many human systems to current climate variability [12, 13]. According to IPCC reports, the global

warming has very likely made a substantial contribution to increases in global upper ocean heat content, while the retreat of glaciers, surface melting of the Greenland ice sheet and Arctic sea-ice loss have very likely lead to the uprise in global mean sea-level. The global water cycle has been likely influenced. On the other hand, as the substantial increase in the CO_2 emission will very likely result in the acidification of ocean water and also likely cause harmful algal blooms and the massive extinctions of some marine organisms to threaten the whole ecosystems in the future. To summarize, the global warming not only affects the innumerable animals and plants but also eventually affects the lives hundreds of thousands of people.

1.3 Carbon dioxide capture and storage

Since CO_2 is the major anthropogenic greenhouse gas in the atmosphere contributing to global warming, in recent years worldwide efforts have been devoted to develop the mitigation options. There are four effective ways to reduce CO_2 emissions into the atmosphere: (I) improving energy utilization efficiency, (II) increasing the use of less carbon-intensive fuels, biomass-based fuels, nuclear power and renewable energy sources such as solar energy, (III) enhancing biological sinks and reducing non-CO_2 greenhouse gas emissions, and (IV) carbon dioxide capture and storage (CCS) [14]. However, fossil fuels have still been the dominant energy source at present. Furthermore, other energy sources such as nuclear power and solar energy still cannot replace fossil fuels on a large scale. As a result, CCS is widely used for the reduction of the CO_2 concentration.

CCS as main strategy for CO_2 management is a process consisting of several stages such as the separation and capture of CO_2 from the large emission sources, i.e. industrial and energy-related sources, the transportation to the storage site and storage it in a suitable deep geological formation for long-term isolation from the atmosphere [14]. The scheme of CCS is shown in Figure 1-5 [15].

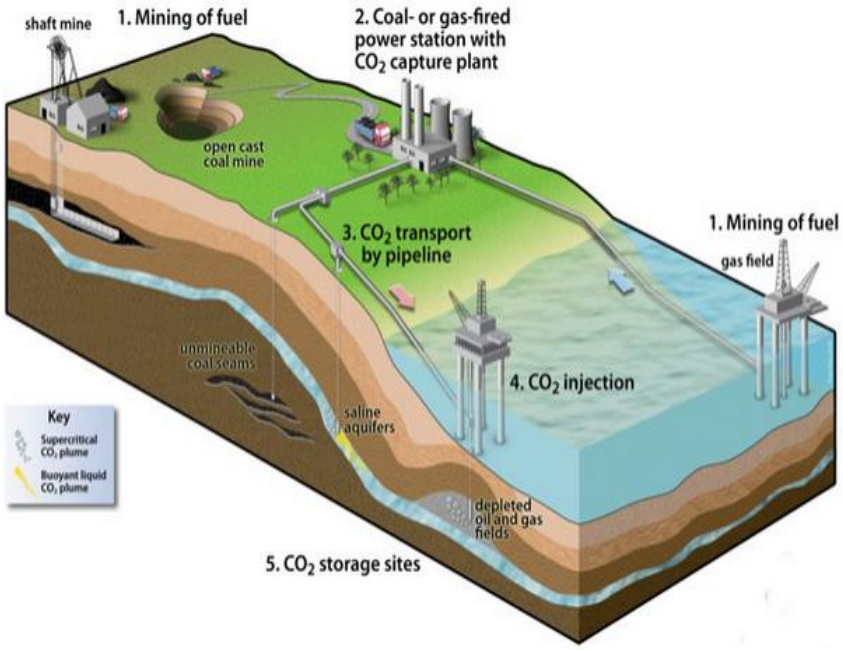

Figure 1-5: The scheme of CO_2 capture and storage process [15].

Among these stages, the transportation and storage of CO_2 are relatively mature technologies and a growing number of fully integrated CCS projects have reached the pilot-stage [16]. However, the considerable cost of capture is slowing down the development of CCS projects [17]. Therefore, the technologies of CO_2 capture should be required urgently and receive considerable research effort. Consequently, various methods and numerous materials are attempted to apply to CO_2 capture.

1.4 Methods and materials for CO_2 capture

Several methods have been employed to CO_2 separation and capture, mostly including absorption, cryogenics, membranes, adsorption [18, 19]. These usually used methods and associated materials are schematically illustrated in Figure 1-6, among these methods except for cryogenics and Microbial, main technologies including the use of scrubbing solutions, solid sorbents and membranes are used to separate and capture CO_2 [18].

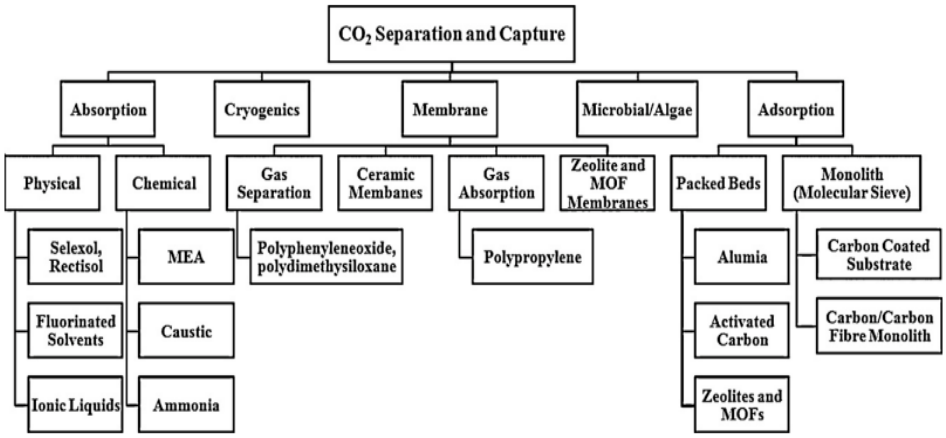

Figure 1-6: Different methods and associated materials for CO_2 separation and capture [18].

Among associated materials, solid sorbents have been most commonly investigated for CO_2 capture. Compared to liquid sorbents, solid sorbents can be used over a wider temperature range from ambient temperature to 700 ℃, yielding less loss after several cycles [20].

1.4.1 Classification of solid materials

However, CO_2 recovery used by different solid sorbents still has faced several challenges. The CO_2 capacity and reaction rate primarily indicate if the solid sorbent can been used for CO_2 capture. The source and cost of solid sorbent as the next thing, demined if this solid sorbent has a wide application prospects. The required conditions of solid sorbents will be the crucial factor in CO_2 capture of solid sorbents. On the one hand, the conditions such as high temperature, low or high pressure are gained through additional energy supply, this have to increase energy composition. On the other hand, energy composition undoubtedly will lead to the formation of CO_2 and other gases again. Hence, the required conditions of solid sorbents for CO_2 capture should be close to ambient temperature and pressure. According to the adsorption and desorption temperatures at 0.1 MPa, solid sorbents are classified as low-temperature sorbents (< 200°C), intermediate-temperature sorbents (200–400 °C), and high-temperature

sorbents (> 400 °C) [21]. Table 1-1 shows the CO_2 capture capacities of main types of sorbents under the required condition. As introduced above, compared with each other, low temperature sorbents has a better potential application for CO_2 capture at 0.1 MPa.

Table 1-1: The CO_2 capture capacities of the main types of sorbents according to their sorption and desorption temperatures at 0.1 MPa [21].

Adsorbent type		Temperature /°C	CO_2 capacity /mmol·g^{-1}
Low-temperature	Carbon based	≤ 80	≤ 3.5
	Zeolite based	≤ 100	≤ 4.9
	MOF based	≤ 100	≤ 4.5
	Alkali-metal carbonate based	≤ 120	≤ 9.4
	Amine based	≤ 60	≤ 5.5
Intermediate-temperature	LDH based	200–400	≤ 1.4
	Calcium based	600–700	≤ 11.6
High-temperature	Alkali ceramic based	500–600	≤ 6.5

Among these low temperature sorbents, amine-, Zeolite-, activated carbon-, and metal–organic frameworks (MOF) based sorbents have been focused for the application of CO_2 capture [22-25]. However, these technologies still face challenges, such as high energy consumption during sorbent regeneration, the efficient issue under ambient conditions because of interference from adsorbed CO_2 and H_2O, and high cost for the removal of the gases. Furthermore, these sorbents would not be desirable or appropriate for the practical application of CO_2 capture methods under moist conditions.

1.4.2 Alkali-metal carbonate based sorbents

Alkali-metal carbonate based sorbents as typical low-temperature sorbents have been paid more attention for CO_2 capture application over the past several years due to both high sorption capacity and low cost [26-29]. Prior to 2014, many studies on the CO_2

capture of alkali-metal carbonate based sorbents focused on both experimental fuel gas conditions and porous supports. Particularly, the experimental conditions of CO_2 capture include reaction or regeneration temperature, CO_2 concentration, H_2O concentration, etc [26]. Various supports used with K_2CO_3 have higher occlusion amounts for CO_2 capture due to enhanced surface area or pore volume.

Most previous studies focused on CO_2 capture of alkali-metal carbonate based sorbents such as K_2CO_3 and Na_2CO_3 took place within relatively high temperature range (50–120 °C) as the following reaction (1-1).

$$M_2CO_3\ (s) + CO_2\ (g) + H_2O\ (g) \leftrightarrows 2MHCO_3\ (s) \qquad (1\text{-}1)$$

where the forward, exothermic reaction is the bicarbonate formation of M_2CO_3 (M: Na, K) while the reverse, endothermic reaction is the decomposition of $MHCO_3$.

1.4.2.1 Sodium carbonate (Na_2CO_3)

Numerous researches on the CO_2 occlusion of Na_2CO_3 under different CO_2 and H_2O concentration, CO_2 capture also did not always occur via reaction (1-1). Several reactions of CO_2 occlusion of Na_2CO_3 under moist conditions are involved as follows [30]:

$$Na_2CO_3\ (s) + H_2O\ (g) \leftrightarrows Na_2CO_3{\cdot}H_2O\ (s) \qquad (1\text{-}2)$$

H_2O capture capacity ⋯ 9.43 $mmol{\cdot}g^{-1}$

$$5Na_2CO_3\ (s) + 3CO_2\ (g) + 3H_2O\ (g) \leftrightarrows 2Na_5H_3(CO_3)_4\ (s) \qquad (1\text{-}3)$$

CO_2 capture capacity ⋯ 5.66 $mmol{\cdot}g^{-1}$

$$Na_2CO_3\ (s) + CO_2\ (g) + H_2O\ (g) \leftrightarrows 2NaHCO_3\ (s) \qquad (1\text{-}4)$$

CO_2 capture capacity ⋯ 9.43 $mmol{\cdot}g^{-1}$

Different precursors such as Na_2CO_3, $NaHCO_3$, and $Na_2CO_3{\cdot}NaHCO_3{\cdot}2H_2O$ were also attempted to apply for the CO_2 capture in moist conditions [30]. It is found that

Na_2CO_3 decomposed from $NaHCO_3$ has a better performance on the CO_2 occlusion because of good pore structure. Thus, in this study, $NaHCO_3$ is used to prepare Na_2CO_3 at a N_2 atmosphere for CO_2 capture.

1.4.2.2 Potassium carbonate (K_2CO_3)

In similar, related to the reactions of CO_2 occlusion of K_2CO_3 under moist conditions are as shown in reaction (1-2), reaction (1-3), reaction (1-4) and reaction (1-5) [31]:

$$K_2CO_3\ (s) + 1.5H_2O\ (g) \leftrightarrows K_2CO_3 \cdot 1.5H_2O\ (s) \quad (1\text{-}5)$$

H_2O capture capacity ⋯ 10.8 $mmol \cdot g^{-1}$

$$2K_2CO_3\ (s) + CO_2\ (g) + 2.5H_2O\ (g) \leftrightarrows K_4H_2(CO_3)_3 \cdot 1.5H_2O\ (s) + 0.5H_2O\ (g) \quad (1\text{-}6)$$

CO_2 capture capacity ⋯ 3.62 $mmol \cdot g^{-1}$

$$K_4H_2(CO_3)_3 \cdot 1.5H_2O\ (s) + CO_2\ (g) \leftrightarrows 4KHCO_3\ (s) + 0.5H_2O\ (g) \quad (1\text{-}7)$$

CO_2 capture capacity ⋯ 2.73 $mmol \cdot g^{-1}$

$$K_2CO_3\ (s) + CO_2\ (g) + H_2O\ (g) \leftrightarrows 2KHCO_3\ (s) \quad (1\text{-}8)$$

CO_2 capture capacity ⋯ 7.24 $mmol \cdot g^{-1}$

Furthermore, different precursors of K_2CO_3 also influence the CO_2 capture behavior. Zhao et al. reported that K_2CO_3 from different precursors such as K_2CO_3, $K_2CO_3 \cdot 1.5H_2O$ and $KHCO_3$ was used to occlude CO_2 in moist conditions [32]. It is found that K_2CO_3 decomposed from $KHCO_3$ has hexagonal crystal structure and better pore structure favorable to CO_2 capture, while K_2CO_3 from other precursors has in general monoclinic crystal structure [33]. Thus, in this study, $KHCO_3$ can be used to prepare K_2CO_3 at N_2 atmosphere for CO_2 capture.

The kinetics mechanism of pure K_2CO_3 or Na_2CO_3 for CO_2 capture in a moist condition is not clearly understood. Hence, study of the fundamental kinetics of CO_2 occlusion of pure K_2CO_3 or Na_2CO_3 is important. We are systematically investigating

CO_2 occlusion of K_2CO_3 or Na_2CO_3 by changing various reaction conditions, such as temperature, CO_2 concentration, and humidity, based on the CO_2 capture characteristics of pure K_2CO_3 or Na_2CO_3 under moist conditions.

1.5 The objectives and Overview of this research

This study will focus on kinetics in CO_2 capture of K_2CO_3 and Na_2CO_3 under different temperature, CO_2 and H_2O concentrations, respectively. Particularly, the detailed information on CO_2 capture process mainly involves crystal structural changes and morphology variations in CO_2 capture of K_2CO_3 and Na_2CO_3. Therefore, a series of techniques will be the powerful methods to investigate the crystal structural changes and morphology variations. The basic theory and principle analysis of several methods such as thermogravimetric-differential thermal analysis (TG-DTA), X-Ray Diffraction (XRD) and Scanning Electron Microscopy (SEM) are briefly introduced in Chapter 2.

Chapter 3 describes the capacity and kinetics of CO_2 capture in K_2CO_3 under different temperature, CO_2 and H_2O concentrations. According to the structural changes with temperature or reaction time, we attempt to propose the relevant mechanism for CO_2 capture in K_2CO_3. To find its mechanism for CO_2 sequestering, morphology and structural changes with reaction time will be connected to the kinetic and exothermic properties of CO_2 capture process. Also the effect of different stages on kinetics of CO_2 capture in K_2CO_3 under different moist conditions will be further investigated. In all these cases, $K_4H_2(CO_3)_3 \cdot 1.5H_2O$ plays an important role in CO_2 capture. Thus, the structure, morphology, and CO_2 dependence measurements of $K_4H_2(CO_3)_3 \cdot 1.5H_2O$ prepared through high temperature will also be performed.

Chapter 4 presents fundamental in CO_2 capture of Na_2CO_3 under different temperature, CO_2 and H_2O concentrations. The dependence measurements of temperature, CO_2 concentration and H_2O concentration on CO_2 capture of Na_2CO_3 will be studied. Similarly, morphology and structural changes with reaction time from SEM and XRD will also be connected to the kinetic and exothermic properties of CO_2 capture

process.

Finally, the conclusions on the analyses of kinetics, the crystalline structure and morphology changes of CO_2 capture in K_2CO_3 and Na_2CO_3 under different reaction conditions will be generally summarized in Chapter 5.

References

[1] T. F. Stocker, D. Qin, G.-K. Plattner, M. M. B. Tignor, S. K. Allen, J. Boschung, A. Nauels, X. Yu, V. Bex, P. M. Midgley. Climate Change 2013: The Scientific Basis, *Cambridge University Press*, Cambridge, United Kingdom and New York, NY, USA, **2013**.

[2] J. T. Houghton, B. A. Callander, S. K. Varney. Climate Change 1992: The Supplementary Report to the IPCC Scientific Assessment, *Cambridge University Press*, Cambridge, United Kingdom and New York, NY, USA, **1996**.

[3] J. T. Houghton, L. G. Meira . A. Callander, N. Harris, A. Kattenberg, K. Maskell. IPCC 1996: Climate Change 1996: The Science of Climate Change, *Cambridge University Press*, Cambridge, United Kingdom and New York, NY, USA, **1996**.

[4] R. T. Watson, I. R. Noble, B. Bolin, N. H. Ravindranath, D. J. Verardo, D. J. Dokken. IPCC 2000: Land Use, Land-Use Change, and Forestry, *Cambridge University Press*, Cambridge, United Kingdom and New York, NY, USA, **2000**.

[5] T. Houghton, Y. Ding, D. J. Griggs, M. Noquer, P. J. van der Linden, X. Dai, K. Maskell, C. A. Johnson. Climate Change 2001: The Scientific Basis, *Cambridge University Press*, Cambridge, United Kingdom and New York, NY, USA, **2001**.

[6] J. Penman, M. Gytarsky, T. Hiraishi, T. Krug, D. Kruger, R. Pipatti, L. Buendia, K. Miwa, T. Ngara, K. Tanabe, F. Wagner. IPCC 2003: Definitions and Methodological Options to Inventory Emissions from Direct Human-Induced Degradation of Forests and Devegetation of Other Vegetation Types, The Institute for Global Environmental Strategies (IGES), Japan, **2003**.

[7] S. Solomon, D. Qin, M. Manning, Z. Chen, M. Marquis, K. B. Averyt, M. Tignor, H. L. Miller. Climate Change 2007: The Physical Science Basis, *Cambridge University Press*, Cambridge, United Kingdom and New York, NY, USA, **2007**.

[8] C. B. Field, V. Barros, T. F. Stocker, D. Qin, K.J. Mach, G.-K. Plattner, M. D. Mastrandrea, M. Tignor, K. L. Ebi. IPCC 2011: Workshop Report of the

Intergovernmental Panel on Climate Change Workshop on Impacts of Ocean Acidification on Marine Biology and Ecosystems, Carnegie Institution, Stanford, CA, USA, **2011**.

[9] O. Edenhofer, R. Pichs-Madruga, Y. Sokona, C. Field, V. Barros, T. F. Stocker, D. Qin, J. Minx, K. Mach, G.-K. Plattner, S. Schlömer, G. Hansen, M. Mastrandrea. IPCC 2012: Meeting Report of the Intergovernmental Panel on Climate Change Expert Meeting on Geoengineering, Potsdam, Germany, **2012**.

[10] The Core Writing Team, R. K. Pachauri, L. Meyer. Climate Change 2014: Synthesis Report, *Cambridge University Press*, Cambridge, United Kingdom and New York, NY, USA, **2014**.

[11] P. Tans, Monthly Average Carbon Dioxide Concentration. Mauna Loa Observatory. In NOAA/ESRL (www.esrl.noaa.gov/gmd/ccgg/trends/).

[12] M. L. Parry, O. F. Canziani, J. P. Palutikof, P. J. V. Linden, C. E. Hanson. Climate change 2007: Impacts, Adaptation and Vulnerability, *Cambridge University Press*, Cambridge, United Kingdom and New York, NY, USA, **2007**.

[13] C. B. Field, V. R. Barros, D. J. Dokken, K. J. Mach, M. D. Mastrandrea, T. E. Bilir, M. Chatterjee, K. L. Ebi, Y. O. Estrada, R. C. Genova, B. Girma, E. S. Kissel, A. N. Levy, S. MacCracken, P. R. Mastrandrea, L. L. White. IPCC 2014: Summary for policymakers. In: Climate Change 2014: Impacts, Adaptation, and Vulnerability. Part A: Global and Sectoral Aspects, *Cambridge University Press*, Cambridge, United Kingdom and New York, NY, USA, **2014**.

[14] B. Metz, O. Davidson, H. C. de Coninck, M. Loos, L. A. Meyer. IPCC 2005: Special Report on Carbon Dioxide Capture and Storage, *Cambridge University Press*, Cambridge, United Kingdom and New York, NY, USA, **2005**.

[15] http://eandt.theiet.org/magazine/2011/07/carbon-capture.cfm

[16] E. J. Wilson, D. Gerard. IPCC 2007: Carbon Capture and Sequestration: Integrating Technology, Monitoring, Regulation, Wiley, **2007**.

[17] R. A. Khatri, S. S. C. Chuang, Y. Soong, M. Gray. *Energy Fuels*, **2006**, 20,

1514−1520.

[18] J. Li, Y. Ma, M. C. McCarthy, J. Sculley, J. Yu, H. Jeong, P. B. Balbuena, H. Zhou. *Coordination Chemistry Reviews*, **2011**, 255, 1791−1823.

[19] R. Thiruvenkatachari, S. Su, H. An, X. X. Yu. *Progress in Energy and Combustion Science*, **2009**, 35, 438−455.

[20] J. Wang, L. Huang, R. Yang, Z. Zhang, J. Wu, Y. Gao, Q. Wang, D. O'Hare, Z. Zhong. *Energy Environ. Sci.*, **2014**, 7, 3478−3518.

[21] Q. Wang, J. Luo, Z. Zhong, A. Borgna. *Energy Environ. Sci.*, **2011**, 4, 42−55.

[22] M. G. Plaza, S. García, F. Rubiera, J. J. Pis, C. J. Pevida. *Chem. Eng.*, **2010**, 163, 41−47.

[23] S. Cavenati, C. A. Grande, A. E. Rodrigues. *J. Chem. Eng. Data*, **2004**, 49, 1095−1101.

[24] V. Presser, J. McDonough, S.H. Yeon, Y. Gogotsi. *Energy Environ. Sci.*, **2011**, 4, 3059−3066.

[25] Y. Liu, Z. U. Wang, H. C. Zhou. *Greenhouse Gases: Sci.Technol.*, **2012**, 2, 239−259.

[26] Y. Liang, D. P. Harrison, R. P. Gupta, D. A. Green, W. A. McMichael. *Energy Fuels*, **2004**, 18, 569−575.

[27] S. C. Lee, B. Y. Choi, C. K. Ryu, Y. S. Ahn, T. J. Lee, J. C. Kim. *Korean J. Chem. Eng.*, **2006**, 23, 374−379.

[28] Y. Seo, S. H. Jo, C. K. Ryu, C. K. Yi. *Chemosphere*, **2007**, 69, 712−718.

[29] C. Zhao, X. Chen, C. Zhao. *Energy Fuels*, **2010**, 24, 1009−1012.

[30] Y. Liang. Carbon dioxide capture from flue gas using regenerable sodium-based sorbents. M.S. Dissertation, Louisiana State University (LSU), Baton Rouge, LA, **2003**.

[31] C. Zhao, X. Chen, C. Zhao, Y. Liu. *Energy Fuels*, **2009**, 23, 1766−1769.

[32] C. Zhao, X. Chen, C. Zhao. *Ind. Eng. Chem. Res.*, **2010**, 49, 12212−12216.

[33] C. Zhao, X. Chen, C. Zhao. *Energy Fuel*, **2012**, 26, 1401−1405.

Chapter 2: The basic theory

When the molecule from a fluid-phase approaches a solid material, phenomena taking place at the solid-fluid interface could be adsorption, absorption, sorption or occlusion. Phenomena mentioned above are controlled by the interaction between the molecule and solid surface according to the properties of both the molecule and the solid material. Moreover, these properties of solid material, i.e., pore size, surface area, and crystal structure, mainly depend on its preparation methods. Thus, the properties of solid contacted with molecules will be studied by a series of different techniques, which can be allowed to give insight into the properties of the solid surface and describe the crystal structure changes of solid materials before and after the gas-solid interactions [1, 2]. In this chapter, the basic theory and principle of main methods used for characterization of solid materials will be briefly described.

2.1 Gas adsorption

Gas adsorption properties strongly depended not only on the pore size but also on the interaction between molecules and the solid surface. According to the International Union of Pure and Applied Chemistry (IUPAC) recommendation, the pore sizes are classified as micropore (< 2 nm), mesopore (2−50 nm) and macropore (> 50 nm) [3]. On the other hand, the interaction between guest molecules and solid include adsorption, absorption, sorption or occlusion. Adsorption can be defined as an equilibrium process in the bulk phase and interface in a very short time. Moreover, adsorption can be classified as physical adsorption (physisorption) and chemical adsorption (chemisorption). Physisorption is mainly caused by the dispersion force between the molecules (adsorbent) at the solid-gas interface and adsorptive molecules (adsorbate),

while chemisorption is duo to the charge transfer interaction or chemical bond formation between adsorbent and adsorbate, to yield new chemical compound. Thus, molecular interactions of chemisorption are much stronger than those of physical adsorption. In contrast, the slowly equilibrium process involving the penetration of molecules into the bulk solid phase by some process of diffusion is known as absorption. If an initial rapid adsorption is followed by a slow process of absorption of molecules into the interior of solid, in this case, the process is called sorption, generally absorption because the effects of absorption cannot be told from those of adsorption. Occlusion is similar to the sorption, but is restricted to of gases by metals only [4]. Moreover, the interaction between molecule and the solid surface among the phenomena mentioned above can also be clearly classified by the occurrence of the structural change of a molecule and/or solid [5]. Thus, novel fundamental concepts on solid-molecule interaction are summarized based on the four types of molecule–solid interaction, as showed in Table 2-1.

Table 2-1: Four types of molecule-solid interaction [5].

Types of molecule-solid interactions	Molecular structure	Solid structure
Physical adsorption	No Change	No Change
Chemical adsorption	Change	No Change
Absorption	No Change	Change
Occlusion	Change	Change

Physical adsorption does not lead to the structural changes of both an adsorbed molecule and solid owning to the dispersion interaction as the main interaction of physical adsorption, inducing no change in the adsorbed molecule and solid surface. However, the structure of only adsorbed molecule changes on chemical adsorption caused by the strongly interaction between molecule and the solid surface through an electronic interaction. On the contrary, solid structure merely changes accompanying without the change of the molecular structure on absorption. Occlusion, the residual

interaction mode, gives rise to simultaneous changes of molecule and solid to produce a new lattice. Thus, in this study, occlusion or sorption can be used to describe CO_2 capture of K_2CO_3 and Na_2CO_3 with crystal structure changes under moist conditions.

Aim to different pore sizes and the interaction between molecule and the solid surface, adsorption isotherm can provide the primary information to describe adsorption properties at solid-gas interface.

2.1.1 Adsorption isotherm

The relationship of adsorption equilibrium between the quantity of the adsorbed gas expressed in moles per gram of the solid material (n) and the adsorption temperature (T), the pressure of the gas (p) and interaction potential between the gases and solid surface is described as follows.

$$n = f(p, T, E) \tag{2-1}$$

In general, adsorption measurements are carried out for a given gas adsorbed on a particular solid at constant temperature T. Then the equation can be expressed simply as

$$n = f(p)_{T, E} \tag{2-2}$$

This relation is called the adsorption isotherm. If the temperature is at or below the critical temperature of gas, the equation becomes

$$n = f(p/p_0)_{T, E} \tag{2-3}$$

where p_0 is saturation vapor pressure at the temperature T and p/p_0 is called relative pressure [6].

The adsorption isotherm, which demonstrates the unique condition of each type of isotherm, generally follows one of six types of adsorption isotherms adopted by IUPAC classification as shown in Figure 2-1 [7].

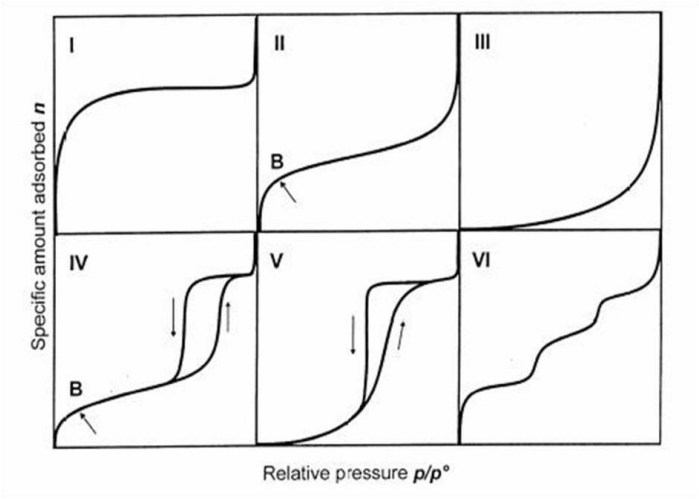

Figure 2-1: The IUPAC classification for adsorption isotherms [7].

According to IUPAC classification, Figure 2-1 observations show that Type I isotherm is known as Langmuir type on account of theoretically explained by Langmuir [8]. Type I isotherm could be observed typically in the chemisorption or specific physical adsorption with microporous adsorbents. The micropore filling predominantly at lower relative pressure and the long plateau shape of isotherm indicates mainly monolayer adsorption on the surface of adsorbent. The adsorption capacity of adsorbent is governed by the micropore volume of the material.

Type II isotherm is well known as BET type isotherm [9]. BET type isotherm is the most typical adsorption isotherm for many nonporous or macroporous adsorbents and represents multilayer adsorption. The knee of the Type Ⅱ isotherm, called Point B, is usually considered to indicate the completion of the monolayer formation and with increasing relative pressure, the beginning of the second, multilayer adsorption processes.

Type III isotherm is another BET type isotherm, and corresponds to the weaker interaction between adsorbates and adsorbents. Type IV isotherm is observed in the physical adsorption with mesoporous adsorbents, where the capillary condensation phenomena occurs, leading to the sharply jump in the uptake at higher pressure. In this case the isotherm possesses a hysteresis loop. The hysteresis means the disagreement of

adsorption and desorption branches and the desorption branch is over the adsorption branch until a certain pressure.

Type V isotherm also has a hysteresis loop. The difference between type V and type IV isotherms is the smaller intensity of the interaction forces between the adsorbate and the adsorbent. Type VI isotherm whose first step indicates the monolayer coverage represents stepwise multilayer by layer adsorption process on nonporous adsorbents with the uniform surface. Thus, it is called the stepwise isotherm.

2.1.2 Analysis methods of Adsorption isotherm

2.1.2.1 The Langmuir equation [8]

The Langmuir equation is used for the analysis of Type I isotherm. This equation is initially derived from the studies on the kinetic theory of gases and assumed that there is a definite and energetically equivalent number of adsorption site, indicating that the multilayer adsorption should not be occurred. The bonding to the adsorption sites can be either physical or chemical. Based on these assumptions, the Langmuir equation can be expressed as:

$$V_{\mathrm{a}} = \frac{V_m bP}{1 + bP} \qquad (2\text{-}4)$$

where V_a is the quantity of gas adsorbed at pressure P, b is an empirical constant and V_m is saturation adsorption capacity of gas adsorbed on the surface. The entire surface must be covered with a monomolecular layer, hence, V_m is the same to the monolayer capacity.

2.1.2.2 The Brunauer-Emmett-Teller (BET) equation [9]

The BET equation plays an important role in the surface area and porosity characterization of solid materials. The Brunauer-Emmett-Teller (BET) equation is an expansion of Langmuir model to multilayer adsorption occurred on the solid surface. The adsorption energy for the first layer is still stronger than that for more than two layers. Furthermore, since this adsorption equilibrium is dynamic, the actual location of

the surface sites covered by more than two layers might vary while the number of molecules in each layer will remain constant. The BET equation can be expressed by

$$\frac{P}{n(P_0 - P)} = \frac{1}{n_m C} + \frac{C-1}{n_m C} \times \frac{P}{P_0} \quad (2\text{-}5)$$

where the n (mol/g) is the adsorbed amount at relative pressure P/P_0, n_m is the monolayer adsorption capacity (mol/g) , and C is the constant value concerned with the energy of adsorption for the first layer. The equation (2-5) could change the formation to the equation (2-6).

$$\frac{x}{n(1-x)} = \frac{1}{n_m C} + \frac{C-1}{n_m C} x \quad (2\text{-}6)$$

where this BET equation is a linear function between $x/n(1\text{-}x)$ and x in the relative pressure range of 0.05 to 0.35, which is usually determined the specific surface area by applying to nitrogen adsorption data. The n_m and C are obtained from the slope and intercept of the BET plot.

The BET equation is mostly used to estimate the specific surface area of solid materials because of the comparatively strong adsorption due to the micropore filling [10]. The specific surface area is determined from the volume of adsorbed gas in the monolayer on the solid material

$$S = \frac{V_m \times N_A \times \alpha}{m \times 22400} \quad (2\text{-}7)$$

where S is specific surface area (m^2/g), N_A is the Avogadro's constant, α is the effective cross-sectional area of one adsorbed molecule (m^2) and m is mass of solid material (g).

2.2 Interactions of bicarbonate-carbonate or bicarbonate

In the preceding chapter, we have introduced that various occlusion reactions of CO_2 capture of K_2CO_3 and Na_2CO_3 under a moist condition may occur in the transformation process of bicarbonate. These formed compounds, such as $KHCO_3$, $K_4H_2(CO_3)_3 \cdot 1.5H_2O$ ($K_4(HCO_3)_2CO_3 \cdot 1.5H_2O$), $Na_5H_3(CO_3)_4$ ($Na_5(HCO_3)_3CO_3$) and $NaHCO_3$, contain the

anion bicarbonate (HCO_3^-) and dianion carbonate (CO_3^{2-}). References of involved compounds can be obtained through inorganic crystal structure database (ICSD). The main interaction motifs of HCO_3^- and CO_3^{2-} can be seen in Figure 2-2. The bicarbonate-bicarbonate or carbonate group form in various interaction motifs through O···H···O hydrogen bonds.

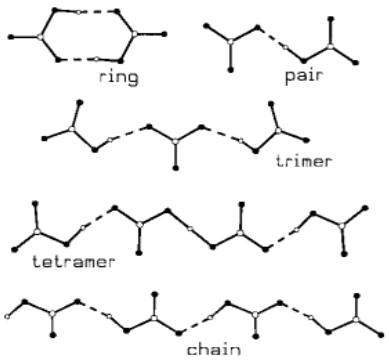

Figure 2-2: The interaction motifs of HCO_3^- ··· HCO_3^- (ring, chain) and HCO_3^- ··· CO_3^{2-} (pair, trimer, and tetramer) [11].

Table 2-2: The crystal structure involved in CO_2 capture of K_2CO_3 and Na_2CO_3.

ICSD code	Compound	Motifs	Space group	Crystal systems
2325 [12]	$KHCO_3$	ring	$P12_1/a1$	monoclinic
401721 [13]	$K_4(HCO_3)_2CO_3 \cdot 1.5H_2O$	trimer	Pbam	orthorhombic
18183 [14]	$NaHCO_3$	chain	$P12_1/c1$	monoclinic
68711 [15]	$Na_5(HCO_3)_3CO_3$	tetramer	P-1	triclinic
52535 [16]	K_2CO_3		$P6_3/mmc$	hexagonal
281362 [17]	Na_2CO_3		C12/m1	monoclinic

According to the interactions between bicarbonate-carbonate or bicarbonate, the main crystal structures involved in CO_2 capture of K_2CO_3 and Na_2CO_3 are summarized in Table 2-2. HCO_3^- group in $NaHCO_3$ forms an infinite chain structure through O···H···O hydrogen bonds (chain). In contrast, dimers ($(HCO_3^-)_2$) formed by HCO_3^- group in

$KHCO_3$ connect each other through double hydrogen bond (ring). Both HCO_3^- group and CO_3^{2-} group form trimer and tetramer, respectively, in $K_4H_2(CO_3)_3 \cdot 1.5H_2O$ and $Na_5H_3(CO_3)_4$ through O···H···O hydrogen bonds. In this study, the crystals will be characterized with various methods.

2.3 Characterization methods

2.3.1 Thermogravimetric-differential thermal analysis (TG-DTA)

Thermogravimetry (TG) is an important laboratory method used for material characterization, which is used as a technique to characterize materials used in various environmental, food, pharmaceutical, and petrochemical applications [18].

Thermogravimetric analysis measures the amount of the mass change of a sample by monitoring as a function of temperature or time in an atmosphere of Nitrogen, Helium, Argon, Oxygen, other gas or in vacuum. A TG instrument mainly consists of a sample pan, a precision balance and a furnace. The sample pan is supported by the precision balance and resides in a furnace when the samples need to be heated or cooled during the experiment [19].

According to the orientation of supported precision balance, TG instruments can be divided into two general types such as vertical and horizontal balance. Vertical balance instruments only have a sample pan hanging from the balance or located above the balance on a sample stem in order to compensate for buoyancy effects due to the variation in the density of the purge gas with temperature. In contrast, horizontal balance instruments generally have two pans (sample and reference) and can perform differential thermal analysis (DTA) measurements without the buoyancy effects [20]. DTA is used to record the temperature difference between the reference pan and sample pan. During TG-DTA measurements, qualitative and quantitative analysis can be performed by studying various reactions and interactions between a sample and special atmosphere. Also reaction mechanisms can be examined and analyzed on the base of

TG-DTA curves variation. Consequently, in the dissertation, the capacity, exothermic properties and kinetics of CO_2 capture in K_2CO_3 and Na_2CO_3 are obtained by TG-DTA measurements.

2.3.2 X-Ray Diffraction (XRD)

X-rays are electromagnetic radiation of wavelength about 1 Å, which is about the same size as an atom. If we can probe the atomic distances, this can exactly provide information about structures that we need. Generally, X-rays are produced by bombarding a metal target (Cu or Mo) with a beam of electrons accelerated by a high voltage, which emitted from a heated filament (tungsten). If the incoming electrons are energetic enough, the beam of electrons can ionize electrons from the K shell (1s) of the target atom leading to resultant vacancies. To attain a lower energetic state, Atom will fill these vacancies by electrons dropping down from the L (2P) or M (3p) shell. The difference between the electron energies of the K shell and L or M shell is emitted in form of characteristic x-rays during this process. In general, two lines (Kα1 and Kα2) of different energies in Kα are produced between K shell and L shell while a line (Kβ) is produced between K shell and M shell [21].

The interactions of X-rays with matter are mainly absorption, scattering. Particularly, as one of X-rays scattering phenomenon, X-ray diffraction is that the atomic planes of a matter cause an incident beam of X-rays to interfere with one another as they leave the crystal [22]. X-ray diffraction can be explained by the Bragg's law.

$$2d\sin\theta = n\lambda \qquad (2\text{-}8)$$

Here, d is the distance between atomic layers in a crystal; θ is angle of incidence of reflect X-ray beam; λ is the wavelength of the incident X-ray beam; n is an integer.

X-ray diffraction is one of the most important techniques to characterize the crystallographic structure and crystallite size. Each crystalline solid has its unique characteristic X-ray powder pattern. Once the material has been identified, X-ray

crystallography may be used to determine its structure [21]. According to XRD pattern to confirm the crystal structure, the crystallite size can be quantified using the Scherrer equation based on the XRD data. In this study, the XRD technique is used to investigate the crystal structural changes and crystallite size with the occlusion reaction time of K_2CO_3 and Na_2CO_3 under different CO_2 concentrations and moist conditions.

2.3.3 Scanning Electron Microscopy (SEM)

Scanning electron microscopy (SEM) is one of electron microscopes that use accelerated electrons as a source of illumination to obtain information about crystalline structure, chemical composition and morphology such as the surface features, shape and size [23]. In an SEM, the high energy carried by accelerated electrons is dissipated as a variety of signals produced by electron-sample interactions when the incident electrons are decelerated in specimen. These signals include secondary electrons, backscattered electrons, diffracted backscattered electrons, photons, visible light and heat [24]. Especially, secondary electrons produce the SEM image for showing morphology and topography while backscattered electrons are most valuable for illustrating contrasts in composition in multiphase specimen. SEM considered as "non-destructive" method visualizes the surface structure of the specimen, providing a 3-D impression. On the other hand, SEM analysis can be used to analyze the specimen repeatedly because x-rays generated in a SEM do not lead to volume loss of specimen [24]. Therefore, in the study, SEM method is used to examine the morphology variation with reaction time of K_2CO_3 and Na_2CO_3 under different CO_2 concentrations and moist conditions.

References

[1] B. Kasemo. Biological surface science. *Curr. Opin. Solid State Mater. Sci.*, **1998**, 3, 451–459.

[2] R. A. Van Santen, P. W. N. M. van Leeuwen, J. A. Moulijn, B. A. Averill. Catalysis an Integrated Approach Studies in Surface Science and Catalysis, *Elsevier*, Amsterdam, **1999**.

[3] F. Rouquerol, J. Rouquerol, K. Sing. Adsorption by Powders and Porous Solid, *Academic press*, London, **1999**.

[4] A. Geol. Surface Chemistry, *Discovery Publishing House Press*, New Delhi, 2006.

[5] H. Noguchi, A. Kondo, D. Noguchi, D. Y. Kim, T. Ohba, C. M. Yang, H. Kanoh, K. Kaneko. *J. Chem. ENG. Japan*, **2007**, 40, 1159−1165.

[6] S. J. Gregg, K. S. W. Sing. Adsorption, Surface Area and Porosity, *Academic Press*, London, **1991**.

[7] K. S. W. Sing, D. H. Everett, R. A. W. Haul, L. Moscou, R. A. Pierotti, J. Rouquerol, T. Siemieniewska. *Pure Appl. Chem.*, **1985**, 57, 603−619.

[8] I. Langmuir. *J. Am. Chem. Soc.*, **1918**, 40, 1361−1403.

[9] S. Brunauer, P. H. Emmett, E. Teller. *J. Am. Chem. Soc.*, **1938**, 60, 309−319.

[10] K. Kaneko, R. F. Cracknell, D. Nicholson. *Langmuir*, **1994**, 10, 4606−4609.

[11] D. Braga, E. D. Oria, F. Grepioni, F. Mota, J. J. Novoa, C. Rovira. *Chem. Eur. J.*, **2002**, 8, 1173−1180.

[12] J.O. Thomas, R. Tellgren, I. Olovsson. *Acta Crystallogr. B*, **1974**, 30, 2540−2549.

[13] V. Cirpus, A. Adam, Z. Anorg. *Allgem. Chem.*, **1995**, 621, 1197−1204.

[14] B. D. Sharma. *Acta Crystallogr.*, **1965**, 18, 818−820.

[15] N. G. Fernandes, R. Tellgren. *Acta Crystallogr.*, **1990**, 46, 466−474.

[16] C. Zhao, X. Chen, C. Zhao. *Chemosphere*, **2009**, 75, 1401-1404.

[17] Y. Liang. M.S. Dissertation, LSU, Baton Rouge, LA, 2003.

[18]http://www.perkinelmer.com/cmsresources/images/44-74556gde_tgabeginnersguide.pdf

[19] http://www.andersonmaterials.com/tga.html

[20]http://www.uzaktanegitimplatformu.com/UEP/uep_ylisans/ey2/ey2_download/Practice%20Guide_Section%202_TGA.pdf

[21] V. Hauk. Structural and Residual Stress Analysis by Nondestructive Methods, *Elsevier*, **1997**.

[22] I.C. Noyan, J. B. Cohen. Residual stress measurement by diffraction and interpretation, *Springer-Verlag*, New York, **1987**.

[23] P. J. Goodhew, J.Humphreys, R. Beanland. Electron microscopy and analysis, *Taylor and Francis*, New York, **2001**.

[24] J. Goldstein. Scanning electron microscopy and x-ray microanalysis, *Kluwer Adacemic/Plenum Pulbishers*, **2003**.

Chapter 3: Fundamentals in CO_2 Sorptivity of K_2CO_3

3.1 Introduction

As the rapid increase in CO_2 emissions from human activities is considered to be the main cause of global warming, reduction of CO_2 emissions has become an urgent global issue. Carbon capture and storage (CCS) can provide an immediate solution by stabilizing or reducing the atmospheric CO_2 concentration via development of CO_2 sequestration methods and accompanying renewable energy technologies [1–5]. The main focus of this field has been placed on amine-, Zeolite13X-, and activated-carbon-based CO_2 capture [6–8]. However, these technologies still face challenges, such as high energy consumption during sorbent regeneration, amine loss during regeneration, and low amine utilization efficiency. Furthermore, Zeolite13X- and activated-carbon-based CO_2 sorbents under ambient conditions have CO_2 efficiency issues because of interference between adsorbed CO_2 and H_2O as well as high cost for gas removal. Furthermore, these sorbents are not appropriate for CO_2 capture applications under moist conditions.

Feasible CO_2 capture sorbents must provide significant enhancement in the capture or sorption rate, saturated sorption amount, and stability for long-term CO_2 capture. Zhao et al. discovered that K_2CO_3 derived from $KHCO_3$ showed excellent CO_2 capture capacity. This can be used to solve the problem of an overall low CO_2 sorption rate [9]. The practical application of K_2CO_3 as a CO_2 sorbent has already been demonstrated on a pilot scale in an actual coal-fired power plant [10, 11]. Conversely, K_2CO_3 as a CO_2 sorbent under moist conditions at atmospheric pressure has been studied extensively as the following reaction [9, 12–21]:

$$K_2CO_3\ (s) + CO_2\ (g) + H_2O\ (g) \leftrightarrows 2\ KHCO_3\ (s) \quad (3\text{-}1)$$

where the forward, exothermic reaction (termed "bicarbonate formation") is the formation of $KHCO_3$ (the theoretical CO_2 capture amount of K_2CO_3 is 7.24 $mmol \cdot g^{-1}$), while the reverse, endothermic reaction is the decomposition of $KHCO_3$. A low temperature increases the CO_2 sorption amount of K_2CO_3 according to the forward reaction of eq (3-1); thus, K_2CO_3 may be used at room temperature for a highly saturated sorption value. Moreover, Chioyama et al. found that the occlusion amount (6.48 $mmol \cdot g^{-1}$, 285 $mg \cdot g^{-1}$) at 0.1 MPa and 313 K was superior to that at a higher temperature and showed that K_2CO_3 could be used at room temperature [22]. Furthermore, the favorable CO_2 occlusion performance of K_2CO_3 supported on activated carbon at a low temperature has also been demonstrated by enhancing the surface area [23]. Consequently, K_2CO_3 is especially promising as a CO_2 sorbent material for moist conditions at room temperature.

However, most previous studies regarding CO_2 capture of K_2CO_3 were carried out at relatively high temperatures (>333 K) under atmospheric pressure. In numerous studies on the CO_2 sorption of K_2CO_3 under moist conditions, CO_2 capture did not always proceed directly via reaction (3-1). Hayashi et al. reported significantly improved CO_2 capture capacity using $K_2CO_3 \cdot 1.5H_2O$ as the active species under flue gas conditions of 13.8% CO_2 with 10% H_2O in helium at 373 K [18]. Shigemoto et al. proposed that K_2CO_3 supported on activated carbon could be converted to $KHCO_3$ through the reaction of $K_2CO_3 \cdot 1.5H_2O$ with CO_2 under moist flue gas (10 % H_2O, 11.8 % CO_2) at 363 K. The relevant reactions are [19]:

$$K_2CO_3\ (s) + 1.5H_2O\ (g) \rightleftarrows K_2CO_3 \cdot 1.5H_2O\ (s) \quad (3\text{-}2)$$

$$K_2CO_3 \cdot 1.5H_2O\ (s) + CO_2\ (g) \rightleftarrows KHCO_3\ (s) + 0.5H_2O\ (g) \quad (3\text{-}3)$$

Bicarbonate formation of K_2CO_3 on Al_2O_3 was achieved via reactions (3-2) and (3-3) rather than reaction (3-1), as reported by Seo et al., [20], and performed under a 10

vol% CO_2, 12.2 vol% H_2O, and 77.8 vol% N_2 [20] atmosphere within a temperature range of 323–343 K. In addition, Lee et al. [21] presented similar bicarbonate formation of K_2CO_3 on Al_2O_3 under a 1 vol% CO_2, 9 vol% H_2O, and 90 vol% N_2 [21] atmosphere at above 323 K. However, Zhao et al. suggested that the formation of $K_4H_2(CO_3)_3 \cdot 1.5H_2O$ may also play an important role in bicarbonate formation of K_2CO_3 [24] and would proceed via reactions (3-4) and (3-5) instead of reaction (3-1) in an atmosphere of 15 mol % CO_2, 15 mol % H_2O, and 70 mol% N_2 at 333 K [25]:

$$2K_2CO_3\,(s) + 2.5H_2O\,(g) + CO_2\,(g) \rightleftarrows K_4H_2(CO_3)_3 \cdot 1.5H_2O\,(s) \quad (3\text{-}4)$$

$$K_4H_2(CO_3)_3 \cdot 1.5H_2O\,(s) + CO_2\,(g) \rightleftarrows 4KHCO_3 + 0.5H_2O\,(g) \quad (3\text{-}5)$$

These reactions were shown to proceed differently dependent on the experimental conditions, and the different kinetics of CO_2 sorption reactions of K_2CO_3 were demonstrated in these works based on a mechanistic interpretation. However, no detailed report on temperature and crystal structure changes with reaction time has been conducted at low temperatures. The morphologies of K_2CO_3 particles also change as the reactions advance, as the crystal growth depends on the reaction conditions. This information is also important for understanding the kinetic behavior of K_2CO_3 particles. However, details of the morphological variations with reaction time have not been reported; thus, the CO_2 capture mechanism under various CO_2 and H_2O conditions is currently unclear.

In this chapter, CO_2 sorptivity of K_2CO_3 under various temperatures, CO_2 and H_2O concentrations were examined by thermogravimetric-differential thermal analysis (TG-DTA) and accompanying structural changes with reaction time were investigated using the X-ray diffraction (XRD) method under vacuum. In addition, morphological variations with reaction time were observed using scanning electron microscopy (SEM). On the basis of the crystal structure and kinetic analysis of bicarbonate formation of K_2CO_3, the dependence of CO_2 capture of K_2CO_3 on CO_2 concentration and humidity

was explained in details. CO_2 sorptivity of $K_4H_2(CO_3)_3 \cdot 1.5H_2O$ was also investigated with XRD and SEM. Three relevant reactions were proposed as fundamental pathways in the $KHCO_3$ formation from K_2CO_3 at low temperatures.

3.2 Experimentals

3.2.1 Sample preparation

Analytical-reagent-grade $KHCO_3$ (99.5 % chemical purity, Wako Chemical Co., Ltd.) was used throughout the decomposition experiments of $KHCO_3$ and bicarbonate formation measurements of K_2CO_3. The decomposition of $KHCO_3$ was processed with TG–DTA (Shimadzu, DTG–60AH). $KHCO_3$ (44–50 mg) was heated at 5 $K \cdot min^{-1}$ from 298 to 473 K in an atmosphere of pure N_2 at 100 $cm^3 \cdot min^{-1}$ to form K_2CO_3 and held at these conditions for 5 min to complete the decomposition. Subsequently, the temperature was lowered to 313 K at -5 $K \cdot min^{-1}$ and maintained for 30 min under a N_2 atmosphere.

After the decomposition of $KHCO_3$, the temperature was lowed from 473 to 383 K at -5 $K \cdot min^{-1}$ and kept for 20 min under an N_2 atmosphere. Subsequently, the formation of $K_4H_2(CO_3)_3 \cdot 1.5H_2O$ were performed with TG-DTA in the composition of CO_2 and water vapor for 120 min at 383 K and then in flowing N_2 at above temperature for 25min. Then the temperature was lowed again to 313 K at -5 $K \cdot min^{-1}$ and kept for 12 min under a N_2 atmosphere. The samples were saved in the vacuum oven at 303 K.

3.2.2 Bicarbonate formation measurements

The $KHCO_3$ samples (30–50 mg) mounted in a platinum pan were set in an atmosphere of pure nitrogen at 100 $cm^3 \cdot minute^{-1}$ and heated at 5 $K \cdot min^{-1}$ from room temperature to 473 K in order to form K_2CO_3, in accordance with the reverse reaction (3-1). The obtained samples were processed using a gas composition of CO_2 and H_2O (v/v of 98.2:1.8) at a flow rate of 100 $cm^3 \cdot min^{-1}$ at temperatures between 313 and 383 K.

Measurement of the K_2CO_3 bicarbonate formation with varying reaction duration times was performed with the TG–DTA apparatus with various compositions of CO_2 and

N_2 containing saturated water vapor at 313 K. CO_2 and N_2 were obtained from high-purity gas cylinders equipped with mass flow controllers to control the flow rate. H_2O vapor was produced by flowing N_2 and CO_2 into distilled water in a bubbler for more than 5 h to reach saturation, with N_2 as the balance gas.

The bicarbonate formation of $K_4H_2(CO_3)_3 \cdot 1.5H_2O$ were performed with TG-DTA with different composition of CO_2 and N_2 containing saturated water vapor or under pure CO_2 for 120 min at 313 K.

On the other hand, measurements of the bicarbonate formation of K_2CO_3 with varying reaction duration were performed with the TG-DTA apparatus under different H_2O concentrations at the CO_2 flow rate of 30 $cm^3 \cdot min^{-1}$. Here H_2O concentration was controlled by flowing N_2 into distilled water in a bubbler and another N_2 used as dry gas in a bubbler.

During above various types of bicarbonate formation measurements, the mixed CO_2, H_2O, and N_2 gas was then introduced into a moisture detector with a thermometer and hygrometer at 313 K. The relative humidity (RH) of the mixed gas was measured with the hygrometer. The total gas flow rate was maintained at 100 $cm^3 \cdot min^{-1}$ for all experiments.

3.2.3 Characterization

The crystal structures of the products after reaction times of 1, 5, 20, 40, 60, and 120 min were measured by XRD (MAC Science, M03XHF) under vacuum to avoid occlusion of CO_2 or H_2O from the ambient atmosphere. The powder XRD patterns were obtained in the 2θ range of 25 to 45° using Cu Kα radiation (40 kV, 25 mA, and $\lambda = 0.15406$ nm) at room temperature. The morphology of the particles before and after CO_2 capture for the different reaction times was observed by using scanning electron microscopy (SEM; JEOL, JSM–6510A) after coating the samples with metallic osmium.

3.3 Results and discussion

3.3.1 CO_2 capture of K_2CO_3 at different temperatures

$KHCO_3$ decomposed to K_2CO_3, CO_2 and H_2O according to the reverse reaction of reaction (3-1). This was confirmed by a weight decrease (between 20 and 35 minutes from the initiation of reaction) upon heating to 473 K, as shown in Figure 3-1. The sample weight eventually decreased to 69.1% (±0.1%) following the heat treatment. Because the theoretical value based on reaction (3-1) is 69.0%, the decomposition proceeded completely. After the decomposition, a mixture of CO_2 and H_2O was supplied to K_2CO_3 at different temperatures. The increase in sample weight depended on temperature, as shown in Figure 3-1. This could be attributed to the bicarbonate formation of K_2CO_3 with CO_2 and H_2O. The change increased more rapidly at higher temperatures because bicarbonate formation requires a minimum activation energy for the chemical reaction to occur. The initial formation rate is much faster at 383 K than at lower temperatures.

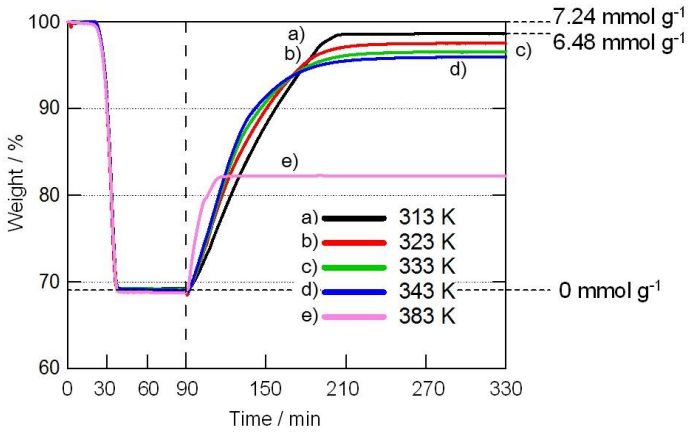

Figure 3-1: Weight change by the decomposition of $KHCO_3$ (<40 min) at 473 K and the bicarbonate formation of K_2CO_3 with CO_2 and H_2O (>90 min) at different temperatures: a) 313 K, b) 323 K, c) 333 K, d) 343 K, e) 383 K.

However, the saturated occlusion amount at 383 K was lower than half of the theoretical value of 7.24 mmol·g^{-1}. By contrast, the initial formation rate is slower at 313 K, but the saturated occlusion amount was 6.48 mmol·g^{-1}, which is 89.3% of the theoretical amount (i.e. 7.24 mmol·g^{-1}). The CO_2 occlusion amount of 6.48 mmol·g^{-1}

(285 $mg \cdot g^{-1}$) is exceedingly high at 0.1 MPa and 313 K under a moist atmosphere in comparison with the CO_2 adsorbed on activated carbon fibres by physical adsorption (120–200 $mg \cdot g^{-1}$ at 273 K) [24]. Thus, K_2CO_3 is a promising material for CO_2 sorption under ambient condition. The CO_2 occlusion by K_2CO_3 under moist conditions was examined at relatively high temperatures (i.e. >333 K) in most of the previous reports, but K_2CO_3 should be used at room temperature to achieve the highest saturated occlusion amount.

Because the temperature dependence of the saturated occlusion amount is not yet understood, XRD patterns were obtained for the samples treated at different temperatures to examine the structural changes of K_2CO_3 following CO_2 occlusion. The patterns of the CO_2–occluded samples at different temperatures are shown in Figure 3-2. All peaks of the sample formed at 383 K were assigned to the $K_4H_2(CO_3)_3 \cdot 1.5H_2O$ phase. Thus, no formation of $KHCO_3$ was observed at 383 K. The XRD patterns showed peaks consistent with two phases, that is, $KHCO_3$ and $K_4H_2(CO_3)_3 \cdot 1.5H_2O$, at temperatures from 313 to 343 K. The peaks attributed to the $KHCO_3$ phase appeared at 343 K, and the peak intensity increased with decreasing temperature, but the peaks of $K_4H_2(CO_3)_3 \cdot 1.5H_2O$ remained at 323 and 313 K. There was also the formation of $KHCO_3$ from $K_4H_2(CO_3)_3 \cdot 1.5H_2O$ and the reaction continued through reactions (3-4) and (3-5) [16]. These two reactions, however, were not intensively considered for the CO_2 occlusion of K_2CO_3.

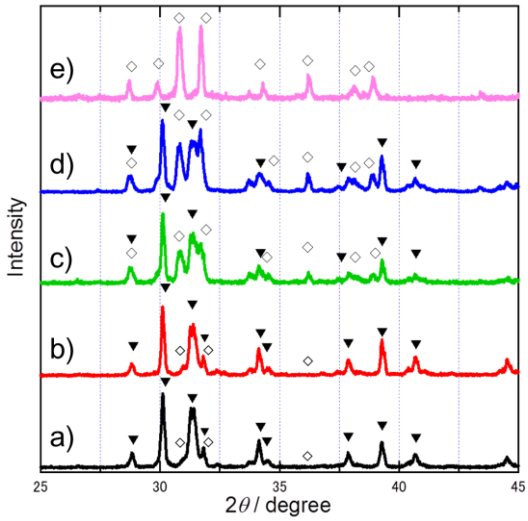

Figure 3-2: XRD patterns of CO_2 occluded samples at different temperatures: a) 313 K, b) 323 K, c) 333 K, d) 343 K, e) 383 K. ▼: $KHCO_3$, ◇: $K_4H_2(CO_3)_3 \cdot 1.5H_2O$

The XRD results showed that only reaction (3-4) proceeded at 383 K, whereas reaction (3-5) proceeded at rather lower temperatures. Figures 3-3 (a and b) show the derivative thermogravimetric (DTG) curves and DTA curves, respectively, obtained at 313, 323, 333 and 343 K, which indicate exothermic reactions. The DTG curves were obtained by differentiating the weight change in Figure 1 over time. Evidently, both curves show a similar shape: (i) The curves consist of two components. (ii) The first peak intensity increases with the increase in temperature, whereas the second peak intensity decreases with temperature increase. Thus, the bicarbonate formation of K_2CO_3 likely involves a double-step reaction.

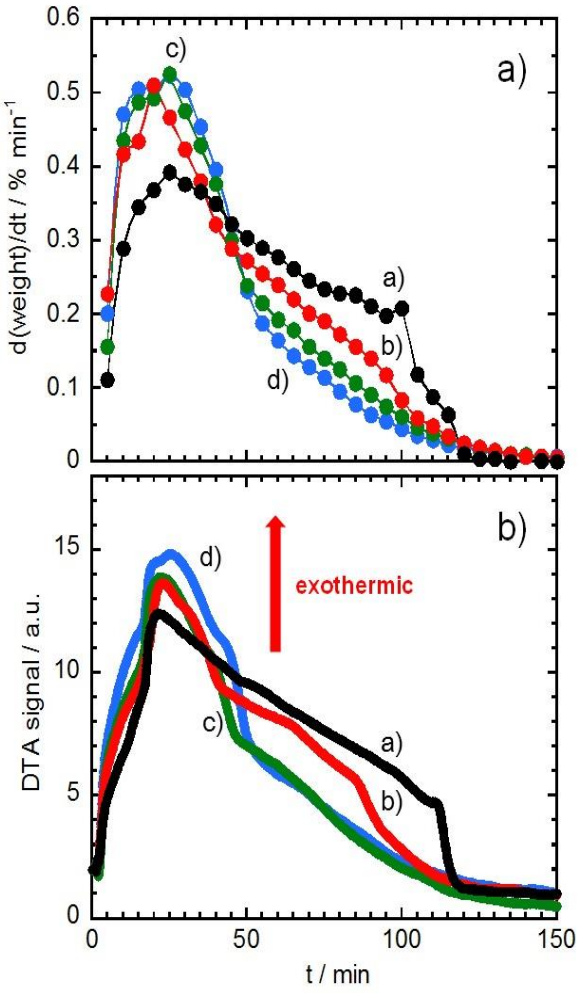

Figure 3-3: DTG (upper) and DTA curves (lower) over time at different temperatures: a) 313 K, b) 323 K, c) 333 K, d) 343 K.

The XRD patterns of pure $KHCO_3$ and $K_4H_2(CO_3)_3 \cdot 1.5H_2O$ phases are shown at the bottom of Figure 3-4, where peak intensities for each phase are kept as relative ratios. The experimental patterns obtained at 323 K (Figure 3-2b) and 313 K (Figure 3-2a) using the peak patterns of these pure phases gave well-fitted patterns, which are shown in Figures 3-4 (a) and (b), respectively. This indicates that these crystals only consist of these two phases.

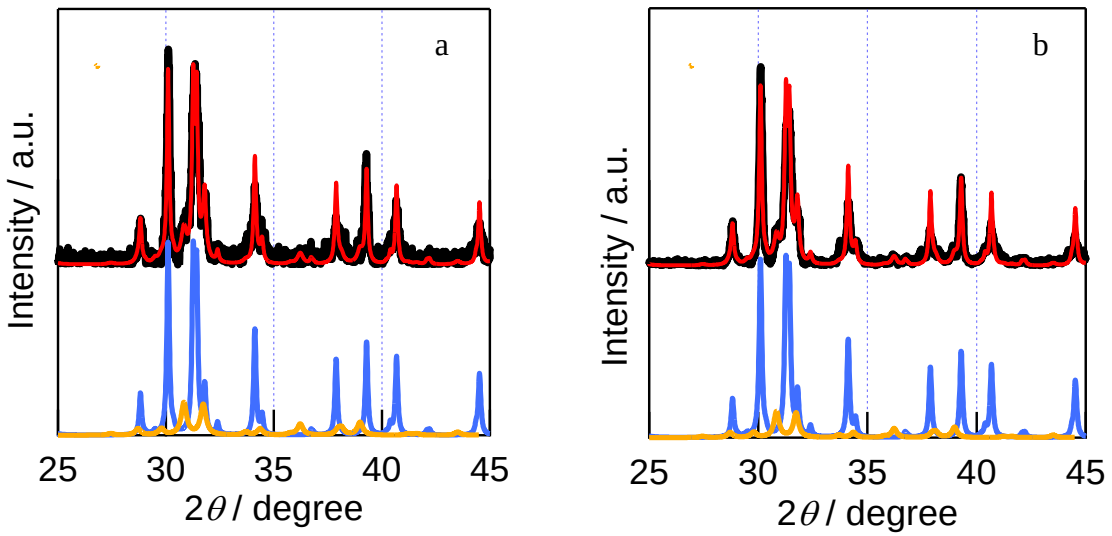

Figure 3-4: Peak fitting of XRD peaks of pure phases to the experimental results obtained at 323 K (a) and 313 K (b). Black: experimental pattern; Red: fitted pattern obtained by using a pattern of pure $KHCO_3$ (blue) and pure $K_4H_2(CO_3)_3 \cdot 1.5H_2O$ (orange).

The peak areas were obtained for the two phases by the peak fitting. The calculation of the peak area for each peak provided a ratio of the peak area of $KHCO_3$ to the total peak area of $KHCO_3$ and $K_4H_2(CO_3)_3 \cdot 1.5H_2O$, $I_{KHCO_3}/\left(I_{KHCO_3} + I_{K_4H_2(CO_3)_3 \cdot 1.5H_2O}\right)$, as shown in Figure 3-5. It was found that the ratio of the $KHCO_3$ phase increased with decreasing temperature. The $KHCO_3$ phase was not observed at 383 K, and it was concluded that reaction (3-5) does not proceed at 383 K, whereas reaction (3-4) does. The two exothermic peaks were observed at time of about 30 min and 100 min, respectively, in the DTA curves of Figure 3(b). Accordingly, reactions (3-4) and (3-5) should be unfavourable at higher temperatures according to Le Châtelier's principle. At temperatures from 313 to 383 K, reaction (3-4) can proceed to a certain extent. However, reaction (3-5) probably shows a stronger temperature dependence, and little formation of $KHCO_3$ proceeds at 383 K or higher. This should be considered while developing an efficient system for CO_2 occlusion of K_2CO_3 under moist conditions.

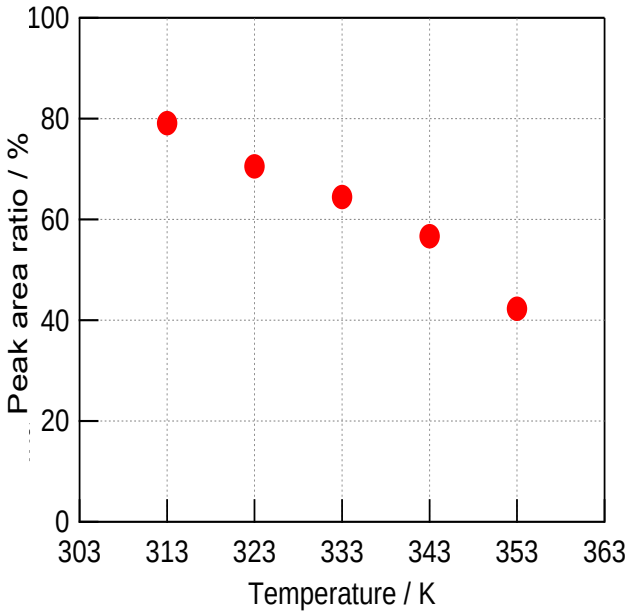

Figure 3-5: Temperature dependence of the peak area ratio of $KHCO_3$ to the total peak area of $KHCO_3$ and $K_4H_2(CO_3)_3 \cdot 1.5H_2O$.

In conclusion, the TG-DTA and X-ray powder diffraction analyses show that the bicarbonate formation of K_2CO_3 with CO_2 and H_2O involves two exothermic reactions. The first step proceeds relatively easily, whereas the second step depends on the temperature. At higher temperatures, the second step does not readily proceed. This is because the second step should be thermodynamically controlled based on Le Châtelier's principle. These results also provide useful information for the practical use of K_2CO_3 in CCS technology.

3.3.2 CO_2 capture of K_2CO_3 under various CO_2 concentrations

To examine the effect of the CO_2 concentration on the sorptivity of K_2CO_3, TG data for the bicarbonate formation of K_2CO_3 were obtained under various partial pressures of CO_2, as shown for reaction times of 0–120 min in Figure 3-6.

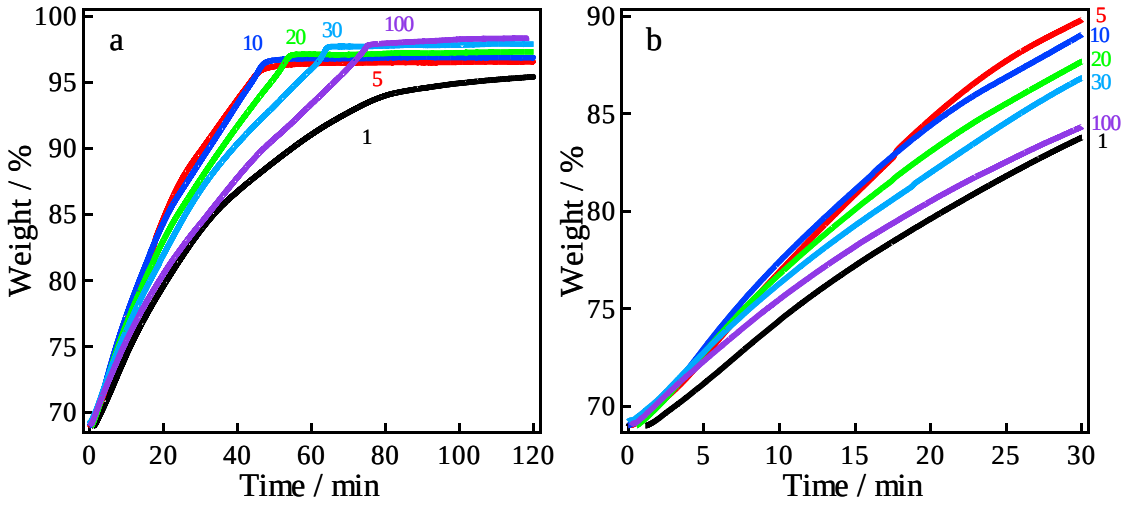

Figure 3-6: TG curves (a) for bicarbonate formation under various CO_2 flow rates ($cm^3 \cdot min^{-1}$), which are indicated with numbers, with N_2 and H_2O and magnified for 0–30 min (b).

A sufficiently humid atmosphere (RH of 68% at 313 K) was supplied to K_2CO_3 with a mixed gas of CO_2 and N_2 containing saturated water vapor. When the flow rate of CO_2 was only 1 $cm^3 \cdot min^{-1}$ + 99 $cm^3 \cdot min^{-1}$ N_2 [1%(v/v) CO_2], the sorption amount was 6.24 $mmol \cdot g^{-1}$, which is 86.2% of the theoretical amount of 7.24 $mmol \cdot g^{-1}$. As the CO_2 flow rate increased from 1 to 30 $cm^3 \cdot min^{-1}$, the sorption amount of K_2CO_3 increased from 6.24 to 6.85 $mmol \cdot g^{-1}$. According to reaction (3-1), a high CO_2 concentration leads to an equilibrium shift toward bicarbonate formation of K_2CO_3. The sorption amount was 6.92 $mmol \cdot g^{-1}$, when the CO_2 flow rate was 100 $cm^3 \cdot min^{-1}$, which is 95.6% of the theoretical value. In comparison to the CO_2 sorption amount at a CO_2 flow rate of 30 $cm^3 \cdot min^{-1}$, the experimental results indicated that increasing the CO_2 concentration resulted in a greater conversion of K_2CO_3 to $KHCO_3$ in the presence of saturated water vapor at 313 K. Figure 3-7 shows the XRD patterns after the completed occlusion (120 min marked in Figure 3-6) at various CO_2 flow rates. It is evident that the peaks of both $K_4H_2(CO_3)_3 \cdot 1.5H_2O$ and $KHCO_3$ phases were present in all samples, while the peaks of the $K_4H_2(CO_3)_3 \cdot 1.5H_2O$ phase appeared to decrease with increasing CO_2 concentration,

which were consistent with the TGA data.

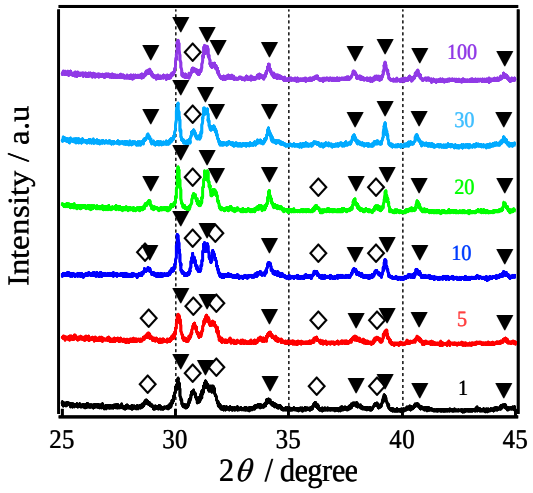

Figure 3-7: XRD patterns after CO_2 occlusion of K_2CO_3 at various CO_2 flow rates ($cm^3 \cdot min^{-1}$), which are indicated with numbers. ▼: $KHCO_3$; ◇: $K_4H_2(CO_3)_3 \cdot 1.5H_2O$.

However, bicarbonate formation was slow at CO_2 flow rates of 20–100 $cm^3 \cdot min^{-1}$. In contrast, bicarbonate formation at CO_2 flow rates of 5 and 10 $cm^3 \cdot min^{-1}$ was much faster than other CO_2 flow rates, as seen in Figure 1b. It was shown that the layer of transformed $KHCO_3$ on the interface of K_2CO_3 particles inhibited the CO_2 and H_2O transfer process because of increasing surface resistance [25]. On the other hand, the initial sorption rate was limited at CO_2 flow rates above 20 $cm^3 \cdot min^{-1}$, as seen in Figure 3-6b. It was previously reported that the formation of $K_2CO_3 \cdot 1.5H_2O$ as an active species could enhance the CO_2 capture capacity, with its formation being the limiting step [18, 19]. However, Zhao et al. discovered that the initial product after the reaction of K_2CO_3 with CO_2 and H_2O was not $K_2CO_3 \cdot 1.5H_2O$ but rather $K_4H_2(CO_3)_3 \cdot 1.5H_2O$. The bicarbonate formation rate of K_2CO_3 was much faster than that of $K_2CO_3 \cdot 1.5H_2O$ [24, 25]. Hence, the formation of the initial two products, their transformation processes, and the morphological variation on the surface of K_2CO_3 particles may influence the reaction rate of bicarbonate formation under different CO_2 flow rates. Investigation of the transformation process of K_2CO_3 and the associated changes in temperature during

bicarbonate formation is of the utmost importance for a better understanding of the CO_2 sorptivity kinetics of K_2CO_3.

Because the transformation process of K_2CO_3 to bicarbonate leads to a temperature change of the reaction system, the kinetic properties can be tracked by monitoring the temperature during the transformation under various CO_2 concentrations. Figure 3-8 shows the temperature curves (a), DTA curves (b), and derivative thermogravimetric (DTG) curves (c; obtained by differentiating the weight change in Figure 3-6 over time) for different CO_2 concentrations. Both DTA and DTG curves showed a striking similarity, exhibiting a series of peaks at the initial and final stages (close to equilibrium) corresponding to exothermic reactions of initial product formation from K_2CO_3 and initial product transformation to $KHCO_3$, respectively. In particular, temperature variation in the initial stage displayed remarkable similarity to both DTA and DTG curves at this stage, as shown in panels d–f of Figure 3-8, respectively.

There was a rapid increase in the temperature in the initial stage of the reaction (reaction time of < 5 min), as seen in Figure 3-8d. The maximum temperature of this initial stage increased with the CO_2 flow rate from 1 to 10 $cm^3 \cdot min^{-1}$, but decreased with a higher CO_2 flow rate. After the initial increase in the temperature, the temperature decreased moderately in all curves (middle stage). A second abrupt increase was observed for CO_2 flow rates between 20 and 100 $cm^3 \cdot min^{-1}$ when the CO_2 sorption was near equilibrium, arguably because of a successive exothermic reaction, although no marked peak was observed for CO_2 flow rates of 1 and 5 $cm^3 \cdot min^{-1}$. This second peak had an analogous peak in the DTA and DTG curves, as shown in panels b and c of Figure 3-8. The temperature at this stage (final stage) decreased upon the increase of the CO_2 flow rate from 20 to 100 $cm^3 \cdot min^{-1}$. These results indicate that both the overall reaction and the initial process of bicarbonate formation under a high CO_2 flow rate (above 20 $cm^3 \cdot min^{-1}$) proceed slowly, which can be understood together with analysis of the reaction mechanism of the system, as discussed below.

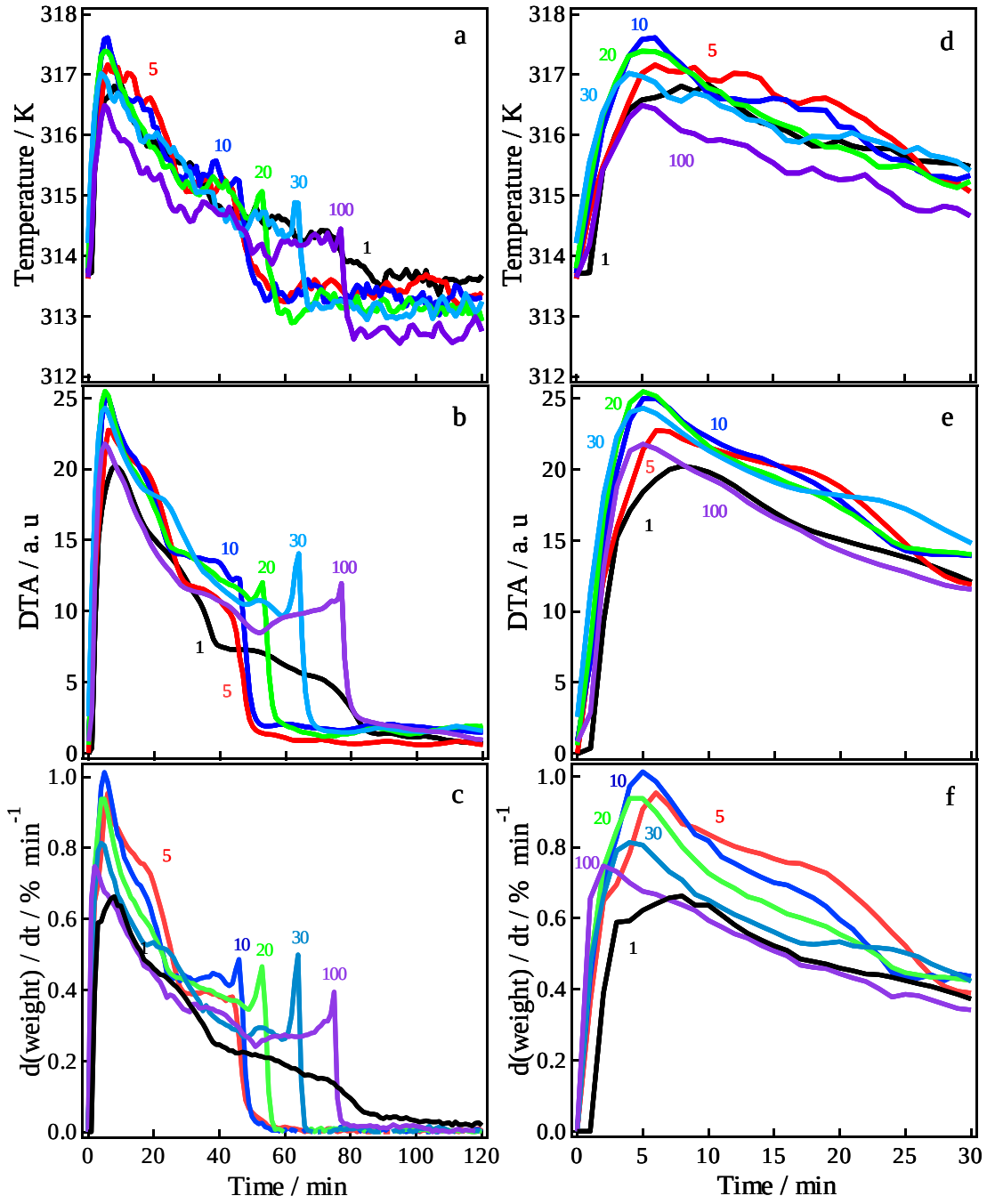

Figure 3-8: Temperature change (a), DTA (b), and DTG (c) curves at various CO_2 flow rates ($cm^3 \cdot min^{-1}$) at 313 K, which are indicated with numbers. These panels are magnified for reaction times of 0–30 min in panels d, e, and f, respectively.

The different pathways of bicarbonate formation of K_2CO_3 were examined by measuring the XRD patterns of CO_2–occluded samples of K_2CO_3 in the presence of

water vapor over various reaction times. There have been few reports related to the initial transformation process of K_2CO_3, and no detailed mechanisms have been reported thus far. Lee et al. reported that K_2CO_3 was transformed to $K_4H_2(CO_3)_3 \cdot 1.5H_2O$ upon treatment with water vapor, followed by further transformation from $K_4H_2(CO_3)_3 \cdot 1.5H_2O$ to $K_2CO_3 \cdot 1.5H_2O$ by drying in N_2 [26, 27]. It was also claimed that $K_2CO_3 \cdot 1.5H_2O$ was readily converted to K_2CO_3 at a low temperature under a slightly moist conditions, supported by the heat released from the exothermic reaction [26, 27].

However, our results, shown in Figure 3-9, indicate that the initial product of CO_2 occlusion of K_2CO_3 is not a simple transformation from K_2CO_3 to $K_2CO_3 \cdot 1.5H_2O$ and $K_4H_2(CO_3)_3 \cdot 1.5H_2O$. For the reaction occurring over 1 min, the XRD patterns (Figure 3-9a) showed the presence of two phases, $K_2CO_3 \cdot 1.5H_2O$ and $K_4H_2(CO_3)_3 \cdot 1.5H_2O$ phases, for all CO_2 flow rates. K_2CO_3 was completely converted to these two phases under humid conditions (RH of 68% at 313 ± 3 K). Thus, it can be concluded that the temperature changes are a result of the initial stage and the subsequent transformation processes.

Subsequently, when the reaction proceeded beyond 5 min, the peak intensity of $K_2CO_3 \cdot 1.5H_2O$ and $K_4H_2(CO_3)_3 \cdot 1.5H_2O$ in the XRD pattern significantly increased (Figure 3-9b). Upon increasing the reaction time to 20 min, the dominant peaks were found to originate from the $K_4H_2(CO_3)_3 \cdot 1.5H_2O$ phase. However, the peaks of $KHCO_3$ increased only slightly with increasing the CO_2 concentration. Furthermore, in compassion to the patterns obtained for the 5 min reaction, the XRD patterns after an occlusion reaction for 20 min showed that the peaks of $K_4H_2(CO_3)_3 \cdot 1.5H_2O$ increased considerably in intensity, while those of the $K_2CO_3 \cdot 1.5H_2O$ phase nearly disappeared. These changes indicate that $K_2CO_3 \cdot 1.5H_2O$ was converted to $K_4H_2(CO_3)_3 \cdot 1.5H_2O$ rather than $KHCO_3$. Accordingly, it can be concluded that $K_2CO_3 \cdot 1.5H_2O$ is the initial product in the bicarbonate formation process of K_2CO_3.

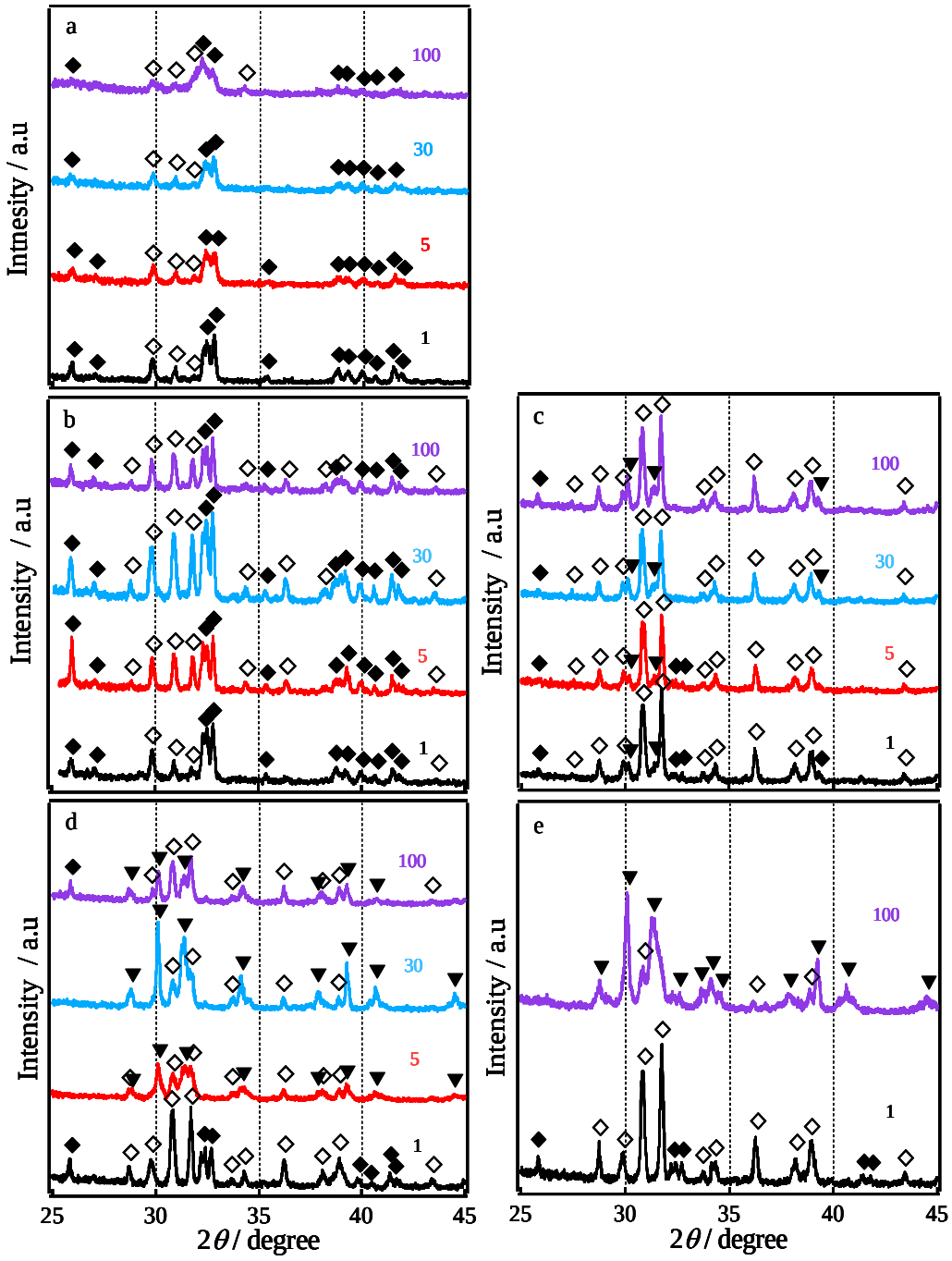

Figure 3-9: XRD patterns after CO_2 occlusion of K_2CO_3 at various CO_2 flow rates ($cm^3 \cdot min^{-1}$), which are indicated with numbers, with reaction time: (a) 1 min, (b) 5 min, (c) 20 min, (d) 40 min, and (e) 60 min. ▼: $KHCO_3$; ◇: $K_4H_2(CO_3)_3 \cdot 1.5H_2O$; ◆: $K_2CO_3 \cdot 1.5H_2O$.

Next, when the reaction time was extended to 40 min, the peak intensity of the $KHCO_3$ phase increased significantly, while the $K_4H_2(CO_3)_3 \cdot 1.5H_2O$ phase was diminished (Figure 3-9d). This result confirmed that $K_4H_2(CO_3)_3 \cdot 1.5H_2O$ was converted to $KHCO_3$ through reaction (3-5). At a low CO_2 flow rate (1 $cm^3 \cdot min^{-1}$), it was observed that the $K_2CO_3 \cdot 1.5H_2O$ phase still remained. This is a result of the unhindered transformation of $K_2CO_3 \cdot 1.5H_2O$ from $K_4H_2(CO_3)_3 \cdot 1.5H_2O$ based on the reversibility of the reaction in a dilute CO_2 atmosphere and saturated humidity at a low temperature. Conversely, at 100 $cm^3 \cdot min^{-1}$, the presence of the $K_2CO_3 \cdot 1.5H_2O$ phase also demonstrated the slow rate of CO_2 occlusion of K_2CO_3 under such a high CO_2 flow.

Upon increasing the reaction time to 60 min, Figure 3-9e shows peaks consisting of $K_4H_2(CO_3)_3 \cdot 1.5H_2O$ and $KHCO_3$ phase contributions under a CO_2 flow rate of 100 $cm^3 \cdot min^{-1}$, while $K_2CO_3 \cdot 1.5H_2O$ and $K_4H_2(CO_3)_3 \cdot 1.5H_2O$ phases were formed under a flow rate of only 1 $cm^3 \cdot min^{-1}$. The peaks of the $K_4H_2(CO_3)_3 \cdot 1.5H_2O$ phase were found to decrease at the flow rate of 100 $cm^3 \cdot min^{-1}$. These results were consistent with those of TGA and the final crystal structure observed under various CO_2 concentrations.

On the basis of the discussed transformation processes and kinetics of CO_2 sorptivity of K_2CO_3 under various CO_2 concentrations and in the presence of saturated water vapor, we can summarize the bicarbonate formation pathways of K_2CO_3 as follows instead of reaction (1):

$$K_2CO_3\ (s) + 1.5H_2O\ (g) \rightleftarrows K_2CO_3 \cdot 1.5H_2O\ (s) \quad (3\text{-}6)$$

$$2K_2CO_3 \cdot 1.5H_2O\ (s) + CO_2\ (g) \rightleftarrows K_4H_2(CO_3)_3 \cdot 1.5H_2O\ (s) + 0.5H_2O\ (g) \quad (3\text{-}7)$$

$$K_4H_2(CO_3)_3 \cdot 1.5H_2O\ (s) + CO_2\ (g) \rightleftarrows 4KHCO_3 + 0.5H_2O\ (g) \quad (3\text{-}8)$$

The crystallite size of $K_2CO_3 \cdot 1.5H_2O$, $K_4H_2(CO_3)_3 \cdot 1.5H_2O$, and $KHCO_3$ for each reaction time was estimated from the XRD patterns in panels a–d of Figure 3-9. The $K_2CO_3 \cdot 1.5H_2O$ and $K_4H_2(CO_3)_3 \cdot 1.5H_2O$ phases were found to grow more slowly with reaction time for high CO_2 flow rate (30–100 $cm^3 \cdot min^{-1}$) than for low CO_2 flow rate

(1–5 $cm^3 \cdot min^{-1}$), as shown in panels a and b of Figure 3-10. Furthermore, it was shown visually that the transformation from $K_4H_2(CO_3)_3 \cdot 1.5H_2O$ to $KHCO_3$ proceeded more slowly at high CO_2 flow rates (30–100 $cm^3 \cdot min^{-1}$) than that for low CO_2 flow rate (5 $cm^3 \cdot min^{-1}$), as shown for 20–40 min in Figure 3-10c. Thus, it can be confirmed that both the initial process and overall reaction of bicarbonate formation under high CO_2 flow rate (above 20 $cm^3 \cdot min^{-1}$) proceed more slowly. Both low temperatures and high CO_2 concentrations are favorable for an equilibrium shift toward bicarbonate formation, but the initial and final exothermic reaction properties and the CO_2 capture rate of K_2CO_3 under different CO_2 concentrations cannot be obtained from XRD data alone, as discussed below.

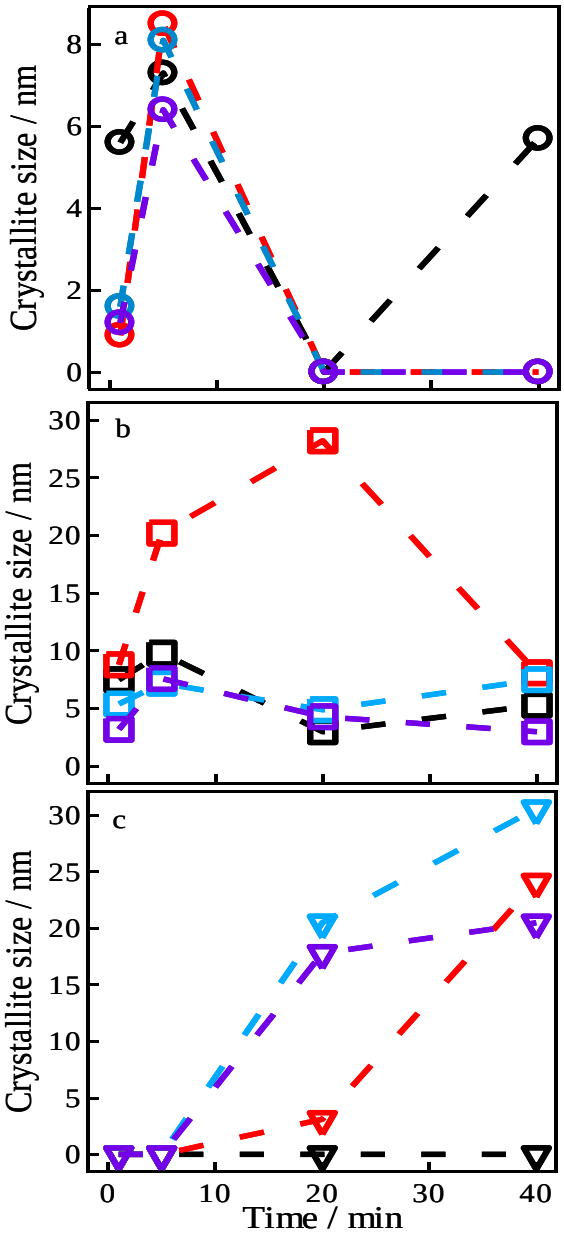

Figure 3-10: Crystallite size of $K_2CO_3 \cdot 1.5H_2O$ (a), $K_4H_2(CO_3)_3 \cdot 1.5H_2O$ (b) and $KHCO_3$ (c) at various CO_2 flow rates over reaction time obtained from XRD patterns in panels a–d of Figure 3-9 by using software Jade according to the Scherrer equation. The range of Bragg angle: 29–35 degree. CO_2 flow rate: black (1 $cm^3 \cdot min^{-1}$), red (5 $cm^3 \cdot min^{-1}$), azure (30 $cm^3 \cdot min^{-1}$), and violet (100 $cm^3 \cdot mil^{-1}$).

To gain an understanding of these properties, the morphological change of K_2CO_3

was examined via SEM before and after CO_2 occlusion for various reaction times. The exemplary images for 5, 30, and 100 $cm^3 \cdot min^{-1}$ CO_2 atmospheres are shown in Figures 3-11, 3-12, and 3-13, respectively.

As seen in Figure 3-11a, K_2CO_3 particles, which were formed by the decomposition of $KHCO_3$ under a N_2 atmosphere, had a macroporous surface. For the CO_2 flow rate of 5 $cm^3 \cdot min^{-1}$ (Figure 3-11b), which is milder for the bicarbonate formation than the 100 $cm^3 \cdot min^{-1}$ flow rate (panels a and d of Figure 3-8), the diameter of the macropores on the surface slightly decreased after the initial 5 min. After 20 min, the pores on the surface nearly disappeared (Figure 3-11c), corresponding to products consisting of major $K_4H_2(CO_3)_3 \cdot 1.5H_2O$ and minor $KHCO_3$ (Figure 3-9c). Large granules of $KHCO_3$ developed on the external surface (Figure 3-11d) along with bicarbonate formation of $K_4H_2(CO_3)_3 \cdot 1.5H_2O$ reacting with CO_2 and H_2O for 20–120 min (Figures 3-9d and 3-7). During this transformation period, CO_2 occlusion reached a plateau in approximately 40 min (Figure 3-6), with no second peak developing in the DTG and DTA curves (Figure 3-8).

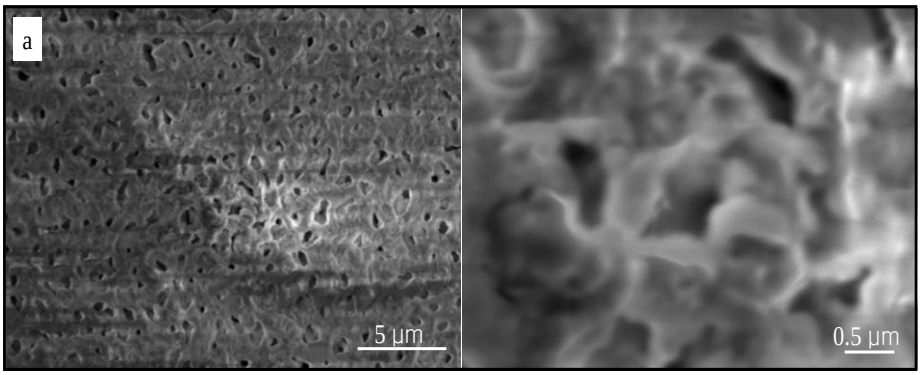

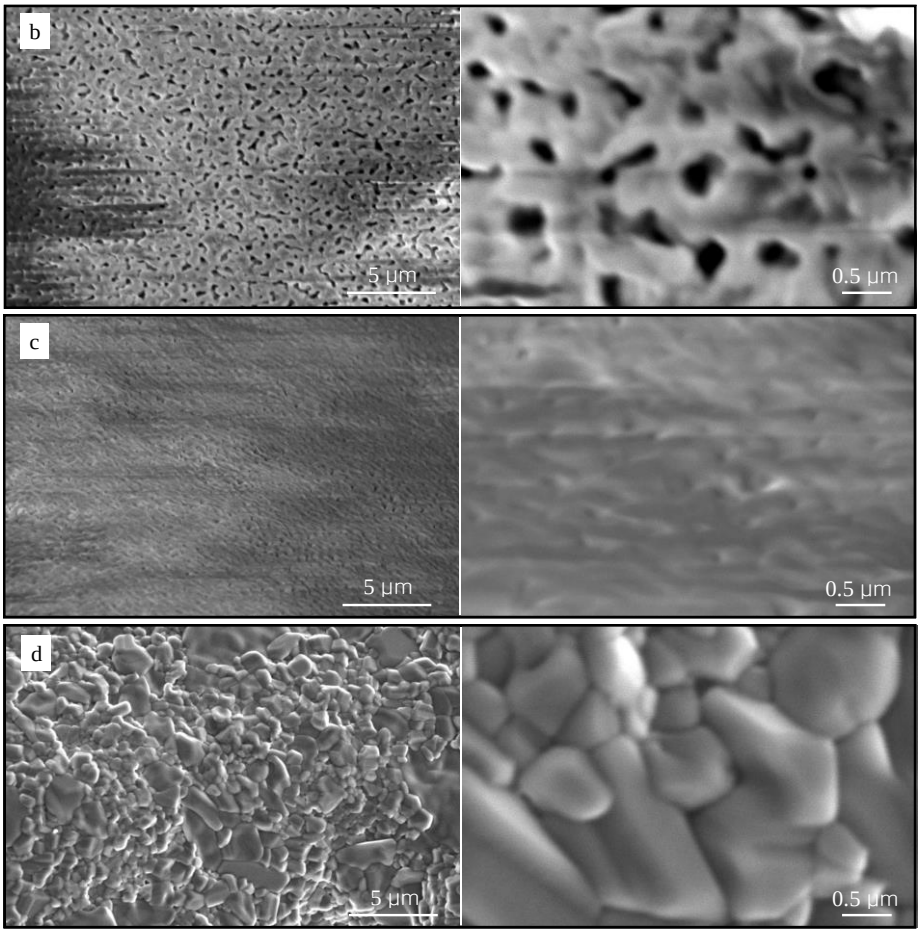

Figure 3-11: SEM images of K_2CO_3 before and after CO_2 occlusion at a CO_2 flow rate of 5 $cm^3 \cdot min^{-1}$ (a–d) (a: 0 min, b: 5 min, c: 20 min, and d: 120 min).

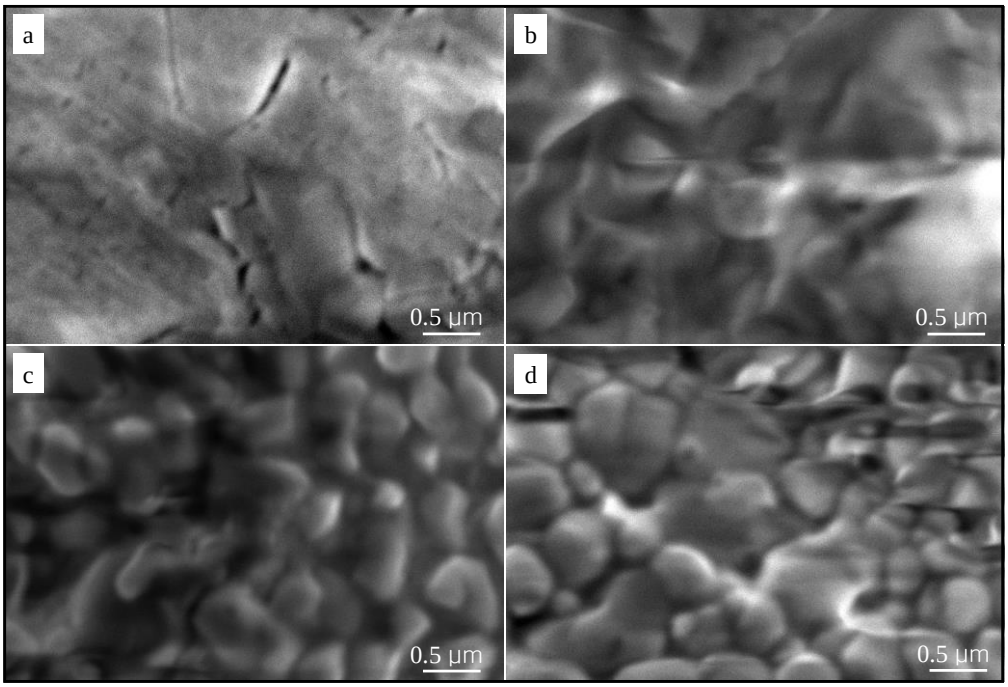

Figure 3-12: SEM images after CO_2 occlusion by K_2CO_3 at a CO_2 flow rate of 30 $cm^3 \cdot min^{-1}$ (a–d) (a: 5min, b: 20 min, c: 40 min, d: 120 min).

At a CO_2 flow rate of 30 $cm^3 \cdot min^{-1}$, as shown in Figure 3-12, the macropores on the surface significantly decreased after the initial 5 min and nearly disappeared to form the wrinkled surface after 20 min. The initial granule formation proceeded on the surface between 20 and 40 min. Finally, smaller granules developed on the surface after 120 min, compared to that for 5 $cm^3 \cdot min^{-1}$. These observations illustrated the development process of granules on the surface.

At a CO_2 flow rate of 100 $cm^3 \cdot min^{-1}$, as shown in Figure 3-13, the wrinkled surface was formed during the initial 5 min. This led to restricted formation of $K_2CO_3 \cdot 1.5H_2O$ and $K_4H_2(CO_3)_3 \cdot 1.5H_2O$. The initial granule growth on the surface, which was accompanied by disappearance of the pores at 20 min (Figure 3-13f), caused the slow transformation process of $K_2CO_3 \cdot 1.5H_2O$ and $K_4H_2(CO_3)_3 \cdot 1.5H_2O$ between 5 and 20 min (panels b and c of Figure 3-9). During this transformation period, the surface resistance continued to be enhanced because of the wrinkled surface formation covering

the initial product particles. As a result, we observed that the $K_2CO_3 \cdot 1.5H_2O$ phase remained at 100 $cm^3 \cdot min^{-1}$ and the formation of $KHCO_3$ from $K_4H_2(CO_3)_3 \cdot 1.5H_2O$ was limited already at 40 min (Figure 3-9d). Consequently, there was a faster decline in the temperature, DTA, and DTG curves between 20 and 40 min, as seen in Figure 3, indicating that the CO_2 occlusion rate at this CO_2 flow rate was slower than that for other CO_2 flow rates (with the exception of 1 $cm^3 \cdot min^{-1}$). The wrinkled surface must be broken to develop larger granules along with bicarbonate formation of $K_4H_2(CO_3)_3 \cdot 1.5H_2O$ between 40 and 60 min so that the CO_2 sorption rate and temperature can decrease according to the DTG and DTA curves in Figure 3-8. Considering the morphology and XRD patterns at 120 min for a CO_2 flow rate of 100 $cm^3 \cdot min^{-1}$, we can see that the smaller granules on the external surface developed with the bicarbonate formation of $K_4H_2(CO_3)_3 \cdot 1.5H_2O$ from 60 to 120 min, as seen in Figures 4e and 2. Because smaller granules promote the chemisorption and gas diffusion processes [28, 29], the acceleration of reaction (3-8) between 60 and 80 min (final stage) was found to cause the observed sharp peaks in the DTA and DTG curves in Figure 3-8.

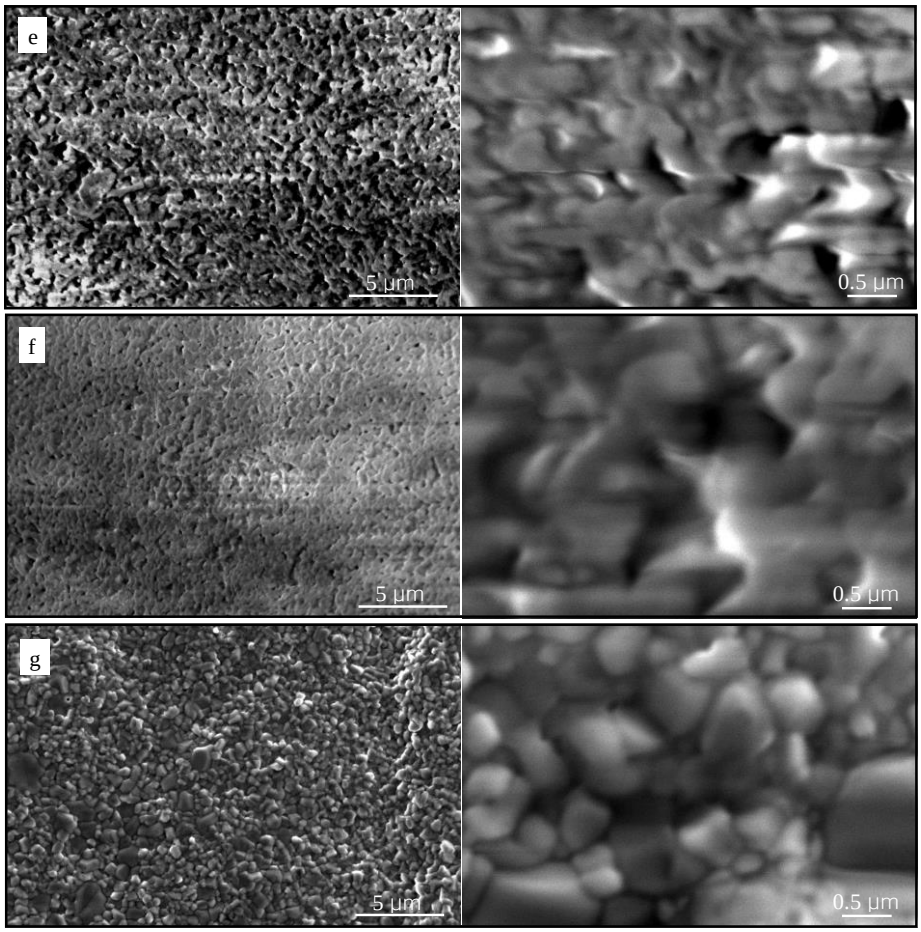

Figure 3-13: SEM images of K_2CO_3 after CO_2 occlusion at a CO_2 flow rate of 100 $cm^3 \cdot min^{-1}$ (e–g) (e: 5 min, f: 20 min, and g: 120 min).

To determine why the second peak appears for high CO_2 flow rates (20–100 $cm^3 \cdot min^{-1}$) during the final stage in Figure 3-8, we compared the morphology at 120 min for a CO_2 flow rate of 100 $cm^3 \cdot min^{-1}$ to that for a CO_2 flow rate of 30 $cm^3 \cdot min^{-1}$. From this, it was found that smaller granules of $KHCO_3$ developed on the surface at 120 min for the CO_2 flow rates of 30 and 100 $cm^3 \cdot min^{-1}$ with the bicarbonate formation of $K_4H_2(CO_3)_3 \cdot 1.5H_2O$. Furthermore, the CO_2 occlusion rate and accompanying temperature showed a transient and sharp increase during the final stage. In contrast, the morphology in the initial stage of CO_2 occlusion played a curial role in the overall reaction rate, which can account for the decline in temperature variation and the

intensity of the peaks in the DTA and DTG curves, as shown in panels d–f of Figure 3-8, upon increasing the CO_2 flow rate, with the exception of 1 $cm^3 \cdot min^{-1}$.

The analysis of variations in XRD patterns with reaction time of the bicarbonate formation process of K_2CO_3 under various CO_2 concentrations, illustrates that the reaction of K_2CO_3 with CO_2 and H_2O proceeds via three reactions. The results of changes in exothermic properties, temperature, and CO_2 occlusion rate show that the CO_2 occlusion process of K_2CO_3 also goes through three stages. The first product is $K_2CO_3 \cdot 1.5H_2O$, which can be converted to $K_4H_2(CO_3)_3 \cdot 1.5H_2O$ in the initial stage of CO_2 occlusion. The formation of $KHCO_3$ from $K_4H_2(CO_3)_3 \cdot 1.5H_2O$ proceeds slowly during the final stage, although there is a second increase in the CO_2 occlusion rate and temperature under high CO_2 flow rates (20–100 $cm^3 \cdot min^{-1}$). The analysis of morphology variation with reaction time demonstrates that the CO_2 occlusion of K_2CO_3 is inhibited at high CO_2 concentrations and the formation of $KHCO_3$ from $K_4H_2(CO_3)_3 \cdot 1.5H_2O$ is favorable for high amounts of CO_2 occlusion with increasing the CO_2 concentration. Particle morphology is found to play a crucial role in the kinetic behavior of CO_2 sorptivity of K_2CO_3. TG–DTA and XRD analysis show the dependence of CO_2 sorptivity of K_2CO_3 upon the CO_2 concentration under various CO_2 atmospheres in the presence of saturated water vapor.

3.3.3 CO_2 capture of K_2CO_3 under various H_2O concentrations

As mentioned above in CO_2 capture of K_2CO_3 under different CO_2 concentrations, the bicarbonate formation of K_2CO_3 proceeds via three stages. The formation and transformation of $K_2CO_3 \cdot 1.5H_2O$ and $K_4H_2(CO_3)_3 \cdot 1.5H_2O$ at the initial stage profoundly influence on the overall CO_2 occlusion rate of K_2CO_3 along with morphology variation. To identify the special effect of H_2O concentration on CO_2 capture of K_2CO_3 for a higher CO_2 concentration under moist conditions, thus, the study on CO_2 capture of K_2CO_3 under different humidity is essential. The CO_2 occlusion of K_2CO_3 under different H_2O concentrations with the CO_2 flow rate of 30 $cm^3 \cdot min^{-1}$ and

XRD patterns of the products after the CO_2 occlusion were exhibited. Figure 3-14 visually showed that the CO_2 sorption amount almost had no increase while the occlusion rate significantly increased with the humidity increasing. This result indicates that the higher H_2O concentrations accelerate to CO_2 capture of K_2CO_3.

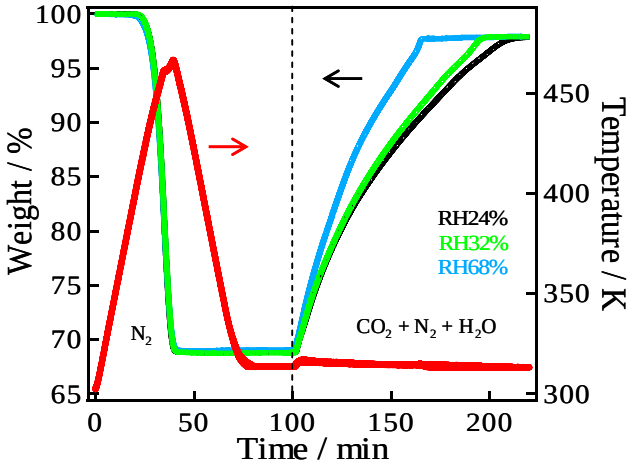

Figure 3-14: TG curves for the decomposition of $KHCO_3$ and CO_2 occlusion of K_2CO_3 under various H_2O concentrations at 313 K.

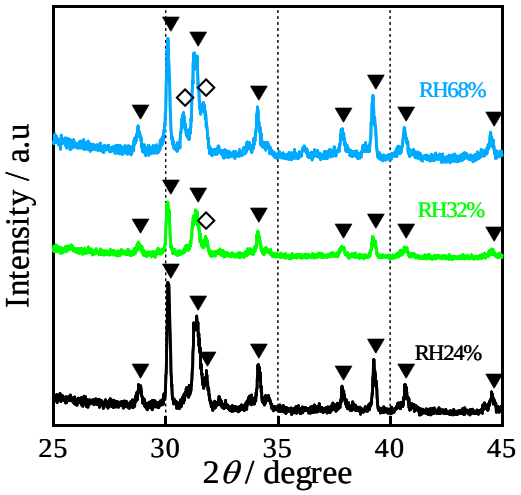

Figure 3-15: XRD patterns after CO_2 occlusion for various H_2O concentrations. ▼: $KHCO_3$, ◇: $K_4H_2(CO_3)_3 \cdot 1.5H_2O$.

XRD patterns after CO_2 occlusion of K_2CO_3 under different H_2O concentrations

showed that major $KHCO_3$ existed in the phases of peaks of K_2CO_3 after CO_2 occlusion under different humidity, as can be seen in Figure 3-15. With the H_2O concentration increasing, the peak intensity of $K_4H_2(CO_3)_3 \cdot 1.5H_2O$ increased. This result illustrated that the bicarbonate formation of $K_4H_2(CO_3)_3 \cdot 1.5H_2O$ was inhibited under the higher H_2O concentration.

The kinetic properties of CO_2 occlusion of K_2CO_3 can be tracked by monitoring the temperature under different humidity as the bicarbonate formation of K_2CO_3 leads to a temperature change of the exothermic reactions. Figure 3-16 showed that both DTA and DTG curves showed a striking similarity, exhibiting a series of peaks at the initial stage and final stage corresponding to exothermic reactions at the initial and final stages of CO_2 occlusion of K_2CO_3.

Similarly, there was a rise in temperature at the initial stage of the reaction with the H_2O concentration increasing from RH24% to RH68%. After the initial temperature rise, the temperature decreased moderately in all curves (middle stage). A second obvious increase at final stage was observed for the higher H_2O concentration (RH68%) when the CO_2 occlusion was close to equilibrium. These results demonstrated that the most thermal energy during the CO_2 occlusion process was obtained from the reactions at the initial stage. The peak (final stage) had an analogue peak in the DTA and DTG curves. Particularly, the CO_2 occlusion rate for the higher H_2O concentration, as shown in DTG curves, had a sharp rise at the final stage. It implied that the higher H_2O concentration was favorable to the initial and final stages of CO_2 occlusion process. Furthermore, these results displayed that both the initial stage and the overall reaction proceed to readily reach the CO_2 occlusion equilibrium with the H_2O concentration increasing. Also these results indicated that the overall reaction rate under different H_2O concentration depended upon the CO_2 occlusion rate at the initial and final stages. Especially, there was the slower CO_2 occlusion rate at the final stage according to the analyses of CO_2 occlusion of K_2CO_3 under different CO_2 concentrations. Thus, it indicated that the rate-controlling step was derived from one of the reactions at the final

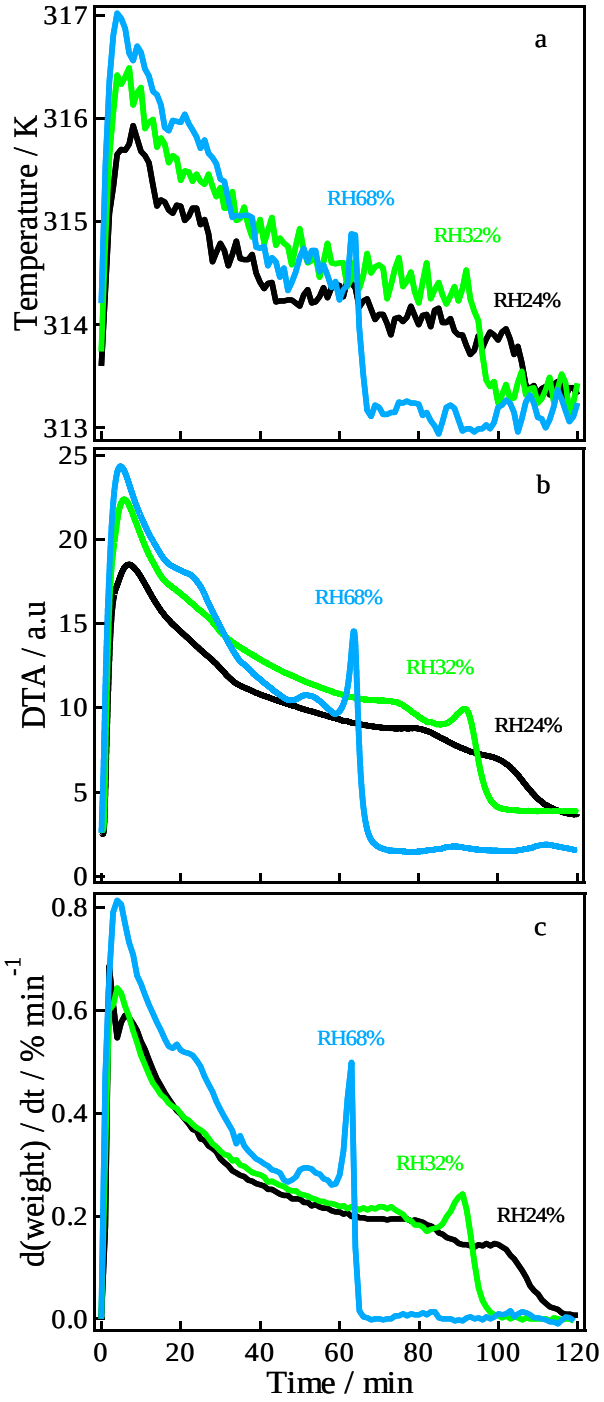

Figure 3-16: Temperature changes (a), DTA (b) and DTG (c) curves for various H_2O concentrations at a CO_2 flow rate of 30 $cm^3 \cdot min^{-1}$.

stage. Above these results and the rate-controlling step for different H_2O concentrations

can be understood together with analyses of the reactions at the initial and final stages on the basis of the crystalline structural change, which were discussed below.

The measurement of XRD patterns after CO_2 occluded by K_2CO_3 with the reaction time in the condition of different H_2O concentration with the CO_2 flow rate of 30 $cm^3 \cdot min^{-1}$ was examined to find the rate-limiting step of the bicarbonate formation of K_2CO_3. Numerous studies concerning the effect of H_2O concentration on CO_2 occlusion of K_2CO_3 have been reported. Park et al. reported that the CO_2 occlusion capacity increased with the H_2O flow rate from 0.009 to 0.077 $cm^3 \cdot min^{-1}$ [12]. Zhao et al. reported that CO_2 sorptivity of pure K_2CO_3 was considerably improved with the H_2O concentration from 0% to 21%, especially between 3% and 15%, with 15% CO_2 at 338 K at 0.1 MPa [25]. Particularly, it was claimed that the hydration reaction of K_2CO_3 was considered as the rate-controlling step for the CO_2 occlusion process so that the overall reaction rate and CO_2 uptake increased with the H_2O concentration increasing [23, 25]. However, our results indicated that there was a different possibility for the rate-controlling step. Besides, detailed information on the transformation of crystalline structure at the initial stage has not been revealed thus far.

The results of XRD patterns with the reaction time under different H_2O concentration can be seen in Figure 3-17. With the reactions occurring over 5 min (Figure 3-17a), the XRD patterns showed the presence of $K_2CO_3 \cdot 1.5H_2O$ and $K_4H_2(CO_3)_3 \cdot 1.5H_2O$ for the H_2O concentration between RH32% and RH68%. Also the peak intensity of $K_2CO_3 \cdot 1.5H_2O$ and $K_4H_2(CO_3)_3 \cdot 1.5H_2O$ in the XRD pattern significantly increased with the H_2O concentration increasing from 32% to 68%. This result indicated that the higher H_2O concentration contributed to the occurrence of the reactions (3-6) and (3-7). Thus, a maximum in the temperature is a result of the released heat from two reactions at initial stage, although we could not claim the heat mostly released from either reaction (3-6) or reaction (3-7).

As these two reactions were proceeding over 20 min for the H_2O concentration between RH32% and RH68%, the peak intensity of $K_2CO_3 \cdot 1.5H_2O$ in the XRD pattern

significantly decreased while the dominant peaks were derived from the $K_4H_2(CO_3)_3 \cdot 1.5H_2O$ phase. As a result, the $K_2CO_3 \cdot 1.5H_2O$ phase was mostly converted into the $K_4H_2(CO_3)_3 \cdot 1.5H_2O$ phase via the reaction (3-7). During this transformation period between 5 and 20 min corresponding to the observed decline at middle stage of DTA and DTG curves in Figure 3-16, it was concluded that $K_2CO_3 \cdot 1.5H_2O$ transformed from K_2CO_3 via the reaction (3-6) provided the main heat for CO_2 occlusion process. On the other hand, for the H_2O concentration of RH68%, the peaks of $KHCO_3$ phase transformed from the $K_4H_2(CO_3)_3 \cdot 1.5H_2O$ increased slightly through the reaction (3-8). In the case, there was still an obvious descending in the DTA and DTG curves between 5 min and 20 min. According to these changes, it can be confirmed that the reaction (3-6) is a highly exothermic initiation reaction rather than reaction (3-7) for CO_2 occlusion of K_2CO_3.

When the reactions were proceeding over 40 min, for the H_2O concentration of 32%, the major $K_4H_2(CO_3)_3 \cdot 1.5H_2O$ phase existed in XRD pattern while the dominant peaks were originating from the $KHCO_3$ phase and $K_4H_2(CO_3)_3 \cdot 1.5H_2O$ phase for the H_2O concentration of 68%. In addition, it was observed that the $K_2CO_3 \cdot 1.5H_2O$ phase still remained and no information on the $KHCO_3$ phase appeared for H_2O concentration of 32%. During the transformation period between 20 and 40 min, the CO_2 occlusion process proceeded through the reaction (3-7) for low H_2O concentration and reaction (3-8) for high H_2O concentration, respectively, as the intensity of DTA and DTG curves continually descended. Consequently, it was concluded that the exothermic property of the reaction (3-6) was much stronger than that of the reactions (3-7) and (3-8). Also the slower CO_2 occlusion via the reaction (3-8) indicated that the reaction (3-8) was the rate-controlling step.

With the reactions terminated at 120 min, the peak intensity of $K_4H_2(CO_3)_3 \cdot 1.5H_2O$ phase in XRD pattern increased with the H_2O concentration increasing. Compared with the XRD patterns between 40 and 120 min (Figures 3-17 and 3-15), the bicarbonate formation of $K_4H_2(CO_3)_3 \cdot 1.5H_2O$ mainly occurred during this transformation process

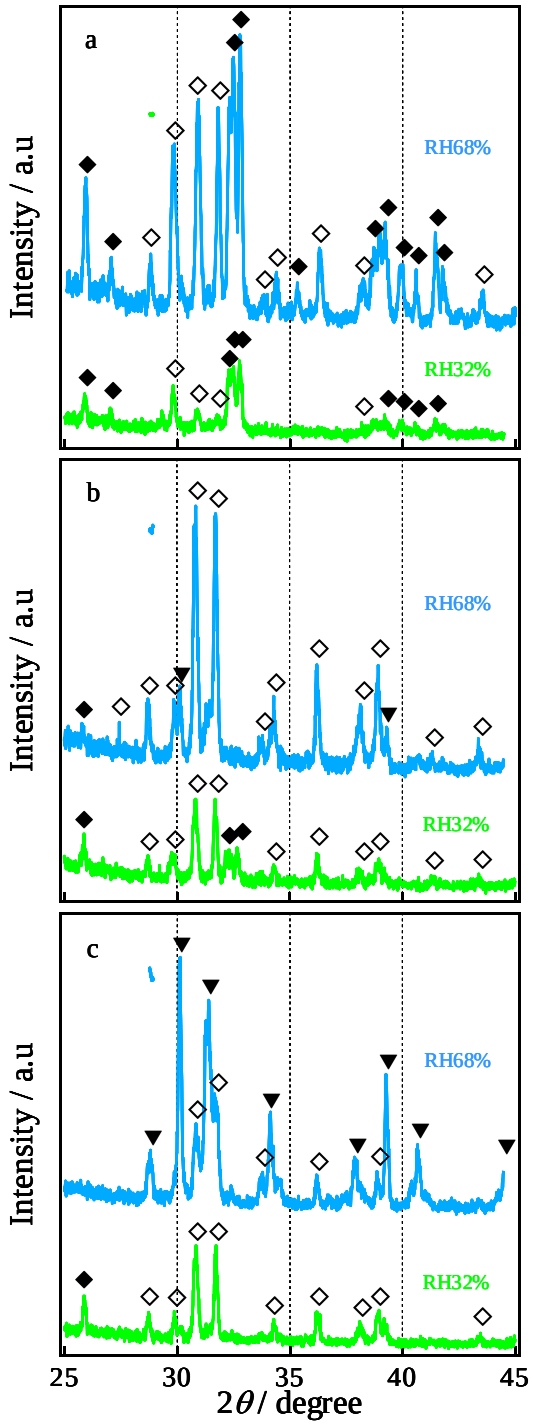

Figure 3-17: XRD patterns after CO_2 occlusion of K_2CO_3 for various H_2O concentrations over reaction times: (a) 5 min, (b) 20 min, and (c) 40 min. ▼: $KHCO_3$; ◇: $K_4H_2(CO_3)_3 \cdot 1.5H_2O$; ◆: $K_2CO_3 \cdot 1.5H_2O$.

corresponding to the uprise in the second peak intensity in temperature, DTA and DTG curves in Figure 3-16. This result is in accordance with the stronger temperature dependence on the reaction (3-5) rather than the reaction (3-4) in the section 3.3.1.

According to the crystalline structural changes over reaction time under different H_2O concentrations, we find that the reaction (3-8) is effectively clarified as the rate-limiting step with highly exothermic for CO_2 occlusion of K_2CO_3.

The morphology change of K_2CO_3 after the CO_2 occlusion for different reaction times was also examined with SEM. The SEM images for RH32% and RH68% H_2O concentration are shown in Figures 3-18 and 3-12, respectively.

There was a slight difference with the formation process for the granules on the surface via three stages for the H_2O concentrations between RH32% and RH68%. For the H_2O concentration of RH32%, the macropores on the surface significantly decreased at the initial 5 min and then remained after 20 min. The initial formation of large-sized granules proceeded on the surface between 20 and 40 min. Finally, small-sized granules developed on the surface after 120 min. Comparing the morphology at 120 min for the H_2O concentration of RH68% with that for the H_2O concentration of RH32%, it was found that the wrinkled surface was formed at 20 min and smaller-sized granules developed on the surface between 40 and 120 min for the H_2O concentration of RH68%. As mentioned in the section 3.3.2, the morphology variation from the wrinkled surface with the porous surface disappearing to smaller-sized granules on the surface lead to the rate changes of the reaction (3-8). These variations caused the observed reduction and then the rise in temperature variation and the intensity of peaks of DTA and DTG curves in Figure 3-16 between 20 and 120 min. Thus, the morphology at the middle and final stages of CO_2 occlusion played an important role in the reaction (3-8) rate of CO_2 occlusion. With the reaction (3-8) advancing, the residual $K_4H_2(CO_3)_3 \cdot 1.5H_2O$ still existed in XRD pattern (Figure 3-15) because the formed $KHCO_3$ granules on the surface increased the surface resistance. In contrary, there was not significantly variation of the morphology on the surface within 5 min. Consequently, the CO_2

occlusion rate at the initial stage depended upon reactions (3-6) and (3-7). These results of the initial and final stages for a higher H_2O concentration were promising for the CO_2 occlusion of K_2CO_3 at low temperature. Ultimately, higher H_2O concentration can provide significant the overall CO_2 occlusion rate at low temperatures.

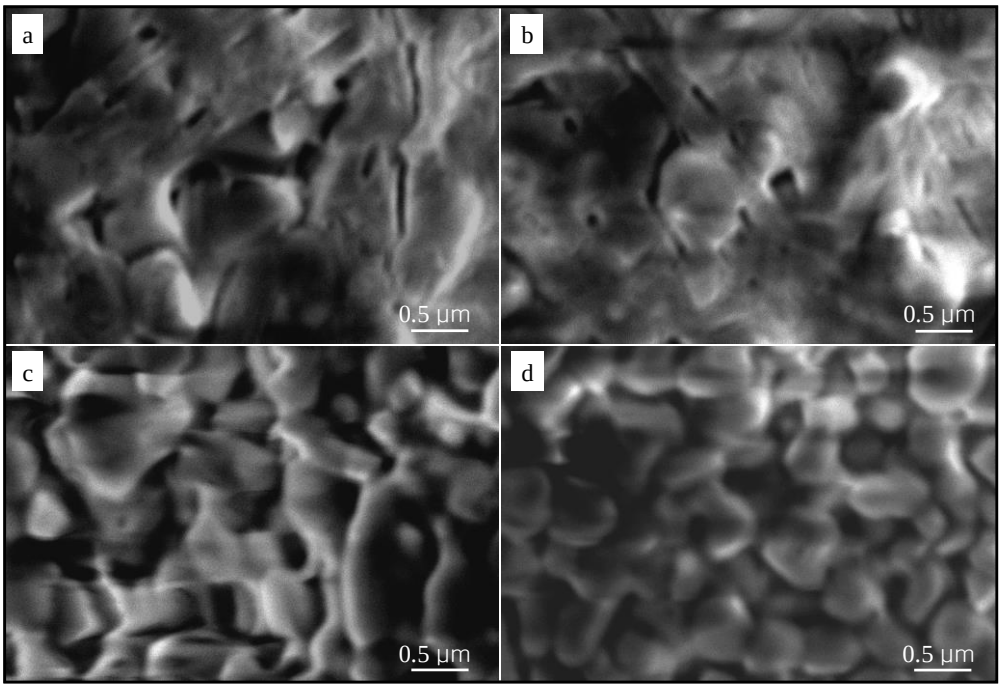

Figure 3-18: SEM images after CO_2 occlusion for the H_2O concentration of RH32% at a CO_2 flow rate of 30 $cm^3 \cdot min^{-1}$ at 313 K (a–d) (a: 5min, b: 20 min, c: 40 min, d: 120 min).

3.3.4 CO_2 capture of $K_4H_2(CO_3)_3 \cdot 1.5H_2O$ under different H_2O or CO_2 concentrations

CO_2 occlusion of $K_4H_2(CO_3)_3 \cdot 1.5H_2O$ displayed the slower bicarbonate formation process for higher CO_2 or lower H_2O concentration, as shown in the section 3.3.2 and 3.3.3, respectively. In order to better understand the exothermic property and bicarbonate formation behavior of $K_4H_2(CO_3)_3 \cdot 1.5H_2O$, the CO_2 occlusion was performed under pure CO_2 atmosphere and different CO_2 concentration containing saturated H_2O, respectively, can be seen in Figure 3-19. As both CO_2 concentration and

H_2O concentration increased, the CO_2 occlusion amount was significantly enhanced. The CO_2 occlusion amount increased to 2.86 mmol·g^{-1} for the CO_2 flow rate of 100 cm^3·min^{-1}, which is about 5% in excess of the theoretical amount of 2.73 mmol·g^{-1}. This result indicated that there was an error for the TG data caused by the multiple exchange process from N_2 to CO_2 + H_2O atmosphere. With the reaction (3-8) proceeding, the CO_2 occlusion rate for the CO_2 flow rate of 5 cm^3·min^{-1} reached the equilibrium at 20 min while that did at 40 min for the CO_2 flow rate of 100 cm^3·min^{-1}.

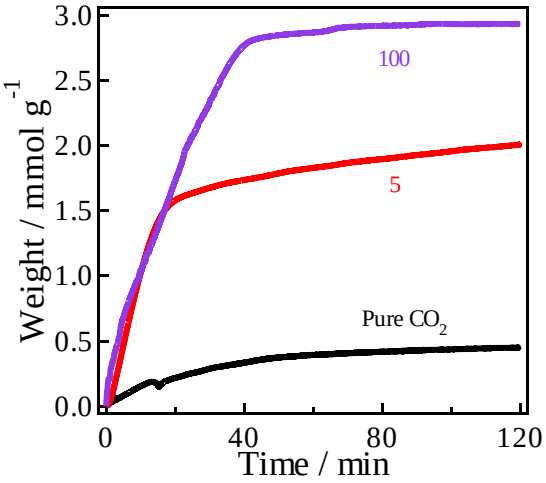

Figure 3-19: TG curves for CO_2 occlusion of $K_4H_2(CO_3)_3$·1.5H_2O at the pure CO_2 atmosphere, and the CO_2 flow rates of 5 cm^3·min^{-1} and 100 cm^3·min^{-1} at 313 K.

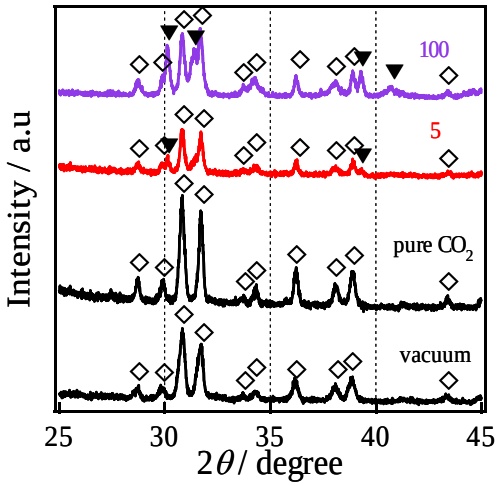

Figure 3-20: XRD patterns of $K_4H_2(CO_3)_3 \cdot 1.5H_2O$ before and after CO_2 occlusion. ▼: $KHCO_3$; ◇: $K_4H_2(CO_3)_3 \cdot 1.5H_2O$.

Figure 3-20 shows that the XRD patterns of $K_4H_2(CO_3)_3 \cdot 1.5H_2O$ before and after CO_2 occlusion were exhibited. Only $K_4H_2(CO_3)_3 \cdot 1.5H_2O$ phase exhibited in XRD patterns for the $K_4H_2(CO_3)_3 \cdot 1.5H_2O$ saved in vacuum oven and under pure CO_2 atmosphere. This result demonstrated that the error for the TG data caused by the multiple exchange process from N_2 to CO_2 atmosphere. For the CO_2 flow rate of 5 and 100 $cm^3 \cdot min^{-1}$, the XRD patterns contained the minor $KHCO_3$ phase and major $K_4H_2(CO_3)_3 \cdot 1.5H_2O$, indicating that the slower bicarbonate formation because of the surface resistance increasing based on the mentioned in the section 3.3.2 and 3.3.3.

Figure 3-21 shows the temperature changes, the DTA and DTG curves over reaction time. With the H_2O or CO_2 concentration increasing, there was an increase in the temperature and CO_2 occlusion rate along with the strong exothermic property. There was a maximum value of approximately 15 a.u. in the DTA curves in Figure 3-22b compared with that in Figure 3-8b in the section 3.3.2. It demonstrated that the exothermic property of reaction (3-8) was weaker than that of reaction (3-6). Figure 3-21c showed that the maximum in the reaction rate was 0.53 $\%\cdot min^{-1}$ at a CO_2 flow rate of 5 $cm^3 \cdot min^{-1}$, which was much lower than that at the initial stage in Figure 3-8c. This result can be confirmed that the bicarbonate formation of $K_4H_2(CO_3)_3 \cdot 1.5H_2O$ [reaction (3-8)] is the rate-controlling step for the CO_2 occlusion of K_2CO_3 under moist conditions in the presence of saturated water vapor. Furthermore, with increasing CO_2 concentration, the maximum value in the CO_2 occlusion rate decreased, as seen in Figure 3-21c, which was consistent with those at the final stage under various CO_2 and H_2O concentrations.

The morphology of $K_4H_2(CO_3)_3 \cdot 1.5H_2O$ before and after CO_2 occlusion for the CO_2 flow rates of 5 and 100 $cm^3 \cdot min^{-1}$, respectively, were observed in Figure 3-22. Figure 3-22a illustrated that macropore almost disappeared to form the compact plane on the

surface according to the preparation method of $K_4H_2(CO_3)_3 \cdot 1.5H_2O$ at higher temperature. The panels b and c of Figure 3-22 showed that the $KHCO_3$ granules developed on the surface.

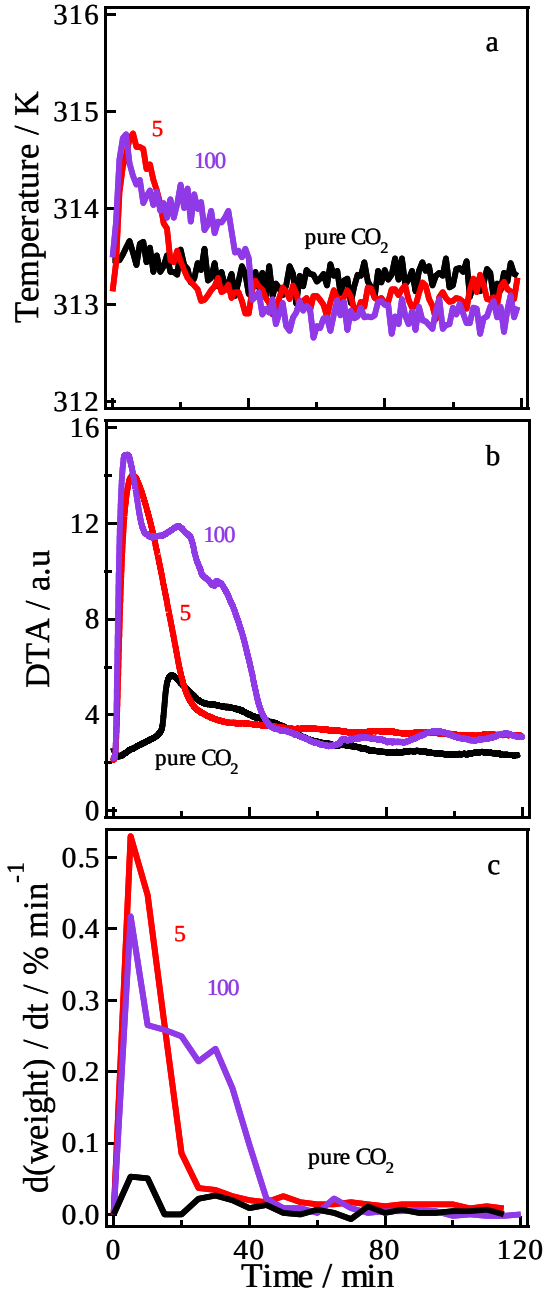

Figure 3-21: Temperature changes (a), DTA (b) and DTG (c) curves for different CO_2 or H_2O concentration.

Finally, based on the analyses of above XRD patterns and morphology, the reaction (3-8) as the rate-controlling step play an important role in the CO_2 occlusion of K_2CO_3. The granules developed on the surface and the surface resistance increased with the bicarbonate formation proceeding. It can be required to improve the morphology on the surface for the bicarbonate formation favorable the application for CO_2 occlusion of K_2CO_3.

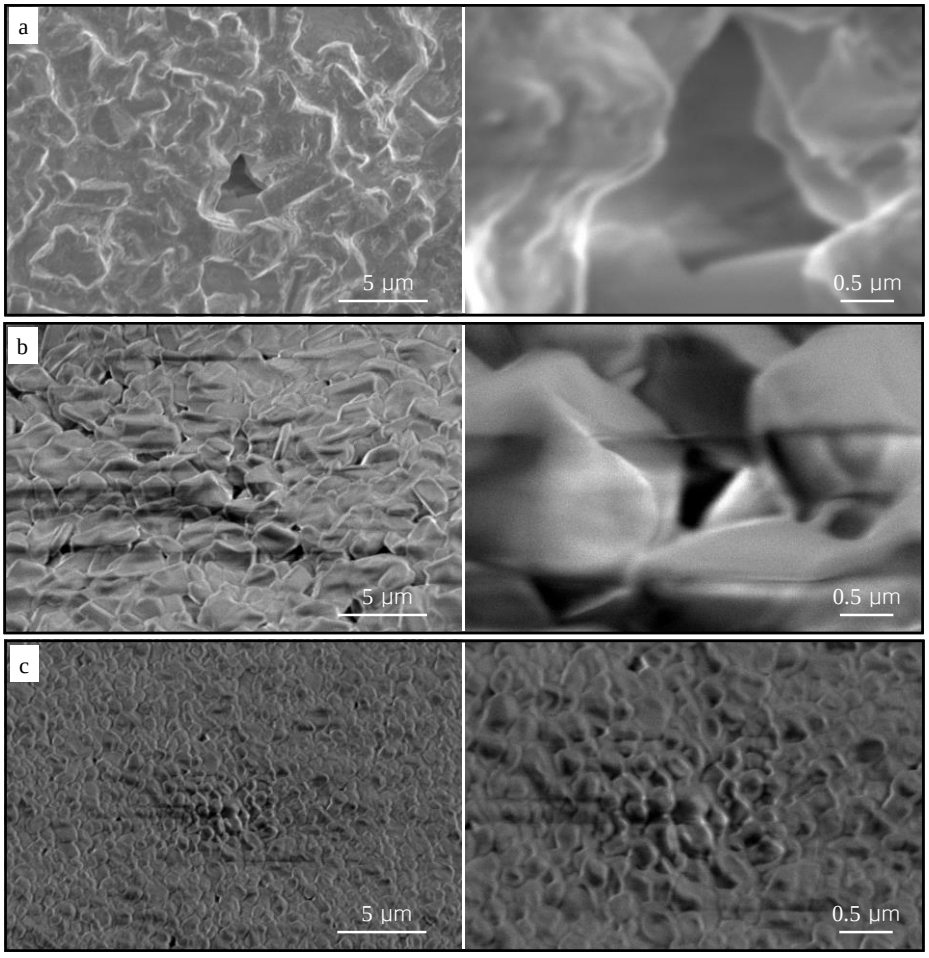

Figure 3-22: SEM images for $K_4H_2(CO_3)_3 \cdot 1.5H_2O$ before (a) and after CO_2 occlusion for the CO_2 flow rates of 5 $cm^3 \cdot min^{-1}$ (b) and 100 $cm^3 \cdot min^{-1}$ (c).

3.4 Conclusion

TG-DTA and XRD analyses showed the dependence of CO_2 sorptivity of K_2CO_3 on

the temperature, CO_2 concentration, and H_2O concentration. Lower temperature is favorable to the bicarbonate formation. The analysis of changes in XRD patterns over reaction time of the bicarbonate formation process of K_2CO_3 under different CO_2 and H_2O concentrations, illustrates that the reaction of K_2CO_3 with CO_2 and H_2O proceeds via three reactions. Also the results of changes in exothermic properties, temperature, and CO_2 occlusion rate show that the CO_2 occlusion process of K_2CO_3 goes through three stages. The formation of $K_2CO_3{\cdot}1.5H_2O$ from K_2CO_3 provides the most heat. $K_2CO_3{\cdot}1.5H_2O$ as the first product can be converted into $K_4H_2(CO_3)_3{\cdot}1.5H_2O$ in the initial stage of CO_2 occlusion. The formation of $KHCO_3$ from $K_4H_2(CO_3)_3{\cdot}1.5H_2O$ is considered as the rate-controlling step, which slowly proceeds at the final stage, although there is a second rise in CO_2 occlusion rate and temperature under higher CO_2 flow rates (20–100 $cm^3{\cdot}min^{-1}$). The analysis of morphology variation over reaction time shows that the CO_2 occlusion of K_2CO_3 is inhibited at a higher CO_2 or lower H_2O concentration, and the formation of $KHCO_3$ from $K_4H_2(CO_3)_3{\cdot}1.5H_2O$ was favorable to high CO_2 occlusion amount with increasing CO_2 or H_2O concentration. Particle morphology is found to play a crucial role in kinetic behavior of CO_2 sorptivity of K_2CO_3 and $K_4H_2(CO_3)_3{\cdot}1.5H_2O$. Ultimately, K_2CO_3 can be used for CO_2 capture under low temperature, and 5–10% CO_2 concentration in the presence of saturated water vapor.

References

[1] M. Aresta. Carbon dioxide recovery and utilization, *Kluwer Academic Pub.*, Boston, **2003**, 53.

[2] B. Metz, O. Davidson, H. de Coninck, M. Loos, L. Meyer. IPCC 2005: Special Report on Carbon Dioxide Capture and Storage, *Cambridge University Press*, New York, **2005**.

[3] T. F. Wall. *Proc. Combust. Inst.*, **2007**, 31, 31−47.

[4] W. C. Yang, J. Hoffman. *Ind. Eng. Chem. Res.*, **2009**, 48, 341−351.

[5] K. J. Fricker, A. H. A. Park. *Eng.Sci.* **2013**, 100, 332−341.

[6] M. G. Plaza, S. García, F. Rubiera, J. J. Pis, C. Pevida. *J.Chem. Eng.*, **2010**, 163, 41−47.

[7] S. Cavenati, C. A. Grande, A. E. Rodrigues. *J. Chem. Eng. Data*, **2004**, 49, 1095−1101.

[8] V. Presser, J. McDonough, S.H. Yeon, Y. Gogotsi. *Energy Environ. Sci.*, **2011**, 4, 3059−3066.

[9] C. Zhao, X. Chen, C. Zhao. *Chemosphere*, **2009**, 75, 1401−1404.

[10] Y. C. Park, S. H. Jo, C. K. Ryu, C. K. Yi. *Energy Proc.*, **2011**, 4, 1508−1512.

[11] Y. C. Park, S. H. Jo, D. H. Lee, C. K. Yi, C. K. Ryu, K. S. Kim, C. H. You, Y. S. Park. *Energy Proc.*, **2013**, 37, 122−126.

[12] S. W. Park, D. H. Sung, B. S. Choi, J. W. Lee, H. Kumazawa. *J. Ind. Eng. Chem.*, **2006**, 12, 522−530.

[13] Y. Seo, S. H. Jo, C. K. Ryu, C. K. Yi. *J. Environ. Eng.*, **2009**, 135, 473−477.

[14] C. Zhao, X. Chen, C. Zhao. *Energ. Fuel*, **2009**, 23, 4683−4687.

[15] C. Zhao, X. Chen, C. Zhao. *Int. J. Greenhouse Gas Control*, **2010**, 4, 655−658.

[16] C. Zhao, X. Chen, C. Zhao. *Ind. Eng. Chem. Res.*, **2010**, 49, 12212−12216.

[17] C. Zhao, X. Chen, C. Zhao. *Energ. Fuel*, **2012**, 26, 1401−1405.

[18] H. Hayashi, J. Taniuchi, N. Furuyashiki, S. Sugiyama, S. Hirano, N. Shigemoto, T.

Nonaka. *Ind. Eng. Chem. Res.*, **1998**, 37, 185−191.

[19] N. Shigemoto, T. Yanagihara, S. Sugiyama, H. Hayashi. *Energ. Fuels*, **2006**, 20, 721−726.

[20] Y. W. Seo, S. H. Jo, H. J. Ryu, D. H. Bae, C. K. Ryu, C. K. Yi. *Korean J. Chem. Eng.*, **2007**, 24, 457−460.

[21] S. C. Lee, H. J. Chae, B. Y. Choi, S. Y. Jung, C. Y. Ryu, J. J. Park, J. I. Baek, C. K. Ryu, J. C. Kim. *Korean J. Chem. Eng*., **2011**, 28, 480−486.

[22] H. Chioyama, H. Luo, T.Ohba, H. Kanoh. *Adsorption Sci. and Technol.*, **2015**, 33, 243−250.

[23] C. Zhao, Y. Guo, C. Li, S. lu. *Chem. Eng. J.*, **2014**, 254, 524−530.

[24] C. Zhao, X. Chen, C. Zhao, Y. Liu. *Energ. Fuel*, **2009**, 23, 1766−1769.

[25] C. Zhao, X. Chen, C. Zhao. *Ind. Eng. Chem. Res.*, **2012**, 51, 14361−14366.

[26] S. C. Lee, B. Y. Choi, C. K. Ryu, Y. S. Ahn, T. J. Lee, J. C. Kim. *Korean J. Chem. Eng.*, **2006**, 23, 374−379.

[27] S. C. Lee, J. C. Kim. *Catal. Surv. Asia*., **2007**, 11, 171−185.

[28] M. J. Venegas, E. Fregoso-Israel, R. Escamilla, H. Pfeiffer. *Ind. Eng. Chem. Res.*, **2007**, 46, 2407−2412.

[29] F. García-Labiano, A. Abad, L .F. de Diego, P. Gayán, J. Adánez. *Chem. Eng. Technol.*, **2002**, 57, 2381−2393.

Chapter 4: Fundamentals in CO_2 Sorptivity of Na_2CO_3

4.1 Introduction

Alkali metal carbonate sorbents have been paid attention for CO_2 capture application over the past several years [1–4]. With high occlusion capacity and low cost, Na_2CO_3 as a CO_2 sorbent under moist conditions at 0.1 MPa and above 313 K have been studied extensively [5–10]. The humidity plays a curial role in CO_2 occlusion amount and the overall reaction rate. With increasing the H_2O concentration, the CO_2 occlusion amount and rate significantly increased [7–10]. Furthermore, it was reported that the hydrate of Na_2CO_3 could be formed slowly through reaction (4-1) in the presence of excess of water vapor at below 333 K [11]:

$$Na_2CO_3(s) + H_2O(g) \leftrightarrows Na_2CO_3 \cdot H_2O\ (s) \quad (4\text{-}1)$$

The temperature also plays an important role in CO_2 capture. Most previous studies regarding CO_2 capture of Na_2CO_3-based sorbents were performed using the thermogravimetric analyzer, several fixed-bed, and fluidized-bed, where the flue gas was simulated with 5–10% CO_2 with 10–20% H_2O at relatively high temperatures (323–353 K) under atmospheric pressure [11–24]. In numerous studies on the CO_2 sorption of Na_2CO_3 under moist conditions, it was found that Na_2CO_3 decomposed from $NaHCO_3$ had a better performance on CO_2 capture, whereas Na_2CO_3 and $Na_2CO_3 \cdot H_2O$ hardly reacted with CO_2 [11–14]. When the flue gas conditions were 8% CO_2 with 16% H_2O in helium, Na_2CO_3 decomposed from $NaHCO_3$ could be converted to $Na_5H_3(CO_3)_4$ through reaction (4-3) at 343 K and higher, whereas $NaHCO_3$ was formed via reaction (4-2) at below 343 K [11]. Dong et al. also reported that the formation of $Na_5H_3(CO_3)_4$

could be transformed from Na_2CO_3 supported on Al_2O_3 through reaction (4-3) under moist flue gas (15% CO_2 with 15% H_2O) in Nitrogen at around 333 K [23, 24]. The relevant reactions are [11]:

$$Na_2CO_3(s) + CO_2(g) + H_2O(g) \leftrightarrows 2NaHCO_3(s) \quad (4\text{-}2)$$

$$5Na_2CO_3(s) + 3CO_2(g) + 3H_2O(g) \leftrightarrows 2Na_5H_3(CO_3)_4(s) \quad (4\text{-}3)$$

where the forward, exothermic reactions (4-2) and (4-3) are the bicarbonate and Wegscheider's salt formation of Na_2CO_3, respectively, corresponding to theoretical CO_2 capture amount of Na_2CO_3 is 9.43 and 5.66 mmol·g^{-1}, while the reverse, endothermic reactions are the decomposition of $NaHCO_3$ and $Na_5H_3(CO_3)_4$, respectively. These results indicate that lower temperature favors to bicarbonate formation.

However, no detailed information on crystal structure changes with reaction time has been revealed so far. The morphologies of Na_2CO_3 particles also change as the reactions proceeds, because the growth of crystals depends on the reaction conditions. This information is also important for understanding the kinetic behavior of Na_2CO_3 particles. But details of the morphology variation with reaction time has not been reported, thus, the CO_2 capture mechanisms under different CO_2 and H_2O conditions are not understood clearly.

In this chapter, CO_2 sorptivity of Na_2CO_3 at different temperatures, under various CO_2 and H_2O concentrations were examined by the thermogravimetric-differential thermal analysis (TG-DTA) and accompanying structural changes over reaction time were exhibited by X-ray diffraction (XRD) method under vacuum. Morphology variations with reaction time were observed by using a scanning electron microscopy (SEM). On the basis of crystal structure and kinetics analysis of bicarbonate formation of Na_2CO_3, the dependence of CO_2 capture of Na_2CO_3 on CO_2 concentration and humidity is explained in details.

4.2 Experimentals

4.2.1 Sample preparation

Analytical reagent grade $NaHCO_3$ (99 % chemical purity, Wako Chemical Co., Ltd.) was used throughout the decomposition experiments of $NaHCO_3$ and bicarbonate formation measurements of Na_2CO_3. The decomposition of $NaHCO_3$ was processed with the thermogravimetric-differential thermal analysis (TG-DTA; Shimadzu, DTG-60AH). $NaHCO_3$ (30−50 mg) was heated at 5 $K \cdot min^{-1}$ from 298 to 473 K to form Na_2CO_3 in an atmosphere of pure N_2 at 100 $cm^3 \cdot min^{-1}$ and held at these conditions for 5 min to complete the decomposition. Subsequently, the temperature was lowed to 303 K at -5 $K \cdot min^{-1}$ and kept for 30 min under a N_2 atmosphere.

4.2.2 Bicarbonate formation measurements

The obtained samples were processed with the TG-DTA apparatus using a gas composition of CO_2 and H_2O (v/v of 98.2:1.8) at a flow rate of 100 $cm^3 \cdot min^{-1}$ at temperatures between 303 and 363 K for 18 h.

The measurements of the Na_2CO_3 bicarbonate formation with varying reaction duration were performed with the TG-DTA apparatus with various compositions of CO_2 and N_2 containing saturated water vapor at 303 K for 300 min. CO_2 and N_2 were obtained from high-purity gas cylinders with mass flow controllers used to control the flow rate. H_2O vapor was produced by flowing N_2 and CO_2 into distilled water in a bubbler for more than 5 h to reach saturation, where N_2 gas was used as balance gas.

On the other hand, under different humidity conditions, the measurements of the Na_2CO_3 bicarbonate formation with varying reaction duration were also performed with the TG-DTA apparatus. H_2O vapor was supplied by flowing N_2 into distilled water inside a bubbler and another N_2 used as dry gas inside a bubbler to adjust the H_2O partial pressure.

For above bicarbonate formation measurements, the mixed gas of CO_2, H_2O and N_2 was introduced into a moisture detector with a thermometer and hygrometer at 313 K. The relative humidity of the mixed gas was measured with the hygrometer. The total gas

flow rate was maintained at 100 $cm^3 \cdot min^{-1}$ for all experiments.

4.2.3 Crystal structure and morphology measurements

The crystal structures of the products after CO_2 occlusion reactions with 10, 20, 40, and 300 min were measured by using an X-ray diffractometer (XRD; MAC Science, M03XHF) under vacuum to avoid occlusion of CO_2 or H_2O from the ambient atmosphere. The powder XRD patterns were obtained in the 2θ range of 25–45° using Cu Kα radiation (40 kV, 25 mA, and λ = 0.15406 nm) at room temperature. The morphology of Na_2CO_3 particles before and after CO_2 capture for the different reaction times were observed by using scanning electron microscopy (SEM; JEOL, JSM-6510A) after coating the samples (10 mA, 10 s) with metallic osmium.

4.3 Results and discussion

4.3.1 CO_2 capture of Na_2CO_3 at different temperatures

The decomposition of $NaHCO_3$ was processed with TG-DTA under a N_2 atmosphere via the reverse reaction of (4-2) to form Na_2CO_3, CO_2, and H_2O at 473 K, as shown in Figure 4-1. The weight for the decomposition of $NaHCO_3$ from 0 to 90 min gradually decreased to 63.0% (±0.2%), which is in very good agreement with the theoretical value of 63.1% according to the reverse reaction of (4-2). This confirms that the decomposition reaction proceeds completely. After the decomposition, a mixture of CO_2 and H_2O was supplied to Na_2CO_3 at different temperatures. As shown in Figure 4-1, the sample weight and bicarbonate formation rate increased slowly with increasing temperature from 303 K to 363 K. It indicated that Na_2CO_3 should be a promising sorbent under moist conditions at low temperature. When the temperature was at 303 K, there was the rapid increase in sample weight between 3 h and the CO_2 occlusion amount was 8.32 $mmol \cdot g^{-1}$, which is 88.2% of the theoretical amount (i.e. 9.43 $mol \cdot g^{-1}$). Compared with the result at 303 K, both CO_2 occlusion rate and amount slightly decreased at 323 K. As the temperature increased from 323 K to 343 K, the CO_2

occlusion amount only increased to 6.30 mmol·g^{-1} along with the initial formation slowly proceeding. With the temperature increased to 363 K, the CO_2 occlusion amount was zero mmol·g^{-1}. Above CO_2 occlusion at different temperatures reached a plateau after 5 h. In general, bicarbonate formation requires a minimum activation energy for the occurrence of chemical reaction, it can be attributed to the change increased more rapidly at higher temperatures. However, the change increased slowly at higher temperatures indicated that CO_2 occlusion of Na_2CO_3 did not simply depend upon the temperature.

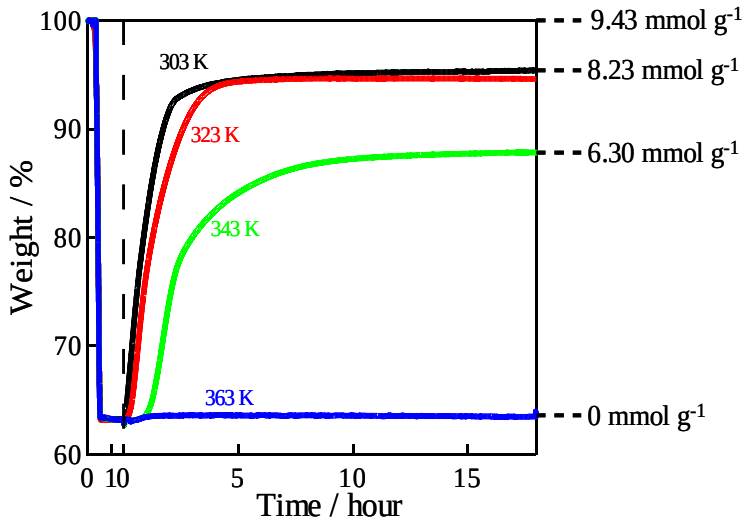

Figure 4-1: Weight change by the decomposition of $NaHCO_3$ (<40 min) at 473 K and the bicarbonate formation of Na_2CO_3 with CO_2 and H_2O (>90 min) at different temperatures.

Because the temperature dependence of the CO_2 occlusion amount and rate can not be understood clearly, the crystal structure after CO_2 occlusion at different temperatures was examined to obtain XRD patterns, as seen in Figure 4-2. The XRD patterns showed the peaks consisting of two phases, i.e., $NaHCO_3$ and $Na_5H_3(CO_3)_4$, at the temperatures from 303 K to 343 K. Furthermore, the peak intensity of $Na_5H_3(CO_3)_4$ phase increased with increasing temperature. This indicated that reaction (4-3) occurred favorably for

relatively high temperatures, whereas reaction (4-2) proceeded at rather lower temperatures. Only pure Na_2CO_3 phase existed in the XRD patterns of CO_2 occluded sample at 363 K. These results were in good agreement with the decline in CO_2 occlusion amount with increasing temperature.

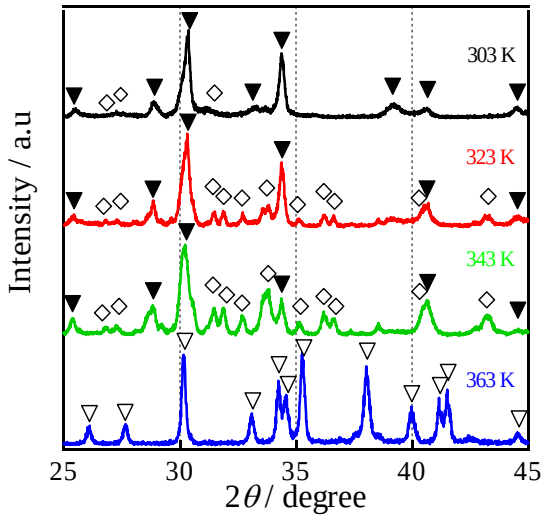

Figure 4-2: XRD patterns of CO_2 occluded samples at different temperatures.
▼: $NaHCO_3$, ◇: $Na_5H_3(CO_3)_4$, ▽: Na_2CO_3

Figure 4-3 showed that DTA curves (a) and DTG curves (b) were obtained at the temperatures of 303–363 K. The DTA curves indicated exothermic reactions for CO_2 occlusion of Na_2CO_3 under moist conditions while both DTA and DTG curves showed a striking similarity. With increasing temperature, the peak intensity diminished in the DTG and DTA curves, which corresponded to exothermic reactions of the formation of $NaHCO_3$ and $Na_5H_3(CO_3)_4$ through Na_2CO_3 reacting with CO_2 and H_2O. It can be confirmed that CO_2 occlusion rate of reaction (4-3) is slower than reaction (4-2) on account of much more $Na_5H_3(CO_3)_4$ formation at higher temperatures. Consequently, it can be also identified that releasing the heat of reaction (4-3) is lower than that of reaction (4-2) based on the observed peak in the DTA curves.

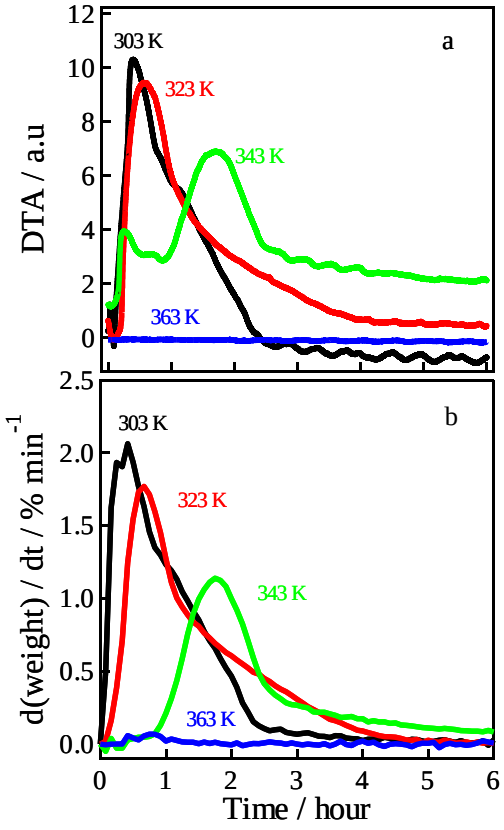

Figure 4-3: DTA (a) and DTG (b) curves over reaction time at different temperatures.

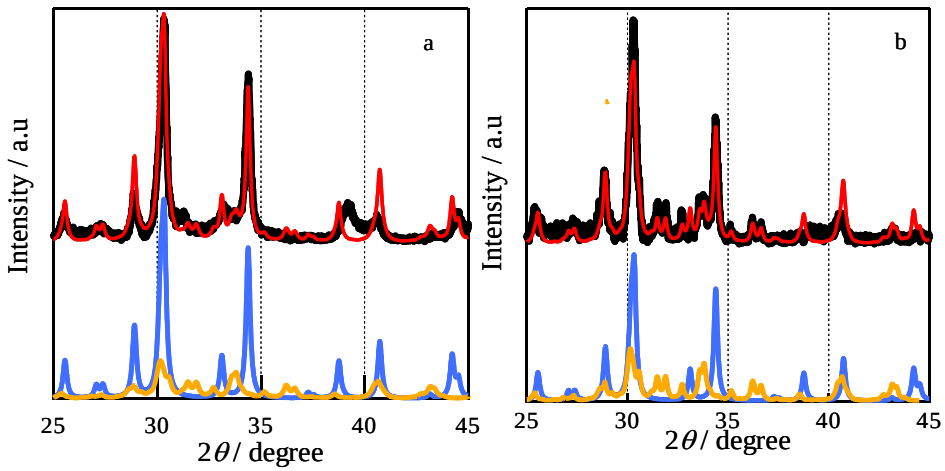

Figure 4-4: Peak fitting of XRD peaks of pure phases to the experimental results obtained at 303 K (a) and 323 K (b). Black: experimental pattern; Red: fitted pattern obtained by using a pattern of pure $NaHCO_3$ (blue) and pure $Na_5H_3(CO_3)_4$ (orange).

As mentioned in the section 3.3.1 in Chapter 3, according to well-fitted peak patterns of these pure phases regarding to the relative ratios of peak intensities of pure $NaHCO_3$ and $Na_5H_3(CO_3)_4$ phases, the experimental patterns of pure $NaHCO_3$ and $Na_5H_3(CO_3)_4$ phases obtained at 303 K and 323 K were shown in Figure 4-4a and b, respectively.

Furthermore, the ratio between the peak area of $NaHCO_3$ and the total peak area of $NaHCO_3$ and $Na_5H_3(CO_3)_4$, $I_{NaHCO_3}/\left(I_{NaHCO_3}+I_{Na_5H_3(CO_3)_4}\right)$, was calculated by the peak fitting for each peak of pure $NaHCO_3$ and $Na_5H_3(CO_3)_4$ phases at 303–343 K, as shown in Figure 4-5. It was found that the ratio of the $NaHCO_3$ phase decreased with increasing temperature. This result further demonstrates that low temperature contributes to bicarbonate formation of Na_2CO_3 occluded CO_2 and H_2O via highly exothermic reaction (4-2).

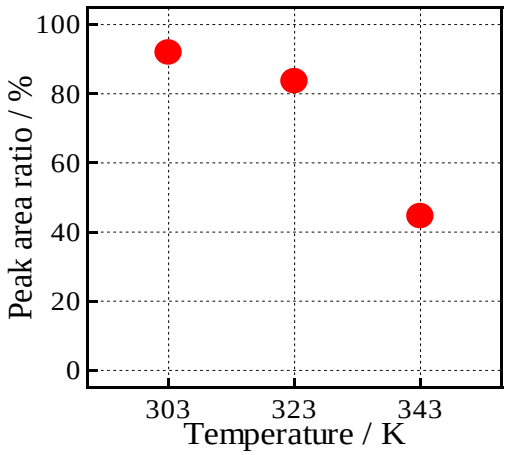

Figure 4-5: Temperature dependence of the peak area ratio of $NaHCO_3$ to the total peak area of $NaHCO_3$ and $Na_5H_3(CO_3)_4$.

The TG-DTA and X-ray powder diffraction analyses show that the CO_2 occlusion of Na_2CO_3 at different temperatures involves two exothermic reactions of the formation of $NaHCO_3$ and $Na_5H_3(CO_3)_4$ from Na_2CO_3. The highly exothermic reaction (4-2) proceeds more easily at low temperatures, whereas reaction (4-3) proceeds at higher temperatures. Moreover, releasing the heat of reaction (4-3) is lower than that of

reaction (4-2). Thus, Na_2CO_3 can be suitable for the CO_2 capture at low temperatures.

4.3.2 CO_2 capture of Na_2CO_3 under various CO_2 concentrations

The dependence of the sorptivity of Na_2CO_3 on CO_2 concentration was obtained with TG-DTA under various CO_2 flow rates, as shown for reaction time of 0–300 min in Figure 4-6.

In similar to the section 3.3.2 in Chapter 2, a sufficiently humid atmosphere (RH of 74% at 303 K) was also supplied to Na_2CO_3 with a mixed gas of CO_2 and N_2 in the presence of saturated water vapor. When the CO_2 flow rate was only 1 $cm^3 \cdot min^{-1}$, the occlusion amount was 2.84 $mmol \cdot g^{-1}$ at 300 min. As the CO_2 flow rate increased from 1 to 30 $cm^3 \cdot min^{-1}$, the CO_2 occlusion amount of Na_2CO_3 increased from 2.84 to 7.39 $mmol \cdot g^{-1}$ at 300 min, which is 74.2–92% of the theoretical amount of 9.43 $mmol \cdot g^{-1}$. Especially, at initial 50 min, the CO_2 occlusion amount already increased from 0.43 to 5.75 $mmol \cdot g^{-1}$, which is 64.8–85.6% of the theoretical amount. When the CO_2 flow rate increased from 30 to 100 $cm^3 \cdot min^{-1}$, the occlusion amount of Na_2CO_3 increased to 8.10 $mmol \cdot g^{-1}$ at 300 min, which is 94.8% of the theoretical amount of 9.43 $mmol \cdot g^{-1}$. These experimental results were consistent with higher CO_2 flow rates favorable for higher CO_2 occlusion amount according to reactions (4-2) and (4-3). Higher CO_2 occlusion amount could be achieved with increasing CO_2 flow rate from 30 to 100 $cm^3 \cdot min^{-1}$, however, the CO_2 occlusion rate was much slow, as can be seen in Figure 4-6b. When the CO_2 flow rate was 100 $cm^3 \cdot min^{-1}$, the CO_2 occlusion amount was only 4.91 $mmol \cdot g^{-1}$ at 50 min, which is 82.3% that is lower than 85.6% at 30 $cm^3 \cdot min^{-1}$. In contrast, when the CO_2 flow rate was 20 and 30 $cm^3 \cdot min^{-1}$, the CO_2 occlusion rate was much faster than other CO_2 flow rates.

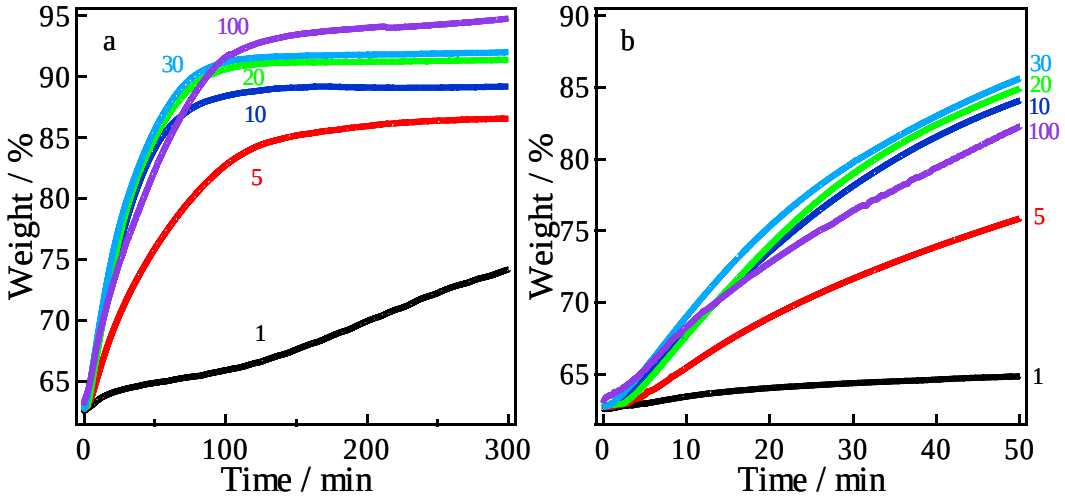

Figure 4-6: TG curves (a) for bicarbonate formation under various CO_2 flow rates ($cm^3 \cdot min^{-1}$), which are indicated with numbers, with N_2 and H_2O and magnified for 0–50 min (b).

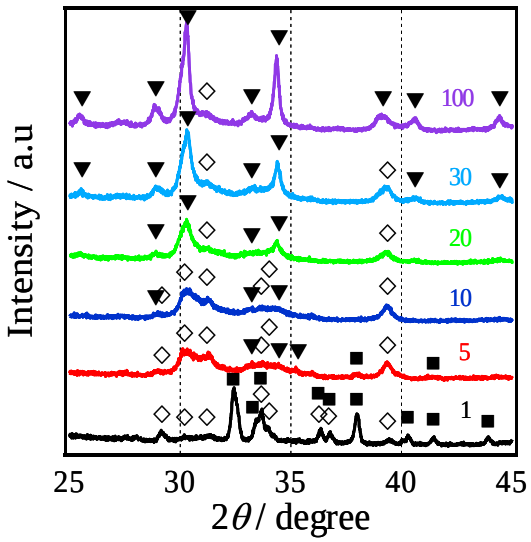

Figure 4-7: XRD patterns after CO_2 occlusion of Na_2CO_3 at various CO_2 flow rates ($cm^3 \cdot min^{-1}$), which are indicated with numbers.
▼: $NaHCO_3$, ◇: $Na_5H_3(CO_3)_4$, ■ : $Na_2CO_3 \cdot H_2O$

Figure 4-7 showed the XRD patterns after the CO_2 occlusion of Na_2CO_3 (300 min marked in Figure 4-6) at various CO_2 flow rates. When the CO_2 flow rate was only 1 and 5 $cm^3 \cdot min^{-1}$, the $Na_2CO_3 \cdot H_2O$ phase was present in the samples because of

unfavorably shift toward the forward reactions of (4-2) and (4-3) under lower CO_2 concentrations. With increasing the CO_2 concentration between 5–100 $cm^3 \cdot min^{-1}$, the peaks of the $Na_5H_3(CO_3)_4$ and $Na_2CO_3 \cdot H_2O$ phases appeared to decrease while that of the $NaHCO_3$ phase increased. This result in the XRD patterns was consistent with the TGA data.

The CO_2 occlusion of Na_2CO_3 at high CO_2 flow rates was limited during 50 min based on the TG results in Figure 4-6b. According to the section 4.3.1, there is the different exothermic along with the formation of $NaHCO_3$ and $Na_5H_3(CO_3)_4$, thus, the transformation process of Na_2CO_3 leads to a temperature change of the reaction system. Hence, investing the transformation process of Na_2CO_3 and the associated changes in temperature during the formation of $NaHCO_3$ and $Na_5H_3(CO_3)_4$ is important for a better understanding of the CO_2 sorptivity kinetics of Na_2CO_3.

Figure 4-8 shows the temperature variations curves (a), DTA curves (b), and derivative thermogravimetric (DTG) curves (c; obtained by differentiating the weight change in Figure 4-6 over time) for different CO_2 concentrations. The temperature variations, DTA, and DTG curves exhibited a series of peaks, as can be seen in Figure 4-8a–c.

The maximum rate of this initial stage increased at approximately 10 min with the CO_2 flow rate from 1 to 30 $cm^3 \cdot min^{-1}$, but decreased with higher CO_2 flow rate at this stage, where were consistent with the TG results in Figure 4-6a and b. After the initial increase in CO_2 occlusion rate, the reaction rate decreased in all curves until to the completed CO_2 occlusion (300 min). With initiating the different rate of CO_2 occlusion under various CO_2 concentrations, the exothermic signals, which were similar to the variations of CO_2 occlusion rate, were observed in Figure 4-8b and e. Also associated temperature changes displayed remarkable similarity to DTA and DTG curves, which were caused by the CO_2 occlusion reactions with highly exothermic, as shown in Figure 4-8a and b. These results indicate that the overall reaction depending strongly upon the initial stage under various CO_2 flow rates proceeds slowly, which can be understood

together with analysis of the reaction mechanism of the system, as discussed below.

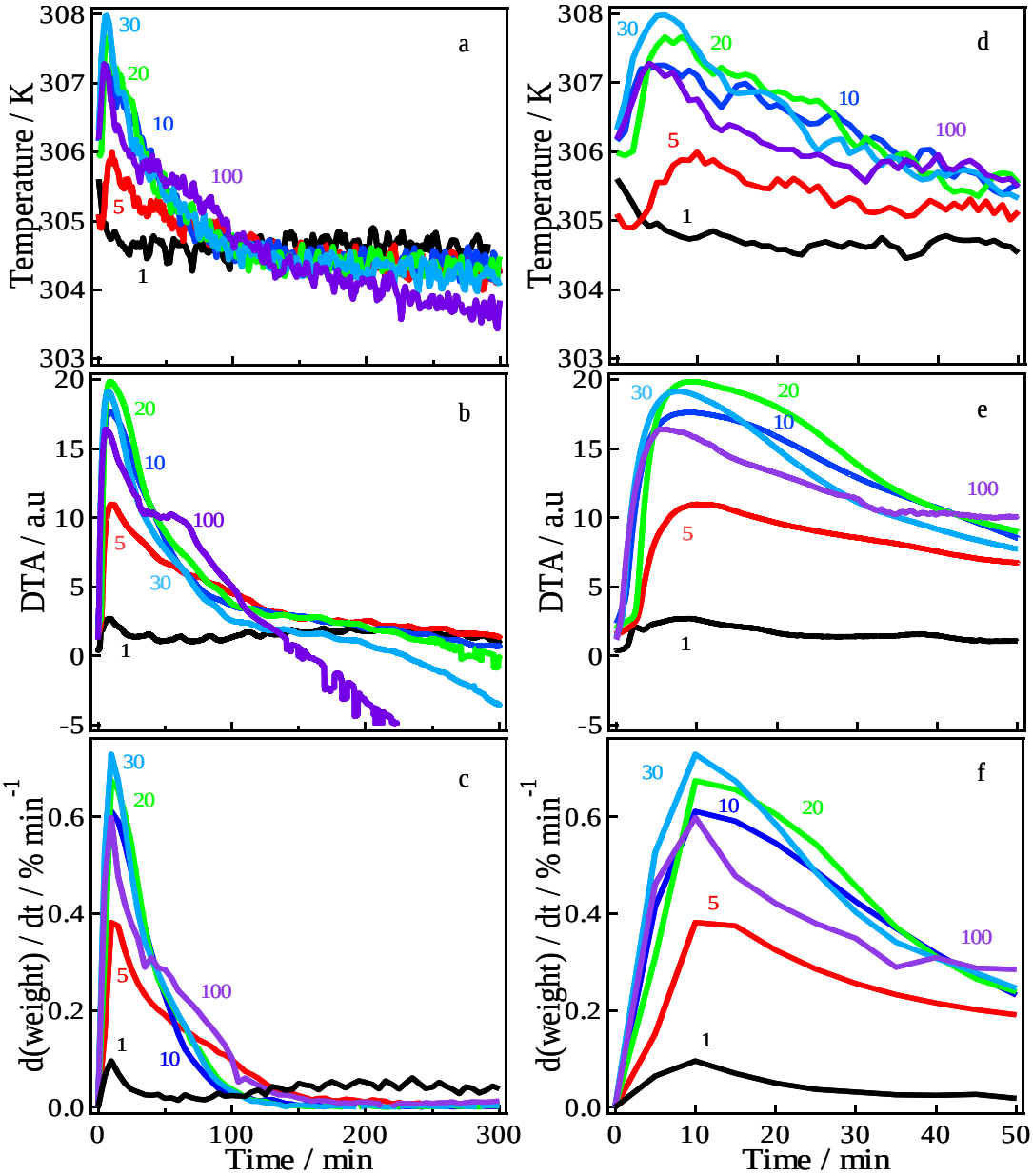

Figure 4-8: Temperature change (a), DTA (b), and DTG (c) curves at various CO_2 flow rates ($cm^3 \cdot min^{-1}$), which are indicated with numbers. These panels are magnified for reaction times of 0–50 min in d, e, and f, respectively.

The XRD patterns of CO_2–occluded samples of Na_2CO_3 in the presence of water vapor with various reaction times were examined, as shown in Figure 4-9.

When the reaction was proceeding to 10 min, major Na_2CO_3 and minor $Na_2CO_3 \cdot H_2O$ phases were present in XRD patterns for various CO_2 flow rates. Liang reported that $Na_2CO_3 \cdot H_2O$ was formed slowly when the temperature was lower than 333 K under excess of water vapor [11]. $Na_2CO_3 \cdot H_2O$ was also transformed under lower CO_2 concentration (1 and 5 $cm^3 \cdot min^{-1}$) at room temperature, as can be seen in Figure 4-7. During this transformation period, it can be claimed that the hydration of Na_2CO_3 occur via reaction (4-1) in the presence of saturated water vapor at room temperature. In addition, the XRD patterns showed the presence of the $Na_5H_3(CO_3)_4$ phase for the CO_2 flow rates of 10 $cm^3 \cdot min^{-1}$, whereas few $NaHCO_3$ phase were present in XRD patterns for high CO_2 concentrations (30 and 100 $cm^3 \cdot min^{-1}$). The formation of $Na_5H_3(CO_3)_4$ and $NaHCO_3$ phases could be transformed from either Na_2CO_3 or $Na_2CO_3 \cdot H_2O$. Thus, it can be concluded that the temperature changes are a result of the exothermic reactions at this stage.

With the reaction occurring over 20 min, Na_2CO_3 phase still remained in the XRD patterns for all CO_2 flow rates. For low CO_2 flow rate (10 $cm^3 \cdot min^{-1}$), the peak intensity of $Na_5H_3(CO_3)_4$ phase increased significantly with $Na_2CO_3 \cdot H_2O$ phase diminishing. This result indicated that $Na_5H_3(CO_3)_4$ was transformed from $Na_2CO_3 \cdot H_2O$ rather than Na_2CO_3. Conversely, for high CO_2 flow rates (30 and 100 $cm^3 \cdot min^{-1}$), the $NaHCO_3$ and $Na_5H_3(CO_3)_4$ phases increased slightly. Furthermore, the peaks of Na_2CO_3 phase in XRD patterns for 100 $cm^3 \cdot min^{-1}$ remained more than 10 and 30 $cm^3 \cdot min^{-1}$. These results indicated that the transformation process of Na_2CO_3 was inhibited between 10–20 min for high CO_2 flow rates. Thus, it can be identified that the inhibited transformation at high CO_2 flow rates caused the peak intensity sharply decreasing in the DTG and DTA curves between 10–20 min in Figure 4-8d–f.

With increasing the reaction time to 40 min, the peaks of the $NaHCO_3$ phases increased significantly while the peak intensity of Na_2CO_3 phase decreased for 30 and 100 $cm^3 \cdot min^{-1}$. During this transformation process, the peak intensity of $Na_5H_3(CO_3)_4$ nearly increased between 20 and 40 min, corresponding to $Na_2CO_3 \cdot H_2O$ phase barely

decreasing (Figure 4-9c). It can be deduced that the formation of $NaHCO_3$ was derived from Na_2CO_3. During the transformation process, it was found that there was a decline in the DTG and DTA curves in Figure 4-8d–f. Consequently, the temperature continued to decrease along with the formation of $NaHCO_3$. Compared to the XRD patterns for 30 and 100 $cm^3 \cdot min^{-1}$, the XRD patterns for 10 $cm^3 \cdot min^{-1}$ between 20–40 min nearly varied, which were assigned to the phases of Na_2CO_3, $Na_2CO_3 \cdot H_2O$, and $Na_5H_3(CO_3)_4$.

Considering the XRD patterns at 300 min for the CO_2 flow rates of 30 and 100 $cm^3 \cdot min^{-1}$, with the $Na_5H_3(CO_3)_4$ phase decreasing between 40 and 300 min (Figures 4-9c and 4-7), the XRD patterns showed that the peak intensity of $NaHCO_3$ phase increased slightly at 300 min. Thus, it can be confirmed that the $Na_5H_3(CO_3)_4$ is converted slowly to $NaHCO_3$. These results were consistent with the DTG and DTA curves.

On the basis of the discussed transformation process, the following reactions instead of reaction (4-3) could be summarized under various CO_2 flow rates in the presence of saturated water vapor, with the exception of reaction (4-2).

$$Na_2CO_3(s) + H_2O(g) \leftrightarrows Na_2CO_3 \cdot H_2O(s) \quad (4\text{-}4)$$

$$5Na_2CO_3 \cdot H_2O(s) + 3CO_2(g) \leftrightarrows 2Na_5H_3(CO_3)_4(s) + 2H_2O(g) \quad (4\text{-}5)$$

$$Na_5H_3(CO_3)_4(s) + CO_2(g) + H_2O(g) \leftrightarrows 5NaHCO_3(s) \quad (4\text{-}6)$$

We find that the transformation process, consisting of the formation of $Na_2CO_3 \cdot H_2O$ from Na_2CO_3, $Na_5H_3(CO_3)_4$ transformed from $Na_2CO_3 \cdot H_2O$ and Na_2CO_3, and the bicarbonate formation of $Na_5H_3(CO_3)_4$, should be the main pathway of CO_2 occlusion for low CO_2 concentrations (below 10 $cm^3 \cdot min^{-1}$) rather than that for high CO_2 concentrations (30 and 100 $cm^3 \cdot min^{-1}$). Conversely, for high CO_2 concentrations, bicarbonate formation was mostly derived from Na_2CO_3 directly through reaction (4-2), although the CO_2 capture was accompanying the formation of few $Na_5H_3(CO_3)_4$ and $Na_2CO_3 \cdot H_2O$. Thus, bicarbonate formation through reaction (4-2) accounts for higher

proportion of these two pathways with increasing the CO_2 concentration.

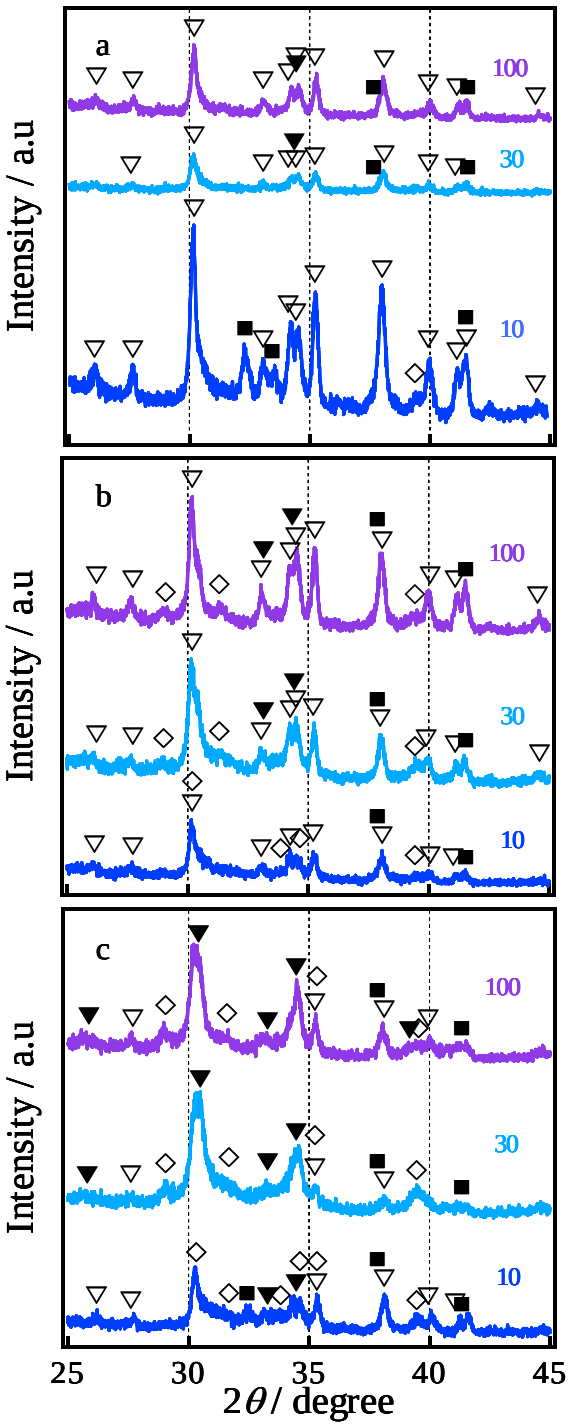

Figure 4-9: XRD patterns after CO_2 occlusion of Na_2CO_3 at various CO_2 flow rates ($cm^3 \cdot min^{-1}$), which are indicated with numbers, with reaction time: (a) 10 min, (b) 20 min, (c) 40 min. ▼: $NaHCO_3$, ◇: $Na_5H_3(CO_3)_4$, ■ : $Na_2CO_3 \cdot H_2O$, ▽: Na_2CO_3.

As mentioned in the section 4.3.1, reaction (4-2) has higher exothermic than reaction (4-3), however, Figure 4-8 displays the opposite results regarding the CO_2 occlusion rate and exothermic properties for 100 $cm^3 \cdot min^{-1}$. Hence, the initial exothermic properties and the CO_2 capture rate of Na_2CO_3 under various CO_2 flow rates cannot be obtained from XRD data alone based on the discussed transformation processes and kinetics of CO_2 sorptivity of Na_2CO_3 under various CO_2 flow rates and in the presence of saturated water vapor. To acquire a better understanding of these properties, the morphological change of Na_2CO_3 was examined via SEM before and after CO_2 occlusion for various reaction times. The SEM images for 10, 30 and 100 $cm^3 \cdot min^{-1}$ CO_2 atmospheres are shown in Figures 4-10, 4-11, and 4-12, respectively.

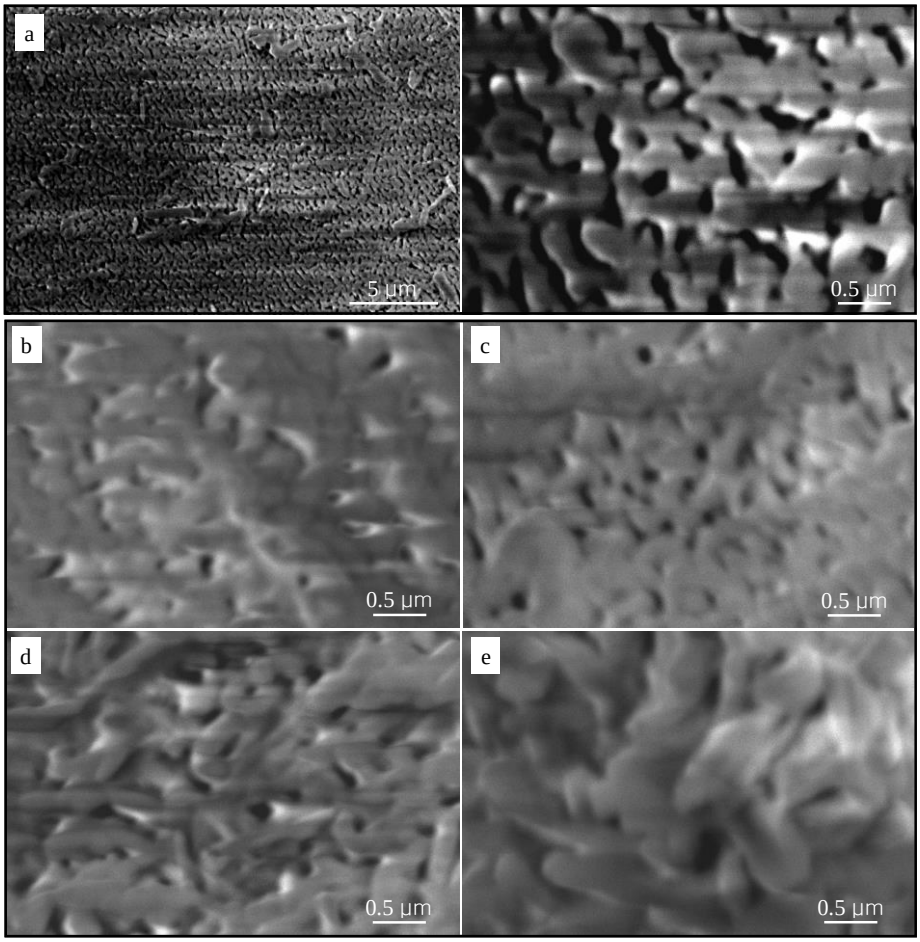

Figure 4-10: SEM images of Na_2CO_3 before and after CO_2 occlusion at a CO_2 flow rate of 10 $cm^3 \cdot min^{-1}$ (a–e) (a: 0 min, b: 10 min, c: 20 min, d: 40 min, and e: 300 min).

Na_2CO_3 particles, as shown in Figure 4-10a, which were formed by the decomposition of $NaHCO_3$ under a N_2 atmosphere, had a macroporous surface. For the CO_2 flow rate of 10 $cm^3 \cdot min^{-1}$, the diameter of the macropores on the surface slightly diminished after the initial 10 min (Figure 4-10b) with the formation of major $Na_2CO_3 \cdot H_2O$ and minor $Na_5H_3(CO_3)_4$, which the maximum in CO_2 occlusion rate was obtained. After 20 min, the pores on the surface developed (Figure 4-10c), corresponding to the transformation of $Na_2CO_3 \cdot H_2O$ to $Na_5H_3(CO_3)_4$. Large granules of dominant $Na_5H_3(CO_3)_4$ developed on the external surface (Figure 4-10d and e) along with $Na_2CO_3 \cdot H_2O$ reacting with CO_2 and H_2O for 40–300 min (Figures 4-9c and 4-7).

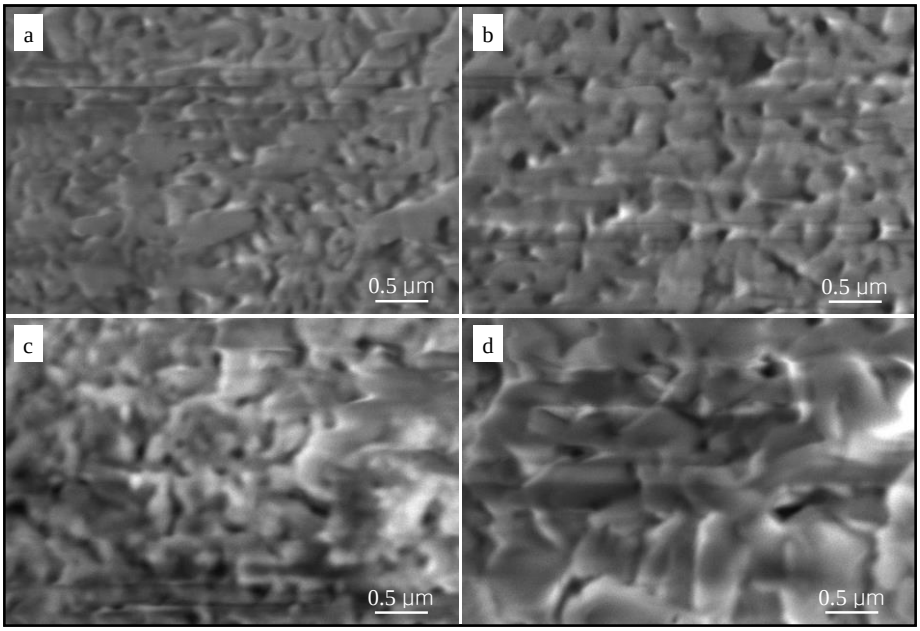

Figure 4-11: SEM images of Na_2CO_3 after CO_2 occlusion at a CO_2 flow rate of 30 $cm^3 \cdot min^{-1}$ (a–d) (a: 10 min, b: 20 min, c: 40 min, and d: 300 min).

For the CO_2 flow rate of 30 $cm^3 \cdot min^{-1}$, the diameter of the macropores on the surface significantly decreased and few mcropores remained on the surface after the initial 10 min (Figure 4-11a). Macropores on the surface were still present after 20 min. Initial formation of large granules proceeded on the external surface after 40 min (Figure 4-11c) along with the formation of major $NaHCO_3$ and minor $Na_5H_3(CO_3)_4$ between 20 and 40

min (Figures 4-9b and c). After 300 min, few macropores appeared on the surface after 300 min. This result demonstrates that the evolution of water vapor stem from reaction (4-5) leads to the macropores on the surface between 20–300 min. Furthermore, the formation of $NaHCO_3$ covering the Na_2CO_3 particles results in the surface resistance increasing to inhibit the CO_2 occlusion. Thus, we can observe that there is an obvious decline in the DTG and DTA curves (Figure 4-8e and f).

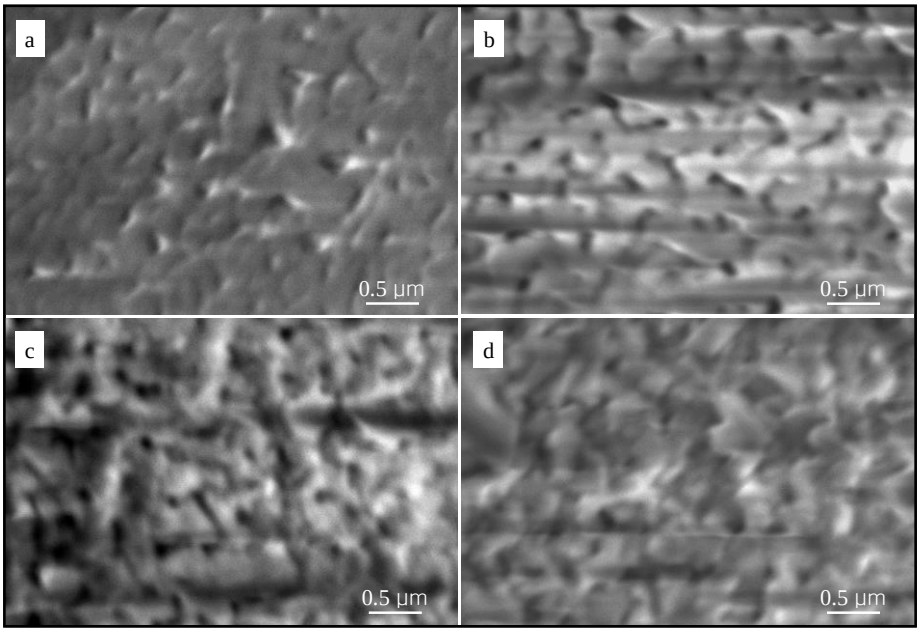

Figure 4-12: SEM images of Na_2CO_3 after CO_2 occlusion at a CO_2 flow rate of 100 $cm^3 \cdot min^{-1}$ (a–d) (a: 10 min, b: 20 min, c: 40 min, and d: 300 min).

For the CO_2 flow rate of 100 $cm^3 \cdot min^{-1}$, the diameter of the macropores on the surface nearly disappeared after the initial 10 min (Figure 4-12a) and then form the wrinkled surface after 20 min. This result leads to the restricted transformation of Na_2CO_3 for 100 $cm^3 \cdot min^{-1}$ (Figure 4-9a and b). Thus, it was observed that the peak intensity at the initial stage decreased in the DTG and DTA curves (Figure 4-8e and f). Initial formation of granules on the surface continued to increase the surface resistance after 40 min. Granules of $NaHCO_3$ developed on the external surface (Figure 4-12c and d) along with bicarbonate formation of Na_2CO_3 and $Na_2CO_3 \cdot H_2O$ reacting with CO_2

and H_2O between 40–300 min (Figures 4-9c and 4-7). In the case of lower proportion of bicarbonate formation transformed from $Na_5H_3(CO_3)_4$, it can be observed that macropores on the surface indeed disappear.

On the basis of the discussed the structure changes and morphological variation with reaction times under various CO_2 concentrations, it is found that the bicarbonate formation of Na_2CO_3 has two different pathways, such as reactions (4-4)–(4-6) and reaction (4-2). With increasing the CO_2 concentrations, bicarbonate formation through reaction (4-2) accounts for higher proportion. The formation of $Na_5H_3(CO_3)_4$ and $Na_2CO_3 \cdot H_2O$ favorably proceeds under low CO_2 concentrations, although their CO_2 occlusion rates are slow. Furthermore, the macropores on the surface decrease or nearly disappear within 10 min. This result leads to increasing the surface resistance to limit the transformation of Na_2CO_3 reacting with CO_2 and H_2O at the initial stage for higher CO_2 concentrations.

4.3.3 CO_2 capture of Na_2CO_3 under various H_2O concentrations

As mentioned in the section 4.3.2, the bicarbonate formation of Na_2CO_3 proceeds via two pathways under various CO_2 concentrations. The proportion of two pathways influences on the overall CO_2 occlusion rate of Na_2CO_3 along with morphology variation. To understand the effect of H_2O concentration on CO_2 occlusion of Na_2CO_3 at room temperature, thus, the study on CO_2 capture of K_2CO_3 in different humidity is important. The kinetics of CO_2 occlusion and crystal structure after the CO_2 occlusion were examined.

Figure 4-13 shows the CO_2 occlusion of Na_2CO_3 under various H_2O concentrations at the CO_2 flow rate of 30 $cm^3 \cdot min^{-1}$. For the H_2O concentration of RH38%, the CO_2 sorption amount was 7.21 $mmol \cdot g^{-1}$, which is 76.5% of the theoretical value of 9.43 at 300 min while the H_2O concentration is RH74%, the amount of CO_2 occlusion increased to 7.39 $mmol \cdot g^{-1}$. Furthermore, with increasing the H_2O concentration from RH38% to RH74%, the equilibrium time shortened from 300 to 100 min. These results

indicated that CO_2 occlusion reaction is significantly accelerated with increasing the H_2O concentration, whereas the CO_2 occlusion amount barely increased.

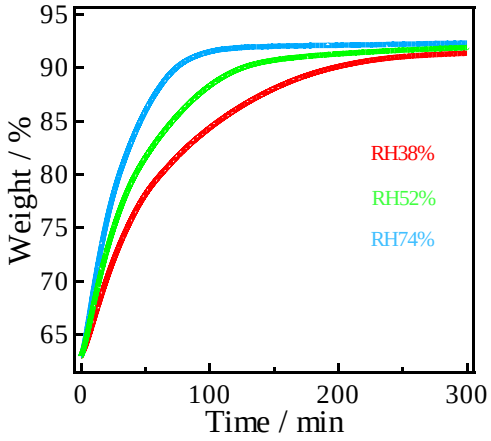

Figure 4-13: TG curves for CO_2 occlusion of Na_2CO_3 under various H_2O concentrations at 303 K.

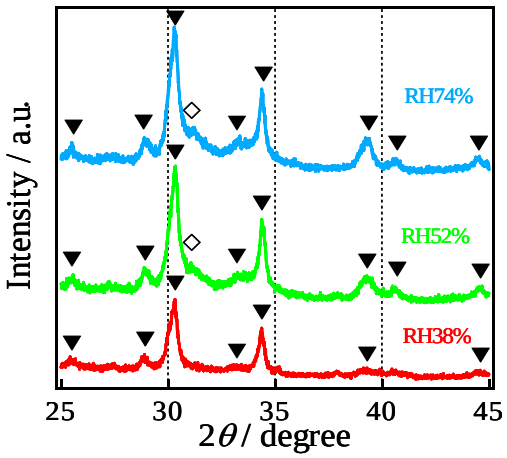

Figure 4-14: XRD patterns after CO_2 occlusion for various H_2O concentrations. ▼: $NaHCO_3$, ◇: $Na_5H_3(CO_3)_4$.

Figure 4-14 shows XRD patterns after CO_2 occlusion of Na_2CO_3 under the H_2O concentrations between RH38% and RH74%. The XRD patterns showed that major $NaHCO_3$ phase was present for above RH38% H_2O concentration. With increasing the H_2O concentration, the peak intensity of $Na_5H_3(CO_3)_4$ increased in the XRD patterns.

This result demonstrate that higher H_2O concentrations is favorable for the formation of $Na_5H_3(CO_3)_4$ transformed from $Na_2CO_3 \cdot H_2O$ through reactions (4-4) and (4-5).

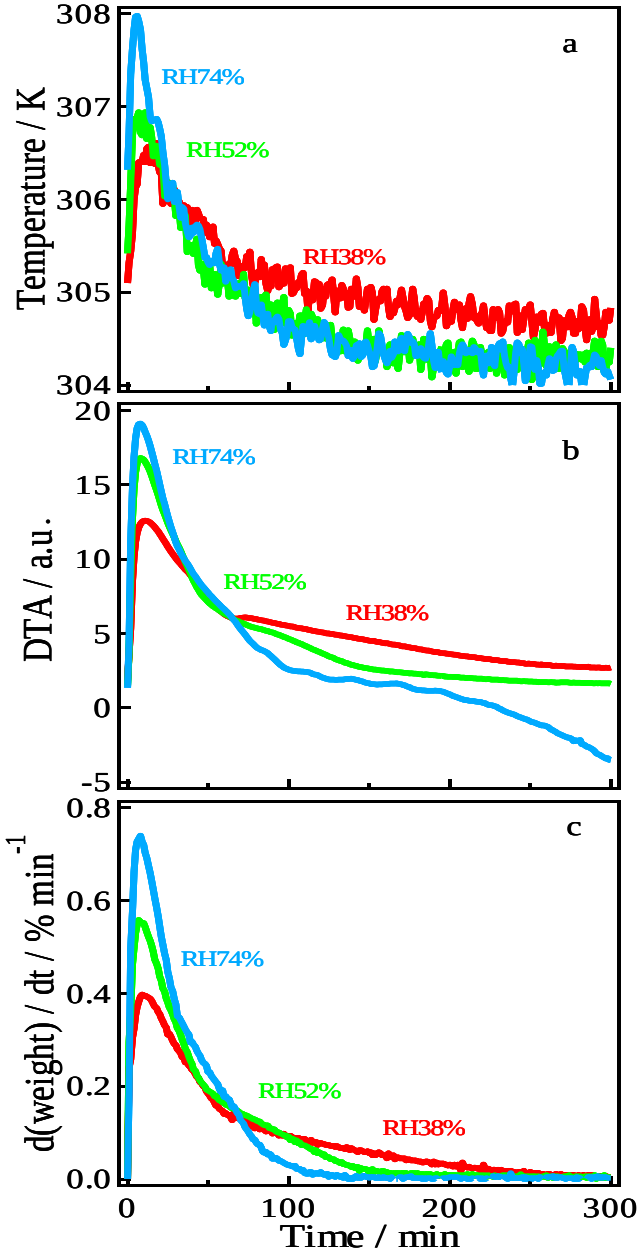

Figure 4-15: Temperature changes (a), DTA (b) and DTG (c) curves for various H_2O concentrations at a CO_2 flow rate of 30 $cm^3 \cdot min^{-1}$.

The CO_2 sorptivity of Na_2CO_3 can be tracked by monitoring the temperature under various with the bicarbonate formation of Na_2CO_3 leading to a temperature change of the exothermic reactions. Figure 4-15 showed that both DTG and DTA curves exhibited

obviously a series of peaks indicating exothermic reactions of CO_2 occlusion of Na_2CO_3. In particular, DTG curves showed that the CO_2 occlusion rate had a sharper rise at the initial stage (within 50 min) for higher H_2O concentrations. It implied that the higher H_2O concentration accelerated the CO_2 occlusion process at the initial stage. Furthermore, DTA curves associated the DTG curves displayed that the exothermic signals increased strongly with increasing the H_2O concentration at the initial stage. Consequently, it was observed that there was a significant increase in temperature at the initial stage of the reaction with increasing the H_2O concentration between RH38% and RH74%. After the initial temperature increase, the temperature decreased in all curves. These results demonstrated that the heat was obtained from the exothermic reactions at the initial stage. Moreover, these results indicated that the overall reaction rate depended upon the CO_2 occlusion rate at the initial stage. Above these observed peaks in the DTG and DTA curves for various H_2O concentrations can be understood together with analyses of the reactions at the initial stage on the basis of the crystalline structural change, which were discussed below.

Figure 4-16 shows the crystal structure changes with different time when the exothermic reaction proceeds within 40 min under various H_2O concentrations at a CO_2 flow rate of 30 $cm^3 \cdot min^{-1}$. As the reaction occurred beyond 10 min, as shown in Figure 4-16a, the XRD patterns showed that all peaks were assigned to the Na_2CO_3 phase for the H_2O concentration of RH52%, whereas the peaks for RH74% consisted of three phases such as Na_2CO_3, $Na_2CO_3 \cdot H_2O$, and $NaHCO_3$ phases. It was confirmed that higher H_2O concentration was favorable to the occurrence of the exothermic reactions (4-4) and (4-5).

With the formation of $Na_2CO_3 \cdot H_2O$ and $NaHCO_3$, it was observed that the peak intensity in the DTG and DTA curves at the initial stage increased with increasing the H_2O concentration (Figure 4-15).

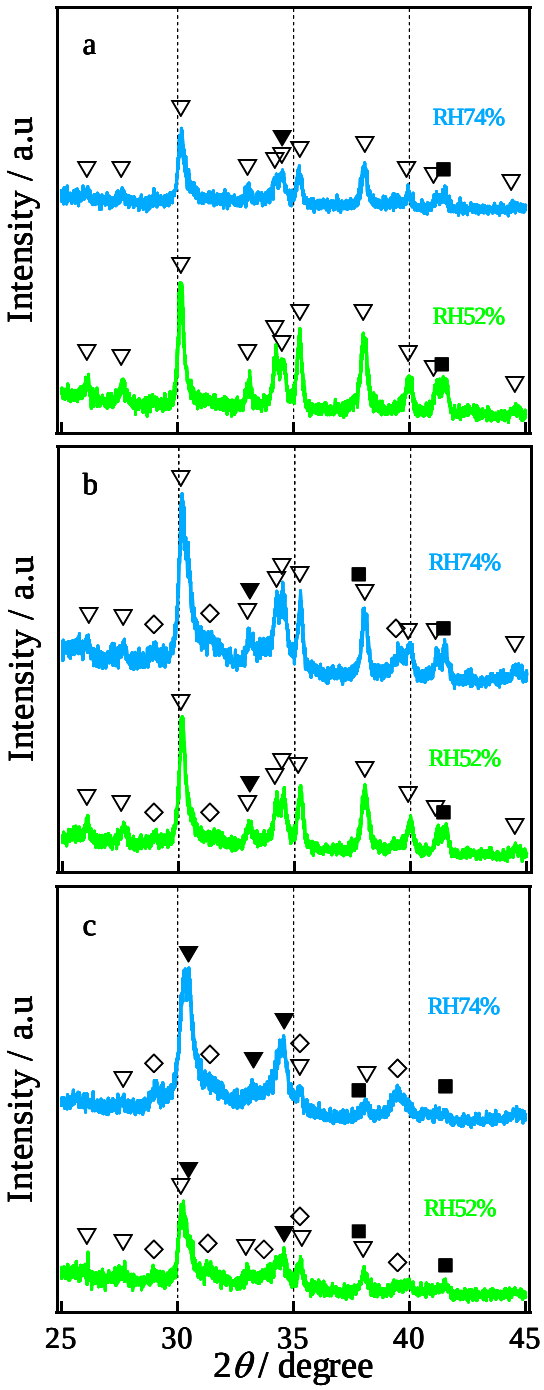

Figure 4-16: XRD patterns after CO_2 occlusion of Na_2CO_3 for various H_2O concentrations with reaction times: (a) 10 min, (b) 20 min, and (c) 40 min. ▼: $NaHCO_3$, ◇: $Na_5H_3(CO_3)_4$, ■ : $Na_2CO_3 \cdot H_2O$, ▽: Na_2CO_3.

When the reaction proceeded to 20 min, the XRD patterns showed that the peaks of $Na_2CO_3 \cdot H_2O$, $Na_5H_3(CO_3)_4$, and $NaHCO_3$ phases were present for the H_2O concentrations of RH52% and RH74%, although the dominant Na_2CO_3 phase still remained after 20 min. With the reaction time increasing to 40 min, for the H_2O concentration of RH74%, the peak intensity of $NaHCO_3$ increased significantly while the Na_2CO_3 phase significantly decreased. Moreover, the $Na_2CO_3 \cdot H_2O$ and $Na_5H_3(CO_3)_4$ phases nearly increased or decreased. This result confirms that Na_2CO_3 is converted mostly to $NaHCO_3$ through reaction (4-2). For low H_2O concentration (RH52%), the peak intensity of $Na_5H_3(CO_3)_4$ phase increased along with the formation of $Na_2CO_3 \cdot H_2O$. Conversely, with the formation of $Na_5H_3(CO_3)_4$ and $NaHCO_3$ phases between 20 and 40 min, the temperature, it was observed that there was an obvious decline in the DTG and DTA curves in Figure 4-15.

To make them understood clearly, the morphological variation of Na_2CO_3 after the CO_2 occlusion for different reaction times was examined with SEM. The SEM images for the H_2O concentrations of RH52% and RH74% are shown in Figure 4-17 and 4-11, respectively.

As shown in Figure 4-17a, for the H_2O concentration of RH52%, the diameter of macropores on the surface slightly decreased after the initial 10 min, when the macropores significantly diminished for RH74% (Figure 4-11a). After 20 min, much macropores remained on the surface, corresponding to the formation of few $Na_2CO_3 \cdot H_2O$ and $Na_5H_3(CO_3)_4$. The macroporous surface nearly disappeared at 40 min along with the formation of dominant $NaHCO_3$. The winkled surface was formed at 300 min, when the product was totally $NaHCO_3$ phase observed in the XRD patterns (Figure 4-16). In comparison to the morphological variation between 40 and 300 min for RH74%, it was found that granules on the surface did not developed obviously for RH52%. These results indicate that a higher H_2O concentration is favorable to the formation of granules on the surface of Na_2CO_3 particles.

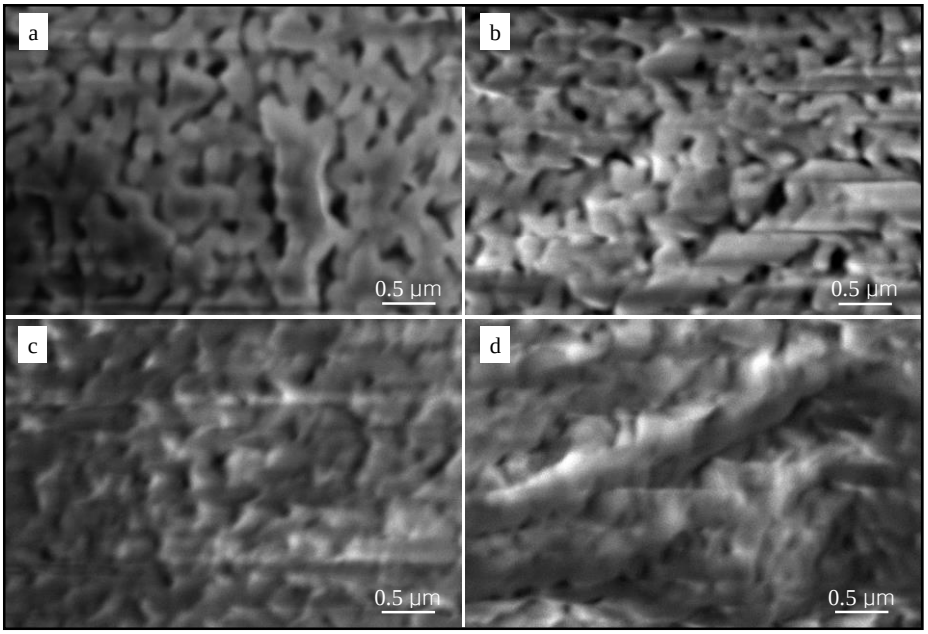

Figure 4-17: SEM images after CO_2 occlusion for the H_2O concentration of RH52% at a CO_2 flow rate of 30 $cm^3 \cdot min^{-1}$ at 303 K (a–d) (a: 10 min, b: 20 min, c: 40 min, d: 300 min).

Regarding the analyses of XRD and morphological variations with the reaction times under various H_2O concentrations, we find that the crystal structure transformation from Na_2CO_3 proceeding slowly limited the overall CO_2 occlusion rate. In particular, the transformation of Na_2CO_3 at the initial stage occurs slowly because of the weak hydration of Na_2CO_3. During this transformation process, the morphological variations do not play a crucial role in the CO_2 occlusion rate.

4.4 Conclusion

The analyses of TG and XRD show the dependence of CO_2 sorptivity of Na_2CO_3 on the temperature, CO_2 concentration, and H_2O concentration. A low temperature favors to the formation of $NaHCO_3$ with highly exothermic, whereas the formation of $Na_5H_3(CO_3)_4$ proceeds readily at higher temperatures. On the basis of the discussed the structure changes and morphological variation with reaction times under various CO_2

and H_2O concentrations, it is found that the bicarbonate formation of Na_2CO_3 has two different pathways, such as reactions (4-4)–(4-6) and reaction (4-2). For higher CO_2 and H_2O concentrations, bicarbonate formation through reaction (4-2) accounts for higher proportion. The formation of $Na_5H_3(CO_3)_4$ and $Na_2CO_3{\cdot}H_2O$ favorably occurs under low CO_2 and high H_2O concentrations, although bicarbonate formation proceeds slowly through reactions (4-5) and (4-6). Furthermore, the macropores on the surface nearly disappearing within 10 min depend mainly upon higher CO_2 and H_2O concentrations favorable for the bicarbonate formation of Na_2CO_3. This result leads to increasing the surface resistance to limit the transformation of Na_2CO_3 reacting with CO_2 and H_2O at the initial stage for higher CO_2 and H_2O concentrations, although the morphology do not a crucial role in the transformation of Na_2CO_3. In addition, Na_2CO_3 is an abundant and cheap sorbent and its CO_2 occlusion amount is 5.75 $mmol{\cdot}g^{-1}$ within 50 min for 30 $cm^3{\cdot}min^{-1}$, which is 85.6% of theoretical CO_2 capture capacity, thus, Na_2CO_3 as the CO_2 capture sorbent has some application value for CO_2 capture.

References

[1] H. Chioyama, H. Luo, T.Ohba, H. Kanoh. *Adsorption Sci. and Technol.*, **2015**, 33 (3), 243−250.

[2] C. Zhao, X. Chen, C. Zhao, Y. Liu. *Energy Fuels*, **2009**, 23, 1766−1769.

[3] J. Hoffman, H. Pennline. J. *Energy Environ. Res.*, **2001**, 1, 90−100.

[4] C. Zhao, X. Chen, C. Zhao. *J. Combust. Sci. Technol.*, **2009**, 15, 135−140.

[5] Y. Liang, D. P. Harrison, R. P. Gupta, D. A. Green, W. J. McMichael. *Energy Fuels*, **2004**, 18, 569−575.

[6] S. C. Lee, B. Y. Choi, S. J. Lee, S. Y. Jung, C. K. Ryu, J. C. Kim. *Stud. Surf. Sci. Catal.*, **2004**, 153, 527−530.

[7] J. B. Lee, C. K. Ryu, J. Baek, J. H. Lee, T. H. Eom, S. H. Kim. *Ind. Eng. Chem. Res.*, **2008**, 47, 4465−4472.

[8] Y. Seo, S. Jo, C. K. Ryu, C. Yi. *Chemosphere*, **2007**, 69, 712−718.

[9] H. Knuutila, E. T. Hessen, I. Kim, T. Haug-Warberg, H. F. Svendsen. *Chemical Engineering Science*, **2010**, 65, 2218−2226.

[10] R. R. Kondakindi, G. McCumber, S. Aleksic, W. Whittenberger, M. A. Abraham. *International Journal of Greenhouse Gas Control*, **2013**, 15, 65−69.

[11] Y. Liang. Carbon dioxide capture from flue gas using regenerable sodium-based sorbents. M.S. Dissertation, Louisiana State University (LSU), Baton Rouge, LA, **2003**.

[12] D. A. Green, B. S. Turk, R. P. Gupta, A. Lopez-Ortiz, D. P. Harrison, Y. Liang. Carbon dioxide capture from flue gas using dry regenerable sorbents. Quarterly Technical Progress Report, Research Triangle Institute: Research Triangle Park, NC, May **2001**.

[13] D. A. Green, B. S. Turk, R. P. Gupta, A. Lopez-Ortiz, D. P. Harrison, Y. Liang. Carbon dioxide capture from flue gas using dry regenerable sorbents. Quarterly Technical Progress Report, Research Triangle Institute: Research Triangle Park, NC, July **2001**.

[14] D. A. Green, B. S. Turk, R. P. Gupta, D. P. Harrison, Y. Liang. Carbon dioxide capture from flue gas using dry regenerable sorbents. Quarterly Technical Progress Report, Research Triangle Institute: Research Triangle Park, NC, Oct **2001**.

[15] D. A. Green, B. S. Turk, R. P. Gupta, W. J. McMichael, D. P. Harrison, Y. Liang. Carbon dioxide capture from flue gas using dry regenerable sorbents. Quarterly Technical Progress Report, Research Triangle Institute: Research Triangle Park, NC, Jan **2002**.

[16] D. A. Green, B. S. Turk, R. P. Gupta, W. J. McMichael, D. P. Harrison, Y. Liang. Carbon dioxide capture from flue gas using dry regenerable sorbents. Quarterly Technical Progress Report, Research Triangle Institute: Research Triangle Park, NC, April **2002**.

[17] D. A. Green, B. S. Turk, J. W. Portzer, R. P. Gupta, W. J. McMichael, Y. Liang, D. P. Harrison. Carbon dioxide capture from flue gas using dry regenerable sorbents. Quarterly Technical Progress Report, Research Triangle Institute: Research Triangle Park, NC, July **2002**.

[18] D. A. Green, B. S. Turk, J. W. Portzer, R. P. Gupta, W. J. McMichael, Y. Liang, D. P. Harrison. Carbon dioxide capture from flue gas using dry regenerable sorbents. Quarterly Technical Progress Report, Research Triangle Institute: Research Triangle Park, NC, Oct **2002**.

[19] D. A. Green, B. S. Turk, J. W. Portzer, R. P. Gupta, W. J. McMichael, Y. Liang, T. Moore, D. P. Harrison. Carbon dioxide capture from flue gas using dry regenerable sorbents. Quarterly Technical Progress Report, Research Triangle Institute: Research Triangle Park, NC, Aug **2003**.

[20] D. A. Green, B. S. Turk, J. W. Portzer, R. P. Gupta, W. J. McMichael, Y. Liang, T. Moore, M. Williams, D. P. Harrison. Carbon dioxide capture from flue gas using dry regenerable sorbents. Quarterly Technical Progress Report, Research Triangle Institute: Research Triangle Park, NC, Oct **2003**.

[21] D. A. Green, B. S. Turk, J. W. Portzer, R. P. Gupta, W. J. McMichael, T. Nelson.

Carbon dioxide capture from flue gas using dry regenerable sorbents. Quarterly Technical Progress Report, Research Triangle Institute: Research Triangle Park, NC, April **2004**.

[22] D. A. Green, B. S. Turk, J. W. Portzer, R. P. Gupta, W. J. McMichael, T. Nelson. Carbon dioxide capture from flue gas using dry regenerable sorbents. Quarterly Technical Progress Report, Research Triangle Institute: Research Triangle Park, NC, July **2004**.

[23] W. Dong, X. Chen, Y. Wu, C. Zhao, C. Liang, D. Liu. *Energy Fuels*, **2012**, 26, 6040−6046.

[24] W. Dong, X. Chen, F. Yu, Y. Wu. *Energy Fuels*, **2015**, 29, 968−973.

Chapter 5: General conclusion

Fundamentals in CO_2 sorptivity of K_2CO_3 and Na_2CO_3 are important for widespread applications for CO_2 capture. We had paid more attention to determine the effect of temperature, CO_2 concentration and humidity on CO_2 sorptivity of K_2CO_3 and Na_2CO_3 at low temperature. We also focused that the pathways of crystalline structure change and morphology variation of K_2CO_3 and Na_2CO_3 particles with reaction time depend upon various CO_2 concentrations and humidity, respectively.

In chapter 3, the studies about kinetics, structural changes and morphological variation in CO_2 sorptivity of K_2CO_3 under different temperature, CO_2 and H_2O concentrations were performed. TG-DTA and XRD analyses showed the dependence of CO_2 sorptivity of K_2CO_3 on the temperature, CO_2 concentration, and H_2O concentration. A low temperature is favorable to the bicarbonate formation. The analysis of changes in XRD patterns over reaction time of the bicarbonate formation process of K_2CO_3 under different CO_2 and H_2O concentrations, illustrates that the reaction of K_2CO_3 with CO_2 and H_2O proceeds via three reactions. Also the results of changes in exothermic properties, temperature, and CO_2 occlusion rate show that the CO_2 occlusion process of K_2CO_3 goes through three stages. The formation of $K_2CO_3{\cdot}1.5H_2O$ from K_2CO_3 provides the most heat. $K_2CO_3{\cdot}1.5H_2O$ as the first product can be converted into $K_4H_2(CO_3)_3{\cdot}1.5H_2O$ in the initial stage of CO_2 occlusion. The formation of $KHCO_3$ from $K_4H_2(CO_3)_3{\cdot}1.5H_2O$ is considered as the rate-controlling step, which slowly proceeds at the final stage, although there is a second rise in CO_2 occlusion rate and temperature under higher CO_2 flow rates (20–100 $cm^3{\cdot}min^{-1}$). The analysis of morphology variation over reaction time shows that the CO_2 occlusion of K_2CO_3 is inhibited at a higher CO_2 or lower H_2O concentration, and the formation of $KHCO_3$ from $K_4H_2(CO_3)_3{\cdot}1.5H_2O$ proceeds slowly, although increasing the CO_2 or H_2O

concentration is favorable to obtaining higher CO_2 occlusion amount. Particle morphology is found to play a crucial role in kinetic behavior of CO_2 sorptivity of K_2CO_3 and $K_4H_2(CO_3)_3 \cdot 1.5H_2O$. Ultimately, K_2CO_3 can be used for CO_2 capture under low temperature, and 5–10% CO_2 concentration in the presence of saturated water vapor.

In chapter 4, the analyses of TG and XRD show the dependence of CO_2 sorptivity of Na_2CO_3 on the temperature, CO_2 concentration, and H_2O concentration. A low temperature favors to the formation of $NaHCO_3$ with highly exothermic, whereas the formation of $Na_5H_3(CO_3)_4$ proceeds readily at higher temperatures. On the basis of the discussed the structure changes and morphological variations with reaction times under various CO_2 and H_2O concentrations, it is found that the bicarbonate formation of Na_2CO_3 has two different pathways, such as reactions (4-4)–(4-6) and reaction (4-2). For higher CO_2 and H_2O concentrations, bicarbonate formation through reaction (4-2) accounts for higher proportion. The formation of $Na_5H_3(CO_3)_4$ and $Na_2CO_3 \cdot H_2O$ favorably occurs under low CO_2 and high H_2O concentrations, although bicarbonate formation proceeds slowly through reactions (4-5) and (4-6). Furthermore, the macropores on the surface nearly disappearing within 10 min depend mainly upon higher CO_2 and H_2O concentrations favorable for the bicarbonate formation of Na_2CO_3. This result leads to increasing the surface resistance to limit the transformation of Na_2CO_3 reacting with CO_2 and H_2O at the initial stage for higher CO_2 and H_2O concentrations, although the morphology does not play a crucial role in the transformation of Na_2CO_3. In addition, Na_2CO_3 is an abundant and cheap sorbent and its CO_2 occlusion amount is 5.75 $mmol \cdot g^{-1}$ within 50 min for 30 $cm^3 \cdot min^{-1}$, which is 85.6% of theoretical CO_2 capture capacity, thus, Na_2CO_3 as the CO_2 capture sorbent has some application value for CO_2 capture.

On the basis of the discussions of CO_2 occlusion of K_2CO_3 and Na_2CO_3, K_2CO_3 and Na_2CO_3 can be applied for CO_2 capture but the former has better application prospect. The basic reason for this case is the different crystal structures of K_2CO_3 (hexagonal)

and Na_2CO_3 (monoclinic) decomposed from the bicarbonate. Consequently, the hydration reaction of K_2CO_3 can transform more easily whereas that of Na_2CO_3 proceeds more slowly.

Acknowledgments

First and foremost I would like to express my deep gratitude to my supervisor, Professor Hirofumi Kanoh, for all his contributions of time, funding, and guidance to make my doctoral program. I appreciate what he has taught me during past three years.

I would like to express my thanks to Associate professor Tomonori Ohba and Assistant professor Stephan Thürmer for their precious comments and invaluable discussion. I would like to thank my tutors, Mr. Yoshikazu Kobayashi and Mr. Hideyuki Chioyama, for their advice and helps.

I want to thank Dr. Itoh of Center for analytical instrumentation for his help for SEM measurement. I also thank my colleagues from Molecular Chemistry and Molecular Nanochemistry Groups, in particular, Mr. Benny Permana and Ms. GuangYang for their encouragement, Mr. Yuki Ohyama and Mr. Manabu Sasaki for the maintenance of XRD, and Mr. Atsushi Takase, Mr. Shotaro Yamamoto, Mr. Kazuki Ohazama, and Mr. Takahisa Okuno for their helps and discussion.

The members of Molecular Chemistry and Molecular Nanochemistry Groups have a friendly relation as well as good communication to make me appear to be warm at home. I am grateful for the memorable activities, such as the barbecue and trips that spent two days and one night together, to enrich my life at Chiba.

Finally, I would like to thank my family for the support for my pursuits and all their love.

July, 2015

Hongchao Luo

Accomplishments

Conference

1) Hongchao Luo, Hideyuki Chioyama, Tomonori Ohba, Hirofumi Kanoh. Kinetics and Structural Changes in CO_2 Sorption of K_2CO_3 and Na_2CO_3 under Moisture, Gordon research Seminars (GRS), 26-27th July, 2014, HongKong, China.[Poster]
2) Hongchao Luo, Hideyuki Chioyama, Tomonori Ohba, Hirofumi Kanoh. Kinetics and Structural Changes in CO_2 Sorption of K_2CO_3 and Na_2CO_3 under a Moist Condition, 10th International Conference on Separation Science and Technology (ICSST), October 30–November 1, 2014, Nara Prefectural New Public Hall, Nara, Japan.[Poster]

Publication

1) H. Chioyama, H. Luo, T. Ohba, and H. Kanoh

   Temperature-dependent Double-step CO_2 Occlusion of K_2CO_3 under Moist Conditions

   Ads. Sci. Technol., **2015**, 33, 243-250.

   DOI: http://dx.doi.org/10.1260/0263-6174.33.3.243

2) H. Luo, H. Chioyama, S. Thürmer, T. Ohba, and H. Kanoh

   Kinetics and Structural Changes in CO_2 Capture of K_2CO_3 under a Moist Condition

   Energ. Fuel, **2015**, 29, 4472–4478.

   DOI: 10.1021/acs.energyfuels.5b00578